(NASA-TM-87448) ON THE SOLUTION OF THE THREE-DIMENSIONAL FLOWFIELD ABOUT A FLOW-THROUGH NACELLE Ph.D. Thesis (George Washington Univ.) 159 p HC A08/MF A01 CSCL 01A 33/02

N85-22371

Unclas 20275

ON THE SOLUTION OF THE THREE-DIMENSIONAL FLOWFIELD ABOUT A FLOW-THROUGH NACELLE

By

William Bernard Compton III

B.S. June 1961, The University of Alabama

M.S. January 1973, The George Washington University

A Dissertation submitted to

The Faculty of

The School of Engineering and Applied Science

of The George Washington University in partial satisfaction

of the requirements for the degree of Doctor of Science

May 5, 1985

Dissertation directed by

John Lindsey Whitesides

Professor of Engineering and Applied Science

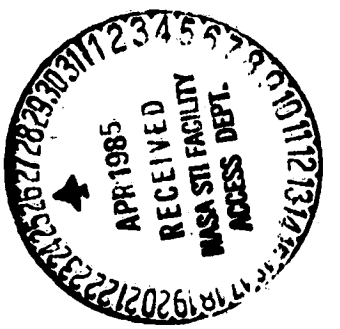

ABSTRACT

A study has been made of the solution of the three-dimensional flow field for a flow-through nacelle. Both inviscid and viscous-inviscid interacting solutions were examined. Inviscid solutions were obtained with two different computational procedures for solving the three-dimensional Euler equations. The first procedure employs an alternating-direction-implicit numerical algorithm, and required the development of a complete computational model for the nacelle problem. The second computational technique employs a fourth-order Runge-Kutta numerical algorithm which was modified to fit the nacelle problem. Viscous effects on the flow field were evaluated with a viscous-inviscid interacting computational model. This model was constructed by coupling the explicit Euler solution procedure with a "lag-entrainment" boundary layer solution procedure in a global iteration scheme. The computational techniques have been used to compute the flow field for a long-duct turbofan engine nacelle at free-stream Mach numbers of 0.80 and 0.94 and angles-of-attack of 0^{o} and 4^{o}.

The numerical experiments show that for predicting the flow inside the nacelle's duct, the viscous effects are extremely important and both the external and internal boundary layers and wakes must be simulated. The internal boundary layer creates a pressure gradient in the nacelle's duct. The external boundary layer and its associated wake displace the streamlines away from the external surface. The displacement of the

streamlines effectively decambers the nacelle's airfoil and weakens the compression at the trailing edge. This gives a less positive exit pressure and hence a less positive overall internal pressure level which agrees better with experiment than the inviscid computations. Therefore, if simulating the correct mass flow through a flow-through nacelle's duct is important, then viscous effects must be included in the computational model.

In contrast to the internal surface, viscous effects were relatively unimportant for predicting the flow on the external surface of the nacelle. Good agreement is shown between the computational results of both Euler numerical procedures and wind-tunnel data on the external surface of the nacelle. The solutions exhibit the proper three-dimensional behavior at both angles of attack and correctly reflect the qualitative and quantitative results at both Mach numbers.

The solutions of both Euler computational techniques exhibited a total pressure loss on the internal surface of the nacelle. An investigation of the loss proved that it was the result of the flow stagnating on the external surface and expanding around the sharp discontinuity in the surface of the nacelle at its leading edge. The studies indicate that the use of C-type grids could probably eliminate the loss. However, for sharp leading edges or where an H-type grid is desirable, it appears that some (problem-dependent) total pressure loss is inherent in numerical Euler-equation solutions.

Even though reasonably accurate engineering solutions were obtained with the implicit computational procedure, a weak instability was discovered in it when applied to the three-dimensional nacelle problem. This instability prevented the implicit solutions from actually converging

although the long wavelength nature of the instability requires a large number of integration steps before it becomes evident. The explicit computational technique is stable.

TABLE OF CONTENTS

LIST OF FIGURES

LIST OF SYMBOLS

A,B,C	Jacobian matrices of the transformed Euler flux vectors $\hat{F},\hat{G},\hat{H}$
$\bar{A},\bar{a}$	scalar multipliers for convergence acceleration in the explicit numerical procedure
a_1,a_2,a_3	coefficients in the Runge-Kutta numerical algorithm
a,b,c,d	terms in the surface boundary equation, equation (37)
C_p	pressure coefficient, $(p - p_\infty)/q_\infty$
C_f	skin-friction coefficient, $\tau_w/(0.5\rho_e U_e^2)$, Chapter VI
C_{f_0}	skin-friction coefficient in equilibrium flow in zero pressure gradient, Chapter VI
C_τ	shear-stress coefficient, $\tau/(\rho U_e^2)$, Chapter VI
C_e	entrainment coefficient, Chapter VI
c_v	specific heat at constant volume
D	numerical dissipation terms, equation (50)
d	numerical dissipation terms, equation (51)
E	total energy, $c_v T + 0.5\,(u^2 + v^2 + w^2)$
$\underline{F},\underline{G}$	flux vectors in the steady Navier-Stokes equations, Chapter VI
$\hat{F},\hat{G},\hat{H}$	flux vectors in the transformed Euler equations
$\bar{F}$	matrix of fluxes in the finite volume formulation of the Euler equations
$\underline{f},\underline{g},\underline{h}$	flux vectors in the Euler equations
$\underline{\bar{f}},\underline{\bar{g}}$	flux vectors in the boundary layer equations, Chapter VI
h	height of the boundary layer, Chapter VI

g^{mn}	metric tensor
H	total enthalpy
$H, \bar{H}, H_1$	boundary layer shape parameters, Chapter VI
I	identity matrix
J	Jacobian of the transformation from the physical coordinate system to the computational coordinate system
M	Mach number
$\underline{n}$	unit normal vector
P	residual, equation (55)
p	pressure
q	dynamic pressure, defines C_p in symbol list
$\underline{q}$	vector of dependent variables, equation (2)
Δq	incremental vector of dependent variables
R	gas constant
R	body radius, equation (69)
R	Riemann invariant, Chapter IV
r	radial cylindrical coordinate
S	surface area
T	static temperature
t	time
Δt	incremental time
U	velocity at the boundary, equations (61-63)
$\underline{U}, \underline{V}, \underline{W}$	contravariant velocities in the ζ, ξ, η directions
U_e	boundary layer edge velocity, Chapter VI
$\underline{u}, \underline{v}, \underline{w}$	velocities in the x,y,z directions

$\underline{V}$	surface velocity, equations (11 and 65)
V	Volume of the computational domain, equation (39)
$\underline{V}$	axisymmetric transpiration velocity normal to the wall, Chapter VI
$\underline{v}$	two-dimensional transpiration velocity normal to the wall, Chapter VI
v	differential volume, equation (39)
$\underline{v}_w, \underline{w}_w$	y and z components of the transpiration velocity normal to the wall, Chapter VI
x,y,z	Cartesian coordinates

Greek and Mathematical Symbols

α	angle-of-attack
β	scalar multiplier, equation (56)
γ	ratio of specific heats
δ	boundary layer thickness, Chapter VI
δ^*	boundary layer displacement thickness, Chapter VI
$\bar{\varepsilon}$	smoothing coefficient, equation (55)
$\delta_\zeta, \delta_\xi, \delta_\eta$	differencing operators in the ζ,ξ, and η directions
ζ,ξ,η	spacial coordinates in the transformed computational space
Θ	boundary layer momentum thickness, Chapter VI
Θ	circumferential coordinate
λ	boundary layer scaling parameter on dissipation length, Chapter VI
ρ	density
Σ	denotes summation
τ	transformed time, equations (28-31)

ϕ	potential function in the telegraph equation, equation (59)
ϕ	circumferential angular location
ψ	source terms on the right hand side of the characteristic compatability relations
ω,ν,ε	numerical dissipation coefficients
∇	partial derivative operator

Superscripts and Subscripts

b	boundary
e	explicit
$\hat{}$	denotes transformed quantity
I	denotes the face of a computational cell
i	implicit
i,j,k	indices corresponding to the ζ,ξ,η directions
int	internal
ℓ	summation index
n	denotes current time step
t	stagnation conditions
w	wall values
∞	free stream conditions
$(\underline{\ })$	denotes vector quantity

All variables are nondimensionalized by appropriate combinations of the free stream parameters, the length of the nacelle, and the specific heat at constant volume.

ACKNOWLEDGMENTS

The author wishes to express his appreciation to the National Aeronautics and Space Administration for its continued support of his graduate studies and for supporting the research presented in this dissertation.

The author is very appreciative of the assistance and guidance given by his advisor, Dr. John L. Whitesides, during both the graduate studies and the research investigation.

The author extends special thanks to Miss Sherri L. Sanchez for typing the manuscript.

In addition, thanks are extended to the author's colleagues at Langley Research Center and elsewhere with whom many technical discussions were carried out. Special thanks are extended to Mr. Lawrence E. Putnam who suggested the general research area, and also to Dr. Richard E. Wilmoth who reviewed the manuscript and provided many helpful suggestions.

The author especially wishes to express his gratitude to his parents who continually encouraged him during his graduate studies and research, and to whom this dissertation is dedicated.

CHAPTER I

INTRODUCTION

Since fuel costs are projected to rise significantly over the next several decades, further growth of the air transportation system becomes increasingly dependent on advances in aircraft technology and design.[1] One important area of transport technology in which there is a potential for significant improvement is the integration of the propulsion system with the airframe. To tap this potential, engineers must increase their understanding of the aerodynamic interactions between the various components of the propulsion system and airframe well beyond the understanding which now exists.

Both experimental and theoretical research is required. Experimental studies of these interactions necessitate expensive, complex models to simulate adequately the inlet and exhaust flows. Consequently, experimental investigations are only practical for limited parametric studies. For analysis and design optimization, increasing attention is being given to the use of computational methods which have been validated by a few discrete experiments. For example, both the Airbus 310 and the Boeing 757 wings have been designed with the aid of numerical analysis.[2]

Because of the geometrical complexity of transport configurations and computer storage limitations, current computational design studies of this type have mainly been limited to inviscid potential-flow methods. These methods, which range from panel techniques to solutions of the full

transonic potential equation,[3-5] have proven to be useful tools in the aircraft design process. Nevertheless, they do not adequately simulate flows where rotationality is important.

To account for rotationality, even in the inviscid case, the application of the Euler equations is required. Solving the inviscid, variable entropy, compressible flow equations allows the solution to capture strong shocks and simulate the jet exhaust flow without special treatments. In addition, vortex sheets may be captured, and as recently shown by Rizzi and Erickson,[6] a Kutta condition may not need to be explicitly enforced. The Euler equations also are thought to yield unique solutions, whereas the full potential equation can yield multiple solutions as shown by Salas[7] and Steinhoff and Jameson.[8] Despite their greater potential, most solutions of the Euler equations have been either two-dimensional, or for relatively simple three-dimensional configurations, or on coarse grids.[9-13] Finally, strong interactions can occur between the viscous boundary layer and the main stream even when the boundary layer does not separate. Hence, the influence of viscosity on the flow field must also be accounted for in order to simulate the physically realistic case.

Therefore, a study of the solution of the three-dimensional flow field for a flow-through nacelle using the Euler equations and a viscous-inviscid interacting computational model was initiated. A flow-through nacelle was selected for the study since the engine nacelle is a fundamental component of a transport's propulsion system. The objective of this research was to investigate the flow field about the flow-through nacelle and the importance of simulating the viscous effects in a computational model for solving this problem. It included investigating

the suitability of the Euler equations as the basis for the computational model and the problems associated with obtaining numerical solutions for this type of configuration. In addition, it involved consideration of the advantages and disadvantages of the basic types of numerical algorithms and solution techniques suitable for flows of this complexity. In order to focus specifically on the application of computational solutions to the flow-through nacelle problem, only state-of-the-art algorithms were considered.

To conduct the study, two separate Euler computational procedures were investigated, each of which appeared to offer certain distinct advantages. The first procedure employed an alternating-direction-implicit numerical algorithm and required development of a computational model specifically geared to the nacelle problem. An interim report on this phase of the research is given in reference 14. The second procedure investigated involved modification of an existing fourth-order Runge-Kutta algorithm to fit the nacelle problem. Viscous effects on the flow field were evaluated with a viscous-inviscid interacting computational model. This model was constructed by coupling the explicit Euler solution procedure with a "lag-entrainment" boundary layer solution procedure in a global iteration scheme.

The computational techniques have been used to compute the flow field for a long-duct turbofan engine nacelle at free-stream Mach numbers of 0.80 and 0.94 and angles-of-attack of 0^{o} and 4^{o}. The results are compared with experimental data. New insight into the mechanics of the interactions between the internal and external flows, gained during these investigations, is discussed. Problem areas, both general and algorithm dependent, are identified and investigated. The numerical performance of

the two techniques is compared, and recommendations are made for further numerical studies.

CHAPTER II

MATHEMATICAL DESCRIPTION OF THE PROBLEM

Governing Flow Equations

The Euler equations mathematically describe the physical laws governing the motion of an inviscid compressible fluid with variable entropy. In the present solution procedure, the three-dimensional time-dependent Euler equations are normalized and written in strong conservation form for a Cartesian coordinate system. If body forces are neglected, these time-dependent equations for mass, linear momentum, and energy can be expressed in vector notation as

$$\frac{\partial q}{\partial t} + \frac{\partial f}{\partial x} + \frac{\partial g}{\partial y} + \frac{\partial h}{\partial z} = 0 \tag{1}$$

where

$$\underline{q} = \begin{Bmatrix} \rho \\ \rho u \\ \rho v \\ \rho w \\ \rho E \end{Bmatrix}, \qquad \underline{f} = \begin{Bmatrix} \rho u \\ \rho u^2 + p \\ \rho uv \\ \rho uw \\ u(\rho E + p) \end{Bmatrix} \tag{2}$$

$$\underline{g} = \begin{Bmatrix} \rho v \\ \rho uv \\ \rho v^2 + p \\ \rho vw \\ v(\rho E + p) \end{Bmatrix}, \qquad \underline{h} = \begin{Bmatrix} \rho w \\ \rho uw \\ \rho vw \\ \rho w^2 + p \\ w(\rho E + p) \end{Bmatrix}$$

In these equations, u, v, and w are velocities in the physical coordinate system (coordinates x,y,z), ρ is the density, and p is the pressure. The total energy, E, is given by

$$E = c_v T + \frac{1}{2}(u^2 + v^2 + w^2) \tag{3}$$

where T is the temperature, and c_v is the specific heat at constant volume. The equation of state

$$p = \rho RT \tag{4}$$

where R is the gas constant, completes the system of equations.

The major interest in using computational fluid dynamics for propulsion integration studies is in predicting the steady state flow for any given configuration. Therefore, the solutions to only steady flows are considered in this analysis. In this case, the total enthalpy, H, where

$$H = E + \frac{p}{\rho} \tag{5}$$

does not vary throughout the flowfield of the flow-through nacelle; and the energy equation, the fifth equation of the set (1), could be replaced

by the condition of constant enthalpy. However, in general for propulsive flows the enthalpy is not constant due to the jet exhaust. Therefore, to be consistent with the ultimate objective of this study, the full energy equation was solved along with the continuity and momenta equations.

Computational Domain and Grid System

A sketch of the three-dimensional computational domain illustrating the nacelle and domain boundaries in both the physical and computational spaces is presented in figure 1. Three dimensionality is produced by rotating the vertical cross-section about the axis of the nacelle, thus generating a cylindrical domain (see part (a) of the figure). To minimize computer run time and storage requirements, symmetry is assumed about the vertical plane, and only one-half of the cylindrical domain is computed. When transformed to the computational space, the coordinate system becomes a rectangular three-dimensional domain (see part (b)). The axis, which is singular, transforms into a plane forming one side of the domain, and the nacelle surfaces transform into a common internal plane as illustrated in figure 1(b).

In the computational domain, the grid system constructed for the discretised solution procedures is body fitted (grid lines coincide with the nacelle surface and other boundaries) in order to facilitate implementation of the boundary conditions. It is a sheared, H-type computational grid. Figure 2 presents a vertical cross section of the grid in the physical space, again illustrating the nacelle geometry and the various boundaries. The grid mesh in the circumferential direction is generated by rotating the vertical cross-section about the axis of the nacelle. The grid spacing in the physical space is geometrically

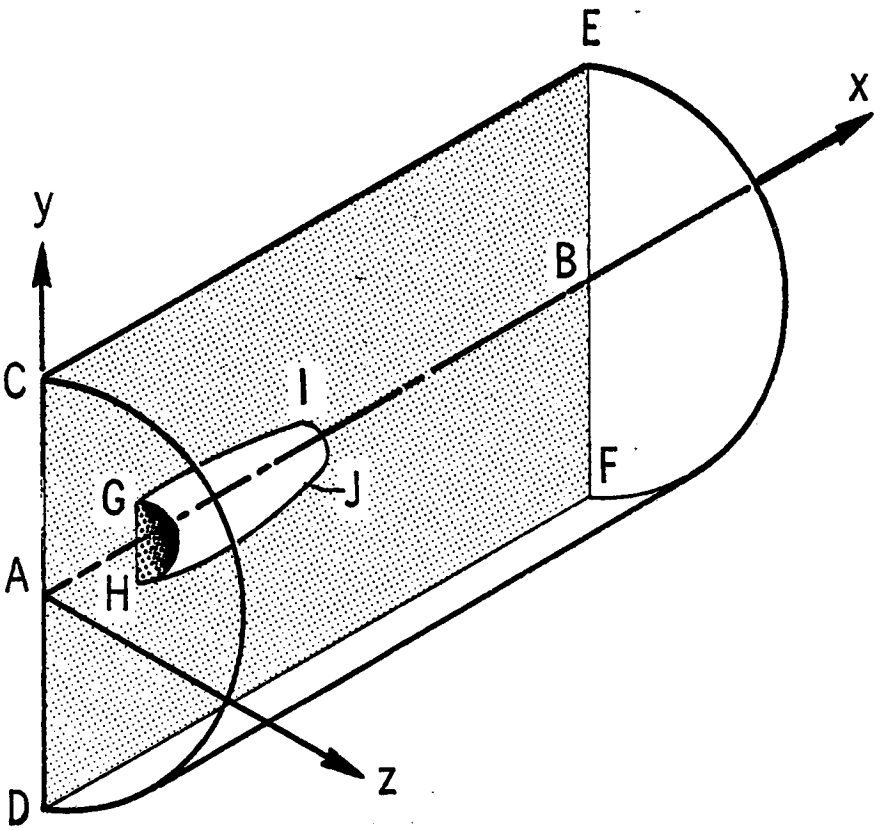

(a) Physical space

Figure 1. Sketch of the computational domain.

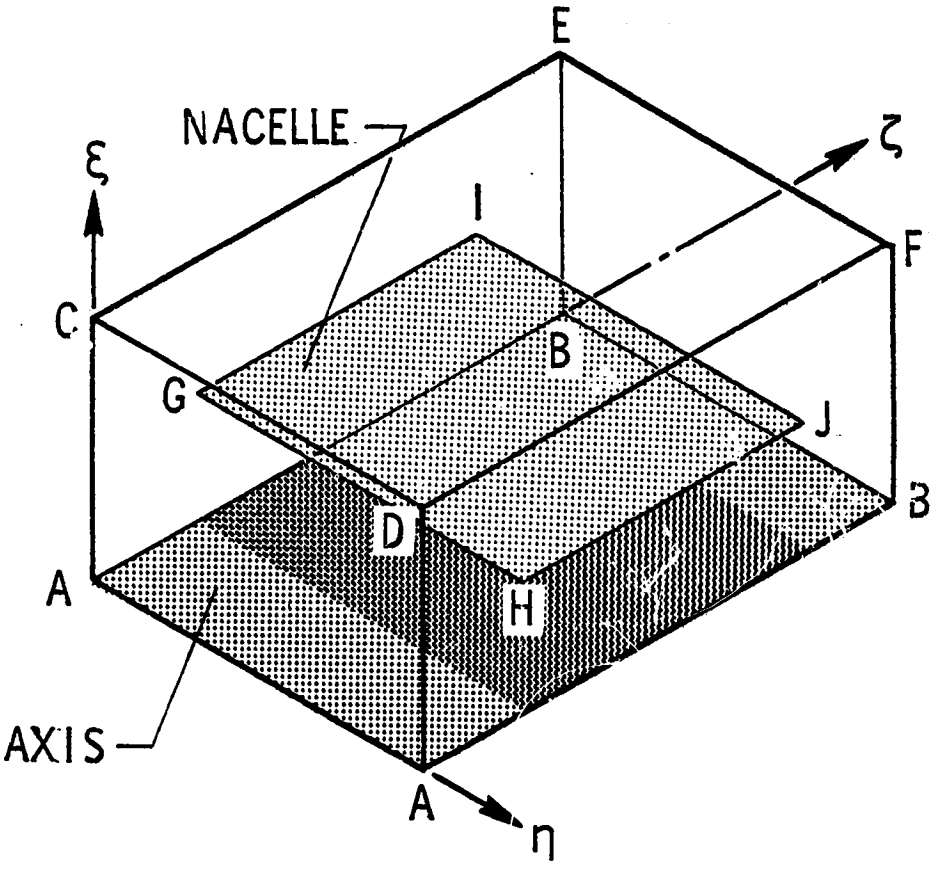

(b) Computational space

Figure 1. Concluded.

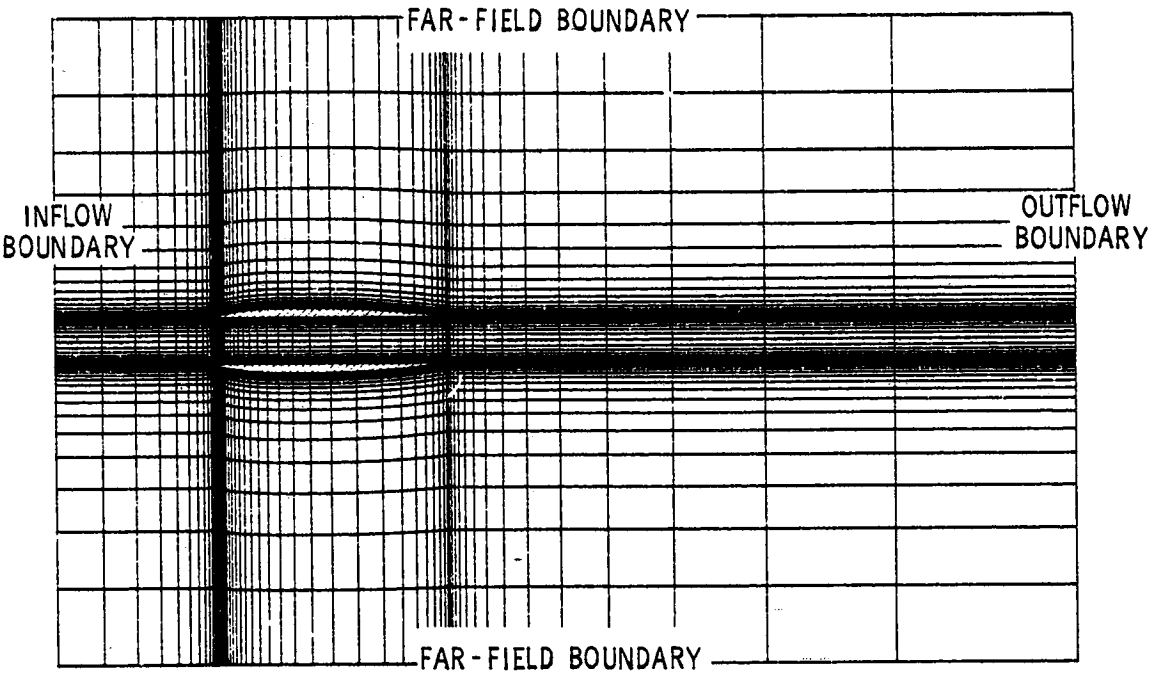

Figure 2. Cross section of a typical three-dimensional grid.

stretched away from the nacelle with grid points being clustered near the nacelle surface and near the leading and trailing edges. The basic computations were made with 58 axial grid planes (30 along the nacelle), 29 grid planes in the radial direction, and 11 in the circumferential direction. Additional calculations were made with grids refined in the axial direction: one containing 68 axial grid planes (40 along the nacelle), and another with 115 axial grid planes (59 along the nacelle).

Analytical Boundary Conditions

For the mathematical description of a physical problem to be well posed, whether the partial differential equations are to be solved in closed form or numerically, the correct boundary conditions must be included. Further, in numerically solving a set of equations in any finite computational domain, boundary conditions arise from two different sources. First, analytical boundary conditions are necessary for the problem to be well posed, and second, numerical boundary conditions arise from a need to complete the differencing equations in the numerical algorithm. The analytical boundary conditions will be discussed in this chapter, while the numerical boundary conditions will be discussed in the chapters which present the computational procedures.

The flow-through nacelle problem includes inflow, outflow, symmetry, far-field, and impermeable surface boundaries. For a well posed problem, only part of the flow variables can be specified at each boundary, with the number and combination of the variables depending on the type of boundary. Characteristic theory provides a guide to both the number and the form of the boundary conditions. Cline[15] describes the application of the theory for this purpose. The theory gives the same results for an

inviscid fluid as the energy method of Oliger and Sundstrom,[16] and was used as a guide in determining the boundary conditions for this work.

Since the mainstream is essentially perpendicular to the inflow and outflow boundaries, reference plane characteristics will be used to determine the number and form of these boundary conditions. Reference plane characteristics are an approximate form of the characteristic equations; however, they are exact if the cross derivative terms are zero. For the three-dimensional Euler equations, the constant-y-constant-z reference plane characteristics can be written

characteristic direction	compatability relation	
$\frac{dx}{dt} = u$	$\begin{cases} \rho \frac{dv}{dt} = \psi_3 \\ \rho \frac{dw}{dt} = \psi_4 \\ \frac{dp}{dt} - a^2 \frac{d\rho}{dt} = \psi_5 \end{cases}$	(6)
$\frac{dx}{dt} = u + a$	$\frac{dp}{dt} - a^2 \frac{du}{dt} = a^2\psi_1 + a\psi_2 + \psi_5$	(7)
$\frac{dx}{dt} = u - a$	$\frac{dp}{dt} - \rho a \frac{du}{dt} = a^2\psi_1 - a\psi_2 + \psi_5$	(8)

where

$$\psi_1 = - \left\{ \frac{\partial}{\partial y} (\rho v) + \frac{\partial}{\partial z} (\rho w) \right\}$$

$$\psi_2 = - \left\{ \rho v \frac{\partial u}{\partial y} + \rho w \frac{\partial u}{\partial z} \right\}$$

$$\psi_3 = - \left\{ \rho v \frac{\partial v}{\partial y} + \rho w \frac{\partial v}{\partial z} + \frac{\partial p}{\partial y} \right\} \qquad (9)$$

$$\psi_4 = - \left\{ \rho v \frac{\partial w}{\partial z} + \rho w \frac{\partial w}{\partial z} + \frac{\partial p}{\partial z} \right\}$$

$$\psi_5 = - \left\{ - a^2 \left(v \frac{\partial \rho}{\partial y} + w \frac{\partial \rho}{\partial z} \right) + v \frac{\partial p}{\partial y} + w \frac{\partial p}{\partial z} \right\}$$

and a is the local speed of sound. For a flow with the mainstream in the x-direction, the ψ terms on the right hand side of these equations are very small and are treated as constants, and the equations become exact when the ψ terms are identically zero. The characteristic directions of equations (6), (7), and (8) represent the projection of the flow pathline and Mach cones on the x-t plane. Subject to the approximate nature of the reference plane characteristics, they comprise a set of five equations in five unknowns and completely describe the flow in the computational domain.

Figure 3 presents a sketch depicting the projection of the characteristic curves on the x-t plane. For a boundary with inflow in the positive x-direction, the shaded area represents the computational domain. Since three compatibility equations are associated with the curve $dx/dt = u$, equation (6), there are four characteristics entering the computational domain and one leaving it. The four characteristics

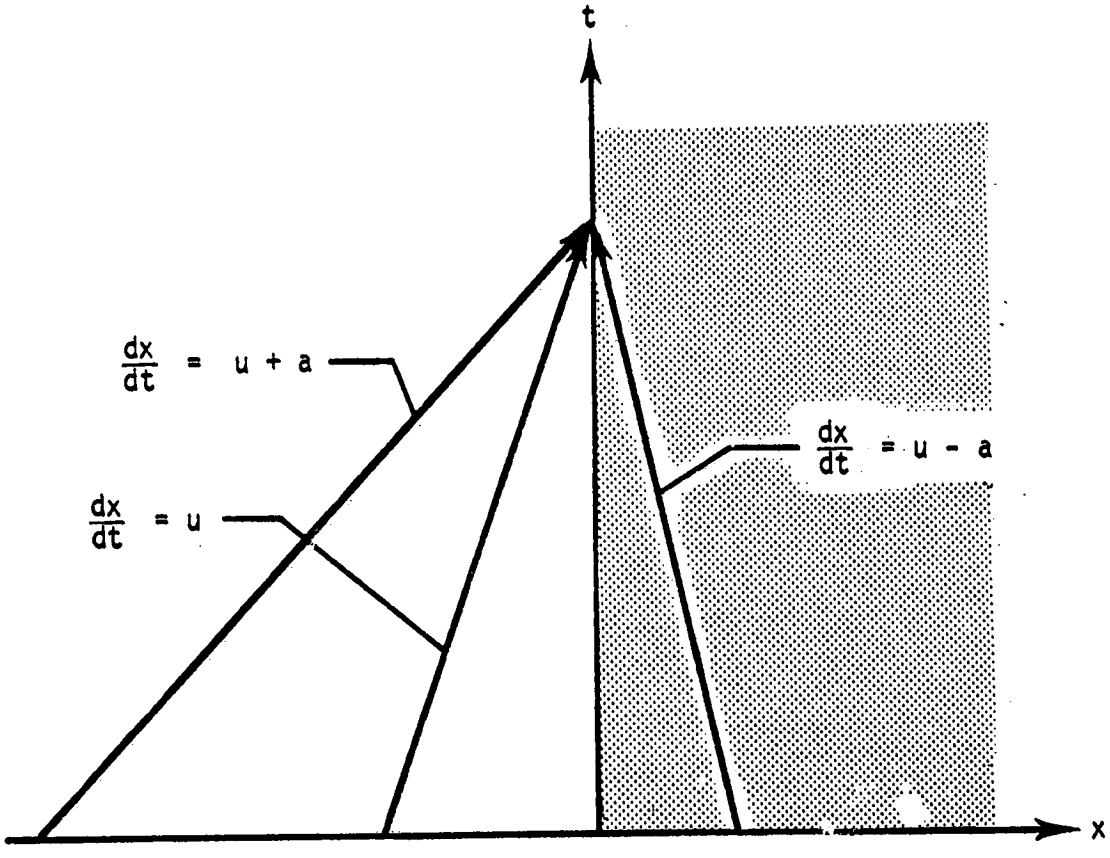

Figure 3. Sketch depicting projection of the characteristic curves on the x-t plane.

entering the domain carry no information whatsoever about the internal solution, and therefore they must be replaced by four boundary conditions. The form of the boundary conditions is obtained from the characteristic leaving the computational domain, equation (8). Since it originates from within the domain, both p and u cannot be prescribed because they must obey the compatability relation holding along the characteristic curve. Usually the total pressure, total temperature, and flow angle are supplied at an inflow boundary, or, an alternate combination consisting of a function of the total entropy, the static temperature, and velocities.

For a boundary with outflow in the positive x-direction, the unshaded area of figure 3 represents the computional domain. The figure illustrates that there is only one characteristic entering the computational domain, indicating one boundary condition must be supplied. It is usually the static pressure, since, when combined with the previous inflow boundary conditions, it completely defines the free stream.

The far field boundary can be either an inflow or an outflow boundary. Therefore the appropiate conditions described above are applied.

The expression for the boundary conditions at the symmetry plane is

$$\frac{\partial q}{\partial \underline{n}} = 0 \tag{10}$$

where $\underline{n}$ is the normal to the symmetry plane.

Finally, the surface boundary condition is that the flow is tangent to the wall, and is expressed by the equation

$$\underline{n} \cdot \underline{V} = 0 \qquad (11)$$

where $\underline{V}$ is the velocity at the surface and $\underline{n}$ represents the unit vector normal to the surface.

As mentioned above, in addition to these analytical boundary conditions, numerical boundary conditions necessary to complete the difference equations are required when actually carrying out the numerical process. They will be discussed in the next two chapters.

Nacelle configuration

A flow-through nacelle was selected for the study since the engine nacelle is a fundamental component of a transport aircraft's propulsion system. The particular flow-through nacelle chosen is depicted in figures 1 and 2. The external surface of the nacelle consisted of a NACA 1-70-100 inlet, a cylindrical section, and a circular arc afterbody. The internal duct of the nacelle was cylindrical. For the computations, the leading edge was made sharp as a simplification to the geometry. This particular configuration was chosen because it resembled long-duct turbofan engine nacelles being proposed for current jet transports, and because experimental data for the isolated nacelle were available for comparison with the computational results.

CHAPTER III

IMPLICIT COMPUTATIONAL PROCEDURE

The implicit procedure used for the flow-through nacelle problem employs the approximately-factored, alternating-direction implicit algorithm of Beam and Warming.[17] This algorithm has been applied successfully to a number of two- and three-dimensional problems.[18,19] The principal advantage offered by implicit methods is that, if properly formulated, they theoretically have no stability limitations on the size of the time step when integrating the set of flow equations. Thus, for obtaining steady-state solutions, fewer integration steps may be needed. The use of a large time step can in some cases further act to accelerate the convergence rate in a manner similar to relaxation schemes for elliptic problems. The principal disadvantage of implicit methods is the requirement for solving large sets of simultaneous algebraic equations. Thus while fewer time steps may be required than for explicit methods, more computational work per time step is usually needed. However, the previous applications of the Beam and Warming algorithm have indicated favorable improvements in overall computational efficiency. The application of this algorithm to solving the three-dimensional Euler equations for flow-through nacelles required the development of a computational model specifically geared to the problem. This chapter describes that computational model.

Transformed Euler Equations

Equation (1) presented the Euler equations written for a Cartesian coordinate system. In the present finite difference technique, the equations are transformed to the computational space before they are integrated. The transformed version of the three-dimensional Euler equations can be written

$$\frac{\partial \hat{q}}{\partial t} + \frac{\partial \hat{F}}{\partial \zeta} + \frac{\partial \hat{G}}{\partial \xi} + \frac{\partial \hat{H}}{\partial \eta} = 0 \tag{12}$$

where t is the normalized time, ζ, ξ, and η are the spatial coordinates in the transformed plane, and

$$\begin{aligned} \hat{q} &= J\underline{q} \\ \hat{F} &= J(\zeta_x \underline{f} + \zeta_y \underline{g} + \zeta_z \underline{h}) \\ \hat{G} &= J(\xi_x \underline{f} + \xi_y \underline{g} + \xi_z \underline{h}) \\ \hat{H} &= J(\eta_x \underline{f} + \eta_y \underline{g} + \eta_z \underline{h}) \end{aligned} \tag{13}$$

where the vectors, $\underline{q}$, $\underline{f}$, $\underline{g}$, and $\underline{h}$ are the vectors for the Euler equations written in Cartesian coordinates (see Chapter II). In the relations above, J is the Jacobian of the transformation from the physical plane (coordinates x,y,z) to the computational plane (coordinates ζ, ξ, η). The expression for the Jacobian is

$$J = x_\zeta y_\xi z_\eta + x_\xi y_\zeta z_\eta + x_\eta y_\zeta z_\xi - x_\eta y_\xi z_\zeta - x_\zeta y_\eta z_\xi - x_\xi y_\zeta z_\eta \qquad (14)$$

Equations (12), (13), and (14) are valid for transformation between any two coordinate systems. In this particular case, the coordinates, x, y, and z, represent respectively the axial, vertical, and horizontal Cartesian coordinates in which the Euler equations were first written. The coordinates, ζ, ξ, and η, represent respectively functions of the axial, radial, and circumferential directions of the cylindrical computational domain with the stretched grid spacing. They can be expressed as

$$\begin{aligned} \zeta &= f_1(x) \\ \xi &= f_2(r) \\ \eta &= f_3(\theta) \end{aligned} \qquad (15)$$

where

$$\begin{aligned} r &= (y^2 + z^2)^{1/2} \\ \theta &= \tan^{-1}\left(\frac{z}{y}\right) \end{aligned} \qquad (16)$$

and f_1, f_2, and f_3 are stretching functions. The ζ, ξ, and η coordinates "unwrap" to form the computational space with equal spacing between coordinate lines. A point to point correlation between the

physical space and the computational space is given in figure 1 and discussed in Chapter II.

Numerical Method

Algorithm. The computational technique employs the approximately-factored alternating-direction implicit numerical algorithm of Beam and Warming in its delta form.[17] The delta form of the Beam and Warming scheme has the advantage that the steady state solution, if one exists, is independent of the size of the time step. The algorithm, including stability and accuracy limitations, is described in detail for two dimensions by Warming and Beam;[20] therefore only a brief outline of the method will be presented here.

The algorithm is developed by first applying an Euler implicit formula between time levels n and $n+1$ to express the vector $\hat{q}^{n+1}$ of the transformed Euler equations (12) in terms of $\hat{q}^{n}$. Then by applying a linearization procedure to the vectors $\hat{F}$, $\hat{G}$, and $\hat{H}$, using a local Taylor expansion about $\hat{q}^{n}$, the Euler equations can be written in the form

$$\left\{I + \Delta t\left(\frac{\partial}{\partial \zeta} A^{n} + \frac{\partial}{\partial \xi} B^{n} + \frac{\partial}{\partial \eta} C^{n}\right)\right\} \Delta \hat{q}^{n+1} =$$

$$-\Delta t\left(\frac{\partial}{\partial \zeta} \hat{F}^{n} + \frac{\partial}{\partial \xi} \hat{G}^{n} + \frac{\partial}{\partial \eta} \hat{H}^{n}\right) + O(\Delta t^{2}) \qquad (17)$$

where I is the identity matrix. The term in the braces on the left-hand side of the equation (17) operates on $\Delta \hat{q}^{n+1}$ where

$$\Delta\hat{q}^{n+1} = \hat{q}^{n+1} - \hat{q}^{n} \tag{18}$$

The terms A^n, B^n, and C^n are Jacobian matrices defined as

$$A^n = \frac{\partial \hat{F}^n}{\partial \hat{q}}, \qquad B^n = \frac{\partial \hat{G}^n}{\partial \hat{q}}, \qquad C^n = \frac{\partial \hat{H}^n}{\partial \hat{q}} \tag{19}$$

Equation (15) is then approximately factored giving

$$\left(I + \Delta t \frac{\partial}{\partial \zeta} A^n\right)\left(I + \Delta t \frac{\partial}{\partial \xi} B^n\right)\left(I + \Delta t \frac{\partial}{\partial \eta} C^n\right)\Delta\hat{q}^{n+1} =$$

$$-\Delta t\left(\frac{\partial}{\partial \zeta} \hat{F}^n + \frac{\partial}{\partial \xi} \hat{G}^n + \frac{\partial}{\partial \eta} \hat{H}^n\right) \tag{20}$$

The factorization of equation (17) produces additional terms which are on the order of Δt^2 and hence do not destroy the temporal accuracy of the scheme. However the present studies indicate that, in three dimensions, the additional terms may seriously degrade the stability characteristics of the algorithm. This property of the algorithm will be discussed in detail later. The spatial derivatives in equation (20) are approximated by second-order central-difference operators yielding a block-tridiagonal system of equations to be solved in each of the three directions ζ, ξ, and η. The alternating-direction-implicit sequence for determining $\hat{q}^{n+1}$ is

$$\left(I + \Delta t \frac{\partial}{\partial \zeta} A^n\right)\Delta W^{n+1} = -\Delta t\left(\frac{\partial}{\partial \zeta} \hat{F}^n + \frac{\partial}{\partial \xi} \hat{G}^n + \frac{\partial}{\partial \eta} \hat{H}^n\right)$$

$$\left(I + \Delta t \frac{\partial}{\partial \xi} B^n\right)\Delta V^{n+1} = \Delta W^{n+1}$$

$$\left(I + \Delta t \frac{\partial}{\partial \eta} C^n\right)\Delta \hat{q}^{n+1} = \Delta V^{n+1} \tag{21}$$

$$\hat{q}^{n+1} = \Delta \hat{q}^{n+1} + \hat{q}^n$$

Numerical dissipation. In order to obtain solutions, it was necessary to add dissipation terms to equation (20) to damp numerical pertubations of short wavelengths and prevent odd-even point decoupling.[21,22] The fourth-order term

$$\omega_e\left(\frac{\partial^4}{\partial \zeta^4} \hat{q}^n + \frac{\partial^4}{\partial \xi^4} \hat{q}^n + \frac{\partial^4}{\partial \eta^4} \hat{q}^n\right) \tag{22}$$

was added to the right-hand side of the equation, and the third-order terms

$$\omega_i \frac{\partial}{\partial t} \frac{\partial^2}{\partial \zeta^2} \Delta \hat{q}^{n+1}, \quad \omega_i \frac{\partial}{\partial t} \frac{\partial^2}{\partial \xi^2} \Delta \hat{q}^{n+1}, \quad \omega_i \frac{\partial}{\partial t} \frac{\partial^2}{\partial \eta^2} \Delta \hat{q}^{n+1} \tag{23}$$

were added to the appropriate factors on the implicit left-hand side. The value of the explicit damping coefficient, ω_e, is set equal to Δt, and the value of the implicit damping coefficient, ω_i, is set equal to $2\omega_e$ in the manner of Pulliam and Steger.[22] For the numerical calculations, the derivatives in the dissipation terms are approximated by

finite-difference formulas. It should be noted that although numerical dissipation can stabilize a solution process, it has the disadvantage of causing a loss of accuracy in regions of strong gradients.

Recently, Abarbanel, Dwoyer, and Gottlieb[23] have proven that the undamped Beam and Warming scheme in three dimensions is weakly, but unconditionally, unstable for the Euler equations. Their work, which has been accomplished since the present research was initiated, shows that the instability is very weak and is only present in the very long wavelengths. Numerical experiments conducted in the present investigation indicate that the dissipation terms described above do not fully stabilize the solution process. However, the experiments also show that the weak long-wavelength instability takes a very large number of time steps to develop near the body. For a reasonable number of time steps (~ 1000), reasonably accurate solutions were obtained.

Metric calculation. If the scheme is applied in a uniform free stream, it is expected that uniform free-stream conditions would be exactly maintained. In three dimensions, however, errors in the uniform flow can be introduced since the transformed flux terms being differenced in equation (20) contain the metric derivatives. These errors can be avoided by using the proper averaging technique when numerically calculating the metric derivatives as pointed out by Pulliam and Steger.[22]

Since three-point central-difference operators are used to evaluate the flux terms of equation (18), the errors will exactly cancel if, for example, ζ_x is calculated by the equation

$$(\xi_x)_{i,j,k} = \frac{1}{J}_{i,j,k}\{[(\delta_j y_{i,k+1} + \delta_j y_{i,k-1})/2] -$$
$$\times [(\delta_k z_{i,j+1} + \delta_k z_{i,j-1})/2] - [(\delta_k y_{i,j+1}$$
$$+ \delta_k y_{i,j-1})/2][(\delta_j z_{i,k+1} - \delta_j z_{i,k-1})/2]\} \qquad (24)$$

and the other metric derivatives are calculated in a similar manner. In equation (24), δ_j and δ_k are the three point central difference operators in the j and k directions, respectively. The metric derivatives were computed by this technique to hold numerical errors to a minimum and consequently enhance the stability of the computational procedure.

Boundary Conditions

Inflow boundary. The analytical boundary conditions were covered in the previous chapter. The numerical boundary conditions, necessary to complete the differencing equations in the finite difference scheme, will now be specified for the implicit algorithm. At the inflow boundary, the analytical boundary conditions are met by specifying the total pressure, total temperature, and inflow angle. The static pressure is the remaining unknown on the boundary and must be numerically determined. It must obey the compatability relations along the characteristic connecting the inflow boundary with the interior solution. Compatability is approximated by extrapolating the pressure from within the computational domain.

Outflow boundary. At the outflow boundary, the analytical boundary condition is the specification of the static pressure. Two basic methods were used to specify the static pressure for the implicit numerical

scheme. The first technique evaluated was setting the boundary pressure equal to the free-stream value, i.e.

$$p = p_\infty \tag{25}$$

In addition to this method, a radiation boundary condition based on a solution to the three-dimensional wave equation

$$\hat{p}_{tt} = \nabla^2 \hat{p} \tag{26}$$

where

$$\hat{p} = p - p_\infty \tag{27}$$

was tested. Bayliss and Turkel[24] derived the radiation boundary condition and applied it in two dimensions with good results. During the present research, the radiation boundary condition was transformed to a three-dimensional form and applied to the flow-through nacelle problem.

In the far field where pertubations are small, the three-dimensional Euler equations assume the form of equation (26) when linearized and transformed by the relations

$$\bar{\zeta} = (1 - M^2)^{-1/2} x$$

$$\tau = a_\infty (1 - M_\infty^2)^{1/2} t + M_\infty \bar{\zeta} \tag{28}$$

$$y = y$$

$$z = z$$

If spherical coordinates are also introduced,

$$\hat{r}^2 = \bar{\zeta}^2 + y^2 + z^2$$

$$\theta = \tan^{-1}\left(\frac{y}{\bar{\zeta}}\right) \tag{29}$$

$$\phi = \tan^{-1}\left(\frac{z}{\bar{\zeta}}\right)$$

equation (26) has solutions of the asymptotic form

$$\hat{p} = \frac{f(\tau - \hat{r}, \theta, \phi)}{\hat{r}} \tag{30}$$

for large τ and $\hat{r}$. The functional form in equation (30) represents an outgoing spherical wave solution to (26). The specific function, f, is not usually known. However, the condition

$$\frac{\partial \hat{p}}{\partial \tau} + \frac{\partial \hat{p}}{\partial \hat{r}} + \frac{\hat{p}}{\hat{r}} = 0 \tag{31}$$

is exact for all functions which identically have the form (30).

Equation (31) is the analytic boundary condition used at the outflow boundary. Transforming back to the physical plane (coordinates t,x,y,z) gives

$$p^{n+1} = \left\{\left[\frac{1}{\Delta t(a_\infty^2 - u_\infty^2)^{1/2}}\right]p^n + \left[\left(\frac{\rho_\infty a_\infty^2}{a_\infty^2 - u_\infty^2}\right)\left(\frac{x}{r}\right)\right]u_t + \left[\rho_\infty\left(\frac{y}{r}\right)\right]v_t + \left[\rho_\infty\left(\frac{z}{r}\right)\right]w_t + \left(\frac{1}{r}\right)p_\infty\right\}\left\{\left[\frac{1}{\Delta t(a_\infty^2 - u_\infty^2)^{1/2}}\right] + \frac{1}{r}\right\}^{-1} \tag{32}$$

where

$$r = (x^2 + y^2 + z^2)^{1/2} \tag{33}$$

and the superscript, n, indicates the time step. During transient periods, equation (32) allows impinging pressure waves to pass through the outflow boundary more effectively than equation (25). At steady state, equation (32) reduces to equation (25). In the implementation of both boundary equations, (32) and (25), the flow quantities other than the static pressure are obtained from the interior of the computational domain by zeroth order extrapolation.

In addition to the two basic outflow boundary conditions just described, the nonreflecting outflow boundary condition of Rudy[25] was tested briefly with mixed results. The Riemann-invariant method described in the next chapter was also tried in conjunction with the implicit

computational technique. An equally brief investigation of this combination failed to yield a satisfactory solution.

Far-Field boundary. The treatment of the far-field boundary depended on whether outflow boundary condition (25) or (32) was used. When outflow boundary equation (25) was used, all the flow quantities on the boundary were obtained by zeroth order extrapolation from interior points. When the radiation equation, (32), was applied, it was simultaneously applied at both the outflow and far-field boundaries (see figure 2) as suggested by Bayliss and Turkell.[24] In the application of the radiation condition at the far-field boundary, p_∞ in the right-hand side of equation (32) was replaced by the local value of the pressure at the previous time step.

A more precise treatment of the far-field boundary would be to test each point on the boundary at each time step for an inflow or an outflow condition and treat the point accordingly. However, since the boundary is relatively far from the nacelle, and the velocities normal to the boundary are very low in comparison to the free-stream velocity, the less complicated treatments were chosen for the calculation at 0^o angle of attack. For calculations with the nacelle at angle of attack, inflow boundary conditions are assigned to the lower half of the far-field boundary and outflow boundary conditions to the upper half.

Surface boundary. For an inviscid fluid, the boundary condition at an impermeable surface is that the flow is tangent to the surface. This condition is expressed at the nacelle surface by equating the contravariant velocity which is not tangent to the surface to zero.

$$\underline{V} = \xi_x \underline{u} + \xi_y \underline{v} + \xi_z \underline{w} = 0 \qquad (34)$$

By using this expression and combining the three momentum equations in the manner of Pulliam and Steger,[22]

$$\xi_x(\text{x-momentum equation}) + \xi_y(\text{y-momentum equation}) + \xi_z(\text{z-momentum equation}) = 0 \tag{35}$$

the following relation which is independent of time can be obtained for the surface pressure:

$$ap_\zeta + bp_\xi + cp_\eta = d \tag{36}$$

where

$$\begin{aligned} a &= \xi_x\zeta_x + \xi_y\zeta_y + \xi_z\zeta_z \\ b &= \xi_x^2 + \xi_y^2 + \xi_z^2 \\ c &= \xi_x\zeta_x + \xi_y\zeta_y + \xi_z\zeta_z \\ d &= -\rho\underline{U}(\xi_x u_\zeta + \xi_y v_\zeta + \xi_z w_\zeta) \\ &\quad -\rho\underline{W}(\xi_x u_\eta + \xi_y v_\eta + \xi_z w_\eta) \end{aligned} \tag{37}$$

and $\underline{U}$ and $\underline{W}$ are the contravariant velocity components tangent to the

nacelle surface.

$$\underline{U} = \zeta_x \underline{u} + \zeta_y \underline{v} + \zeta_z \underline{w}$$

$$\underline{W} = \eta_x \underline{u} + \eta_y \underline{v} + \eta_z \underline{w} \qquad (38)$$

Equation (36) is solved for the surface pressure by first extrapolating ρ, $\underline{U}$, and $\underline{W}$ along the ξ coordinate to the nacelle using a first-order procedure. Then p_ξ is expressed as a second-order one-sided finite-difference formula, and p_ζ and p_η are written as second-order central difference formulas. The resulting equation is then approximately factored, and a series of tridiagonal equations in the ζ and η directions are numerically solved to yield the surface values.

Leading and trailing edges. The implicit finite-difference computational procedure requires a direct treatment of the leading and trailing edge boundaries, and a wide variety of the treatments was attempted in the present work. Solutions to the Euler equations at such points require careful treatment in order to overcome the mathematical difficulties while at the same time maintaining correct physical behavior. For example, the condition of tangency of the flow to the nacelle surface necessitates that stagnation conditions exist at the sharp leading and trailing edges. However, for the grid spacings investigated, specifying stagnation conditions at the leading and trailing edges resulted in large jumps in the flow quantities in the immediate vicinity of these points. A more accurate solution is obtained by the following approximate treatment of the leading and trailing edge boundaries.

At the leading edge, the density and contavariant velocities are extrapolated along the internal and external surfaces of the nacelle. The condition that the total enthalpy is constant plus the extrapolated quantities determines the thermodynamic and kinetic properties of the leading edge flow. The internal and external surfaces are treated separately and the tangency condition is maintained on each surface.

The densities and contravariant velocities are also extrapolated along the internal and external surfaces to the trailing edge. The pressure at the trailing edge is determined from the external values and the condition that the total enthalpy is constant. A discontinuity in the density and in the magnitude of the velocities is allowed between the internal and external surfaces.

Best agreement between the inviscid computations and the experimental pressures on the inside of the nacelle were obtained when a Kutta-like condition was adopted at the trailing edge. It consisted of setting the flow angle at the trailing edge equal to the angle of the internal surface of the nacelle. The primary results presented for the implicit procedure in Chapter VI are calculated using this boundary condition. However, further numerical studies show that instead of giving the correct inviscid solution, the Kutta-like condition actually models viscous effects present in the experimental data. These results and their implications are presented in Chapter VII.

CHAPTER IV

EXPLICIT COMPUTATIONAL PROCEDURE

In addition to the implicit finite-difference numerical procedure described in Chapter III, an explicit finite-volume procedure which employed a fourth-order Runge-Kutta numerical algorithm was also evaluated. The algorithm has been applied to both two and three-dimensional problems, and appears to give accurate and stable solutions in both cases.[11-13] The main advantage of explicit schemes is that the updated solution at a new time step is independently calculated at each grid point or cell. Thus, sets of algebraic equations do not have to be solved as they do for implicit methods. The disadvantage of explicit numerical algorithms is that the grid spacing imposes stability limitations on the size of the time step when integrating the flow equations. Thus, less computational work is required at each time step, but more time steps are normally needed. The limitation on the size of the time step is most restrictive for viscous solutions where the grid spacing must be very fine in order to adequately define the boundary layer. For inviscid solutions, the restriction is much less severe.

Unlike the implicit computational procedure, the explicit procedure was not completely developed in the present study, but was adapted to the nacelle problem from an existing computer code written by Jameson and Baker.[13] The adaptation consisted mainly of changing the logic of the code to allow for both internal and external nacelle surfaces on an H-type

grid. Essentially, the explicit interior point algorithm and boundary treatments were inserted into the overall framework developed for the implicit code. The adaptation also involved reprogramming some of the boundary conditions for the H grid. This chapter describes the application of the explicit algorithm to the nacelle problem.

Finite Volume Formulation.

The basic principles of the explicit procedure are covered thoroughly in references 11, 12, and 13; therefore only a brief outline of the procedure will be presented here. The Euler equations, (1), can be written in integral form as

$$\frac{\partial}{\partial t}\int_V q\,dV + \int_S \bar{F}\cdot ds = 0 \tag{39}$$

where q is the vector of conserved quantities (dependent variables) presented in equations (1), V is the volume of the domain, S is its surface area, and $\bar{F}$ is

$$\bar{F} = \begin{bmatrix} \rho u, & \rho v, & \rho w \\ \rho u^2 + p, & \rho uv, & \rho uw \\ \rho uv, & \rho v^2 + p, & \rho vw \\ \rho uw, & \rho vw, & \rho w^2 + p \\ \rho uH, & \rho vH, & \rho wH \end{bmatrix} \tag{40}$$

The commas separate the x, y, and z, or physical, components of $\bar{F}$. No transformations are necessary with the finite-volume formulation.

Numerical Method

Algorithm. To integrate the equations over the computational domain, the explicit procedure uses the four-stage Runge-Kutta numerical algorithm in its standard form. For a linear system of equations

$$\frac{\partial q}{\partial t} + P(q) = 0 \tag{41}$$

the four-stage scheme can be written as

$$\begin{aligned} q^{(0)} &= q^n \\ q^{(1)} &= q^{(0)} - a_1 p(0) \\ q^{(2)} &= q^{(0)} - a_2 p(1) \\ q^{(3)} &= q^{(0)} - a_3 p(2) \\ q^{(4)} &= q^{(0)} - p(3) \\ q^{n+1} &= q^{(4)} \end{aligned} \tag{42}$$

where q^n and q^{n+1} are the values of the dependent variables at time steps n and $n+1$ respectively. For the standard scheme, the values for the coefficients, a, are

$$a_1 = \frac{1}{4}, \quad a_2 = \frac{1}{3}, \quad a_3 = \frac{1}{2} \tag{43}$$

These coefficients give the scheme a numerical stability bound which allows a maximum Courant number of $2\sqrt{2}$.

Before the Euler equations can be numerically integrated by using the Runge-Kutta algorithm, they must be discretised. In the present procedure, dissipation terms are also appended to the discretised equations before the solution process is begun. The next two sections describe the discretization process and dissipation terms.

Discretised equations. The Euler equations are spatially discretised by approximating them in integral form in each cell of the computational domain. Note that the computational grid divides the domain into a system of adjoining hexagonal cells. The discretised equations for a cell are

$$v_{i,j,k} \frac{d}{dt} (q)_{ijk} + \sum_{\ell} (S_{\ell} \cdot \bar{F}_{\ell})_{ijk} = 0 \qquad (44)$$

where the indices i,j,k identify the center of the cell, and v is the differential cell volume which is independent of time. The summation on the subscript, ℓ, denotes summation on all six faces of the hexagonal cell. At each face, the dot product between the face area, S, and the flux tensor, $\bar{F}$, is evaluated as

$$S \cdot \bar{F} = S_x \bar{F}_x + S_y \bar{F}_y + S_z \bar{F}_z \qquad (45)$$

where the subscripts x, y, and z indicate components in the physical directions. Since the intermediate solution, the solution at time level n, is known at each cell center, the flux at each cell face is evaluated

by averaging the fluxes at the centers of adjacent cells. For example, for a typical face, I, located at $i+1/2,j,k$ with adjacent cell centers at i,j,k and $i+1,j,k$, the mass flux at time level n would be

$$(\rho u)_I = \frac{1}{2}\{(\rho u)_{i,j,k} + (\rho u)_{i+1,j,k}\} \tag{46}$$

This method of averaging amounts to using central differences in a finite difference formulation, and yields second order spatial accuracy in the absence of any dissipation terms.

Approximating the time derivatives with a forward difference formula and solving for q^{n+1} gives

$$q^{n+1} = q^n - \frac{\Delta t}{v_{i,j,k}} \sum_{\ell} (S_\ell \cdot \bar{F}_\ell)_{i,j,k} \tag{47}$$

which completes the discretization of the integral form of the Euler equations.

Numerical dissipation. Equation (47) is in a form compatible with the Runge-Kutta numerical algorithm. However, to insure numerical stability, dissipation terms are appended to the right-hand side of the equation before the solution process begins. The dissipation terms are the same as those used by Jameson et. al. in reference 13. The augmented form of the equations is

$$q^{n+1}_{i,j,k} = q^n_{i,j,k} - \frac{\Delta t}{v_{i,j,k}} \left\{ \sum_{\ell} (S_\ell \cdot F_\ell)_{i,j,k} + D_{i,j,k} \right\} \tag{48}$$

where $D_{i,j,k}$ represents the dissipation terms in all three computational directions (directions ζ, ξ, and η).

$$D_{i,j,k} = (D_\zeta + D_\xi + D_\eta)_{i,j,k} \tag{49}$$

The damping terms are composed of third order terms (fourth-order differences) which prevent odd-even point decoupling , and first order terms (second-order differences) which prevent preshock oscillations.

The third order terms are similar to the ones appended to the implicit procedure, and are formed by taking the fourth-order differences of the dependent variables along each of the computational coordinate directions. Taking the ζ direction as an example gives

$$(D^{(4)}_\zeta)_{i,j,k} = d^{(4)}_{i+1/2,j,k} - d^{(4)}_{i-1/2,j,k} \tag{50}$$

where

$$d^{(4)}_{i+1/2,j,k} = \omega^{(4)} \frac{(v_i + v_{i+1})_{j,k}}{2\Delta t} (q_{i+2} - 3q_{i+1} + 3q_i - q_{i-1})_{j,k} \tag{51}$$

and $d^{(4)}_{i-1/2,j,k}$ is calculated by a corresponding formula. The term, $(v_i + v_{i+1})_{j,k}/2\Delta t$ insures that the units are consistent in equation (48). Similar terms are formed for the ξ and η directions. These dissipation terms are spatially accurate to the third order, and hence do not compromise the accuracy of the spatial discretization of the Euler equations which is second order.

In addition to the third-order dissipation just discussed, first-order dissipation is necessary in the vicinity of shocks to prevent preshock oscillations. These terms are formed by taking second-order differences of the dependent variables, and have the form

$$(D_\zeta^{(2)})_{i,j,k} = -\omega^{(2)} \nu \left\{ \varepsilon_{i+1/2} \frac{\nu_{1+1/2}}{\Delta t} (q_{i+1} - q_i) - \varepsilon_{i-1/2} \frac{\nu_{i-1/2}}{\Delta t} (q_i - q_{i-1}) \right\} \tag{52}$$

where ν and ε form a switch sensitive to the second differences in pressure.[13] Their formulas for the face located at i+1/2 are

$$\nu_{i,j,k} = \frac{|p_{i+1,j,k} - 2p_{i,j,k} + p_{i-1,j,k}|}{|p_{i+1,j,k} + 2p_{i,j,k} + p_{i-1,j,k}|} \tag{53}$$

and

$$\varepsilon_{i+1/2} = \max(\nu_{i+1,j,k}, \nu_{i,j,k}) \tag{54}$$

Similar formulas are used to calculate ν and ε at i-1/2,j,k. Near pressure discontinuites such as shocks, the first order dissipation terms become very large, and the scheme is first order accurate. Whenever the pressure variations are smooth, the first order terms are negligible, and the scheme remains spatially second order accurate.

The numerical dissipation just discussed is added to equation (47) at all four stages of the Runge-Kutta algorithm. However, the damping terms are updated only at the beginning of each time step, and are not recalculated between the stages of the scheme.

Implicit smoothing. In the present explicit method, like reference 13, the stability bound is increased by applying implicit smoothing to the residuals which are calculated explicitly. The smoothing method is similar to the class of numerical algorithms suggested by Lerat,[26] and takes the form

$$(1 - \bar{\varepsilon}\,\delta_\zeta^2)(1 - \bar{\varepsilon}\,\delta_\xi^2)(1 - \bar{\varepsilon}\,\delta_\eta^2)\hat{P}_{i,j,k} = P_{i,j,k} \tag{55}$$

where $\hat{P}$ is the smoothed residual. The smoothing operators are applied as factors operating on $\hat{P}$ in the transformed directions. Therefore only three separate tridiagonal equations must be solved to determine the smoothed value of the residuals.

Convergence acceleration. Convergence to a steady state solution is accelerated in the computational procedure by two methods.[13] First the maximum allowable time step is used for a given Courant number at each individual cell. Using a variable time step destroys the temporal accuracy of the solution technique, but that is of relatively little concern since the steady state is the solution of interest. A variable time step is equivalent to making the following modification to the Euler equations

$$\frac{\partial q}{\partial t} + \beta I\left|\frac{\partial f}{\partial x} + \frac{\partial g}{\partial y} + \frac{\partial h}{\partial z}\right| = 0 \tag{56}$$

where β is a scalar multiplier and I is the identity matrix. Thus β can be chosen individually for each cell to advance the solution at the maximum Courant number.

The second method of enhancing convergence is by including a forcing function in the Euler equations proportional to the difference between the local enthalpy and the free-stream enthalpy. With the addition of this term, the modified form of the equations becomes

$$\frac{\partial q}{\partial t} + \frac{\partial f}{\partial x} + \frac{\partial g}{\partial y} + \frac{\partial h}{\partial z} + \bar{A}(H - H_\infty) = 0 \tag{57}$$

where

$$\bar{A}(H - H_\infty) = \begin{bmatrix} \bar{a}\rho(H - H_\infty) \\ \bar{a}\rho u(H - H_\infty) \\ \bar{a}\rho v(H - H_\infty) \\ \bar{a}\rho w(H - H_\infty) \\ \bar{a}\ (H - H_\infty) \end{bmatrix} \tag{58}$$

and $\bar{a}$ is a constant. At steady state, $H = H_\infty$, so the steady state Euler equations remain unaltered when the enthalpy damping term is included. Jameson also shows that in the absence of shocks, the flow would remain irrotational and homentropic.[12] The enthalpy damping function acts similar to the ϕ_t term of the telegraph equation

$$\phi_{tt} + a\phi_t = \phi_{xx} + \phi_{yy} \tag{59}$$

where in relaxation methods, ϕ_t plays an important role in determining the rate of convergence.

Boundrary Conditions

Inflow boundary. The treatment of the inflow, outflow, and far-field boundaries is based on the Riemann invariants for a one-dimensional flow normal to the boundary.[13] For a one-dimensional flow, the Riemann invariants and the characteristics along which they apply are

characteristic	Riemann invariant
$\frac{dx}{dt} = u + a$	$R = u + \frac{2a}{\gamma - 1}$
$\frac{dx}{dt} = u - a$	$R = u - \frac{2a}{\gamma - 1}$

(60)

where R is the value of the Riemann invariant, u is the velocity normal to the boundary, and a is the speed of sound.

In applying the Riemann invariants to calculate the numerical boundary conditions, the values of u and a are determined from the flow variables in the regions where the respective characteristics originate. For the inflow boundary depicted in figure 1, the characteristic originating from outside the computational domain is $dx/dt = u + a$. Therefore, the value of the corresponding Riemann invariant is calculated by the formula

$$R_\infty = \underline{U}_\infty \cdot \underline{n} + \frac{2a_\infty}{\gamma - 1} \tag{61}$$

where $\underline{n}$ is the unit normal to the boundary and $\underline{U}_\infty$ is the velocity of the free-stream. The Riemann invariant for the characteristic originating inside the computational region, $dx/dt = u - a$, is

$$R_{int} = \underline{U}_{int} \cdot \underline{n} - \frac{2a_{int}}{\gamma - 1}$$

$$\underline{U}_b \cdot \underline{n} = \frac{1}{2} (R_\infty + R_{int}) \tag{62}$$

where the subscript, int, indicates the interior of the domain. In making this calculation, the values of $\underline{U}_{int}$ and $\underline{a}_{int}$ are computed from the properties of the flow variables in the cell next to the boundary. The equations for the two invariants, (61) and (62), can be combined to yield the normal velocity and the speed of sound at the boundary.

$$a_b = \frac{\gamma - 1}{4} (R_\infty - R_{int}) \tag{63}$$

where the subscript, b, indicates boundary values.

This procedure for calculating the normal velocity and speed of sound is equivalent to specifying one boundary condition and numerically calculating another. Consistency with the analytical boundary conditions discussed in Chapter III must be maintained. Therefore, at the inflow boundary where four conditions must be supplied, the tangential velocities and entropy are set equal to their free stream values. The three velocity components, the speed of sound, and the entropy completely determine the dependent variables at the inflow boundary.

Outflow boundary. The outflow boundary is treated in a similar manner. However, the characteristics entering and leaving the computational domain are reversed, resulting in the new equations for the normal velocity and speed of sound

$$\underline{U}_b \cdot \underline{n} = \frac{1}{2}(R_{int} + R_\infty)$$

$$a_b = \frac{\gamma - 1}{4}(R_{int} - R_\infty) \tag{64}$$

On the outflow boundary, the entropy and tangential velocities are extrapolated from the interior of the computational domain. Thus, the treatment of the outflow boundary is also consistent with the number and form of the analytical boundary conditions given by characteristic theory.

Far-field boundary. The far-field boundary is treated as an inflow boundary where the normal velocity is the vector sum of the velocities in the y and z directions, or v and w respectively.

Surface boundary. The surface boundary creatment is very similar to the treatment for the implicit procedure. The concept is the same; however it is applied slightly differently to the finite volume formulation used in the explicit numerical procedure. For the finite volume formulation, the pressure is the only flow quantity required on the body surface. A brief overview of the method, which was proposed by Rizzi[27] and used in reference 13, follows.

The boundary condition for a solid body in inviscid flow is that the flow is tangent to the surface, equation (11). Taking the total

derivative of the flow tangency condition with respect to time

$$\left(\frac{\partial}{\partial t} + \underline{V}\cdot\text{grad}\right)\ (\underline{V}\cdot\underline{n}) = 0 \tag{65}$$

(where $\underline{V}$ is the velocity at the surface and $\underline{n}$ represents the unit vector normal to the surface) and substituting it into the inner product of $\underline{n}$ and the momentum equations yields

$$\rho\underline{V}\cdot(\underline{V}\cdot\text{grad})\underline{n} = \underline{n}\cdot\text{grad}(p) \tag{66}$$

for a stationary body. For a general nonorthogonal grid, equation (66) can be expressed in the form

$$\rho\left[W^1\left(u_1\frac{\partial n_1}{\partial \zeta^1}\right) + W^3\left(u_1\frac{\partial n_1}{\partial \zeta^3}\right)\right] = g^{m2}\frac{\partial p}{\partial \zeta^m} \tag{67}$$

where

$$u_1 = \frac{dx_1}{dt}, \qquad W^1 = \frac{d\zeta^1}{dt}, \qquad W^3 = \frac{d\zeta^3}{dt}, \qquad g^{m2} = \frac{\partial \zeta^m}{\partial x_\ell}\frac{\partial \zeta^2}{\partial x_\ell} \tag{68}$$

and double indices indicate summation as in tensor notation.

In equation (67), Rizzi substitutes the flow quantities at the nearest field point for those on the body surface. This yields a first-order accurate boundary method which is consistent with the accuracy of

the second-order interior scheme and gives an overall solution accuracy of second order. Thus, the gradient of the pressure along the coordinate line intersecting the surface, ξ, can be evaluated, and then the pressure can be extrapolated to the body.

CHAPTER V

VISCOUS-INVISCID INTERACTING COMPUTATIONAL MODEL

Chapters III and IV respectively describe an implicit and an explicit computational procedure for solving the three-dimensional Euler equations for the flow past a flow-through nacelle. However, the Euler equations, which model compressibility and rotationality, do not model viscous stresses. In the physically realistic case, strong interactions often occur between the viscous boundary layer and the main stream even when the boundary layer does not separate. In these instances, modeling the frictional forces becomes essential if accuracy is to be maintained. Therefore, to complete the study of the flow field surrounding the flow-through nacelle, a procedure with which to assess the viscous effects was needed.

To obtain a computational technique which simulated viscous effects, the explicit Euler solution procedure was coupled with a boundary layer solution procedure. The resulting viscous-inviscid interacting computational model is based on a global iteration between the integration of the Euler equations and the boundary layer equations. The present chapter describes this interacting computational model.

Boundary Layer Equations

Since the objective of the viscous-inviscid interaction phase of the research was to evaluate the viscous effects on the nacelle pressures, a

boundary layer solution procedure that was well validated was desired. The inviscid calculations and the wind-tunnel data indicate that the flow on the nacelle remains attached. Therefore an integral technique used in the direct mode was considered applicable.[28] Green's[29] compressible, axisymmetric, "lag entrainment" method solved in the direct mode was chosen because of its reliability.

The method involves the integration of three ordinary differential equations: the momentum integral equation, an entrainment equation, and a rate equation for the entrainment coefficient.

$$\frac{d\theta}{dx} = \left[\frac{RC_f}{2} - (H + 2 - M^2)\frac{R}{U_e}\left(\frac{dU_e}{dx}\right) - \theta\frac{dR}{dx}\right]\Big/ R$$

$$\frac{d\bar{H}}{dx} = \frac{dH}{dH_1}\left[C_e - H_1\left(\frac{C_f}{2} - (H + 1)\frac{\theta}{U_e}\frac{dU_e}{dx}\right)\right]\Big/\theta \qquad (69)$$

$$\frac{dC_e}{dx} = \left[\frac{F}{\theta}\frac{2.8}{H - H_1}\left((C_\tau)_{eq_\infty}^{1/2} - \lambda C_\tau^{1/2}\right) + \left(\frac{\theta}{U_e}\frac{dU_e}{dx}\right)\right.$$

$$\left. - \frac{\theta}{U_e}\frac{dU_e}{dx}\left(1 + .075M^2\frac{(1 + .2M^2)}{(1 + .1M^2)}\right)\right]$$

The momentum integral equation, the first equation, is obtaind by integrating in the direction normal to the wall both the continuity and streamwise momentum equations and combining the results. The entrainment equation, which is the second one, is obtained by integrating the continuity equation in the direction normal to the wall. The rate equation for the entrainment coefficient comes from a similar integration of the energy equation, and represents explicitly the balance between the

convection, production, diffusion, and dissipation of kinetic energy.

In the previous equations, θ is the momentum thickness and R the radius of the body. The shape factors are defined as:

$$H = \delta^*/\theta \qquad \text{(incompressible flow)}$$

$$\bar{H} = \delta^*/\theta \qquad \text{(compressible flow)} \tag{70}$$

$$H_1 = (\delta - \delta^*)/\theta$$

where δ is the boundary layer thickness, δ^* the displacement thickness, and the emperical relationships

$$H_1 = 3.15 + \frac{1.72}{\bar{H} - 1} - 0.01(H - 1)^2$$

$$H + 1 = (\bar{H} + 1)\left(1 + \frac{rM^2}{5}\right) \tag{71}$$

exist between H, $\bar{H}$, and H_1. The term, r, is the temperature recovery factor. The entrainment coefficient is defined by

$$C_e = \frac{1}{r\rho_e U_e} \frac{d}{dx}(r\rho_e U_e H_1 \theta) \tag{72}$$

and the term, F, by

$$F = \frac{(0.02C_e + C_e^2 + 0.8\, C_{f_0}/3)}{(0.01 + C_e)} \tag{73}$$

where C_{f_0} is the equilibrium skin-friction coefficient at zero pressure

gradient. The term C_f is the skin-friction coefficient and C_τ is the shearing-stress coefficient.

These boundary layer equations are integrated by a variable order, variable interval Adams method. The method is part of the Langley Cyber 200 mathematical library[30] and is recomended for sets of stiff first-order ordinary differential equations.

Viscous-Inviscid Interacting Theory

Matching conditions. The global viscous-inviscid interacting technique depends upon a coupling of the inviscid Euler equations and the boundary layer equations through conventional transpiration boundary conditions. As pointed out by Thomas[31], for the inviscid Euler solution to simulate a solution with viscous effects, it must match the vicous solution in that part of the flowfield where the inviscid and viscous equations both describe the flow accurately. The matching conditions for the Euler equations are described for two dimensions in his dissertation.

The viscous-inviscid interaction technique presently used to assess the viscous effects on the nacelle uses a three-dimensional adaptation of the two-dimensional matching procedure. In both procedures, transpiration boundary conditions determined from a solution of the boundary layer equations are imposed at the body surface and in the wake of the body to enforce the boundary layer effects. An outline of the method used to determine the equivalent inviscid transpiration boundary conditions necessary to match the inviscid and viscous solutions follows.

For two-dimensional steady flow, the Navier Stokes equations are:

$$\frac{\partial F}{\partial x} + \frac{\partial G}{\partial y} = 0 \tag{74}$$

and the Euler equations are

$$\frac{\partial f}{\partial x} + \frac{\partial g}{\partial y} = 0 \tag{75}$$

Designate the point where both sets of equations describe the flow accurately by h. Then intergrating both sets of equations with respect to y over the range $0 \leq y < h$ and matching the solutions at $y \geq h$ yields

$$g_w = G_w + \frac{\partial}{\partial x}\int_0^h (f - F)\, dy \tag{76}$$

The subscript, w, indicates wall values and implies that the inner boundary of the inviscid solution is the nacelle wall. An advantage of choosing the wall as the inner boundary of the inviscid solution is that only one computational grid needs to be generated. Thomas follows the example of Johnston and Sochol,[32] and lets F be a composite function

$$F = f + \bar{f} - f_w \tag{77}$$

where $\bar{f}$ is from the boundary layer equations:

$$\frac{\partial \bar{f}}{\partial x} + \frac{\partial \bar{g}}{\partial y} = 0 \tag{78}$$

Substituting the composite function into equation (74) and performing the integration gives

$$g_w = \bar{g}_w + \frac{\partial}{\partial x}\int_0^h (f_w - \bar{f})\, dy \tag{79}$$

The resulting vector, g_w, is the Euler vector, g, at the nacelle surface when the Euler and Navier-Stokes layer solutions are properly matched at $y = h$. Using the continuity equation as an example, the equivalent inviscid boundary condition at the wall necessary to match the inviscid and viscous solutions is:

$$(\rho v)_w = \frac{d}{dx}\left[(\rho u)_w \delta^*\right] \tag{80}$$

Note that Johnston and Sochol use the inviscid wall values in determining the mass flux term on the right hand side of equation (80). This is the same equation as the one presented by Lock.[33] It states that the mass flow normal to the wall in the equivalent inviscid flow is equal to the streamwise rate of change of the mass flow deficit produced by the boundary layer.

The previous development of the transpiration boundary conditions is in two dimensions. However, the present computational technique solves the Euler equations in three dimensions. The steady three-dimensional Euler equations in vector form are

$$\frac{\partial f}{\partial x} + \frac{\partial g}{\partial y} + \frac{\partial h}{\partial z} = 0 \tag{81}$$

and contain, in addition to the vector g, the vector, h, which must also be determined at the wall. In determining these two vectors, advantage was taken of the axisymmetric nature of the nacelle. By

performing a mass balance for the flow between two axial stations, the wall, and the edge of the boundary layer, it can be shown that the axisymmetric equivalent of equation (80) is

$$(\rho \underline{V})_w = \frac{1}{r}\frac{d}{dx}\{(\rho u)_w(2r\delta^* + \delta^{*2})\} \tag{82}$$

where V is the velocity vector normal to the surface. For the three-dimensional adaptation, V is divided into components $\underline{v}$ and $\underline{w}$ in the vertical and horizontal directions respectively

$$\begin{aligned} \underline{V}_w &= (\underline{V}\cdot\underline{n}_y)_w \\ \underline{w}_w &= (\underline{V}\cdot\underline{n}_z)_w \end{aligned} \tag{83}$$

Due to the relatively small boattail angles of the nacelle, the axial component is neglected. The vectors, n_y and n_z, represent the y and z components of the unit normal to the surface. Using these quantities and the inviscid values of the tangent velocity, u_w, and pressure, p_w, at the surface, the equivalent inviscid vectors g_w and h_w can be evaluated at the surface of the nacelle where

$$\underline{g}_w = \begin{Vmatrix} \rho v \\ \rho uv \\ \rho v^2 + p \\ \rho vw \\ v(\rho E + p) \end{Vmatrix}_w, \qquad \underline{h}_w = \begin{Vmatrix} \rho w \\ \rho uw \\ \rho vw \\ \rho w^2 + p \\ w(\rho E + p) \end{Vmatrix}_w \tag{84}$$

Surface pressure equation. The surface pressure equation for a solid wall boundary with no flow across it, equation (67), was presented previously in Chapter IV. For convenience, it is repeated here

$$g^{m2}\frac{\partial p}{\partial \zeta^m} = \rho\left[W^1\left(u^j\frac{\partial n_j}{\partial \zeta^1}\right) + W^3\left(u^j\frac{\partial n_j}{\partial \zeta^3}\right)\right]$$

Allowing for flow across the solid boundary introduces an extra term and changes the surface pressure equation into

$$g^{m2}\frac{\partial p}{\partial \zeta^m} = \rho\left[W^1\left(u^j\frac{\partial n_j}{\partial \zeta^1}\right) + W^3\left(u^j\frac{\partial n_j}{\partial \zeta^3}\right)\right] - \rho\left[W^1\frac{\partial}{\partial \zeta^1}(n_j u^j) + W^3\frac{\partial}{\partial \zeta^3}(n_j u^j)\right] \qquad (85)$$

Computations with both forms of the surface pressure equation resulted in negligible differences in the solution. However, all viscous-inviscid interacting calculations presented in this dissertation were made with the modified form, equation (85).

Application of the Viscous-Inviscid Interaction Technique

The transpiration boundary conditions presented in equation (84) are applied on both the external and internal nacelle surfaces and also in the wake of the nacelle. In the wake application, the transpiration boundary conditions are imposed along the constant ξ coordinate surface starting at the nacelle trailing edge and extending approximately one half of the nacelle cord downstream. At this axial location, the wake boundary condition had decayed to a very low value. The wake is composed of the

boundary layers originating from both the external and the internal nacelle surfaces. Separate transpiration boundary conditions, calculated from each of these components of the wake, were imposed along the ξ = constant surface depending on whether the particular grid cell was on the outside or inside of the surface. However, when numerically integrating the Euler equations, fluxes were allowed to flow freely through the surface, and a pressure balance was maintained across it.

In the overall global iteration between the Euler and boundary layer solutions, the boundary layer equations are solved every 100 time steps of the Euler integration process using the current values of the viscous-inviscid solution. The transpiration boundary conditions are then updated using the new boundary layer solution and held constant until the next global iteration. The overall solution technique is started from a converged inviscid solution and is typically run for 1000 time steps which gives 10 iterations of the boundary layer. After the 10 overall global iterations, the solution has essentially ceased to change.

The transpiration boundary conditions described in the preceding sections physically displace the outer inviscid flow away from the surface to allow for the deceleration of the stream in the boundary layer. Hence they account for the displacement effects of the boundary layer. They do not account for wake curvature effects which are theoretically as important, but, in practice are usually smaller in magnitude.[34] Neither do they account for strong interaction effects such as the interaction between the boundary layer and a strong shock wave which results in a breakdown of the usual boundary layer approximations.[34]

CHAPTER VI

INVISCID RESULTS

Calculations were made with the two computational techniques described in Chapters III and IV for a flow-through nacelle at free-stream Mach numbers of 0.80 and 0.94, and at angles of attack of 0^{o} and 4^{o}. All computations were made on a Control Data Corporation Cyber 203 vector processor in the scalar mode. In this chapter, the results obtained with the alternating-direction-implicit computational procedure will be presented first, and then the results obtained with the explicit Runge-Kutta procedure. Several interesting difficulties which had a significant impact on the solutions were encountered and investigated in detail during the numerical studies. This aspect of the research will be discussed. The two techniques will be compared on the basis of quality of the solutions, and also on practical considerations in implementing and processing the resulting computer codes on the Cyber 203.

Implicit Computational Results

Basic solution. The results obtained with the alternating-direction-implicit computational procedure are presented in figures 4 through 8. Figure 4 presents the basic solution for the nacelle at a free stream Mach number of 0.80 and an angle of attack of 0^{o}. Wind-tunnel data of Re and Peddrew[35] are included in part (a) of the figure, which presents the surface pressures. A comparison of the calculated results and experimen-

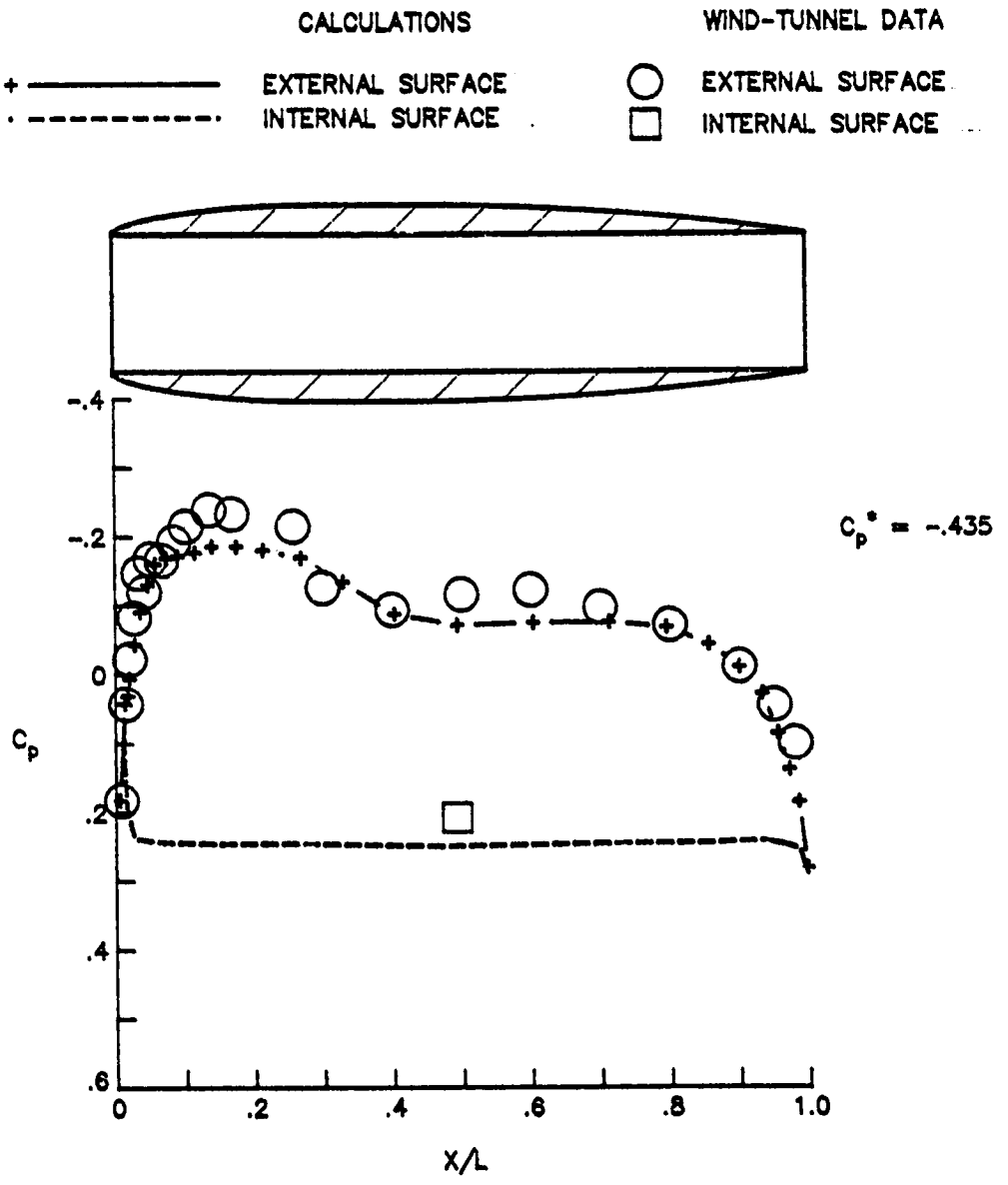

(a) Surface pressure coefficients.

Figure 4. Basic solution calculated with the implicit computational procedure. ($M_\infty = 0.80$, $\alpha = 0.0^0$.)

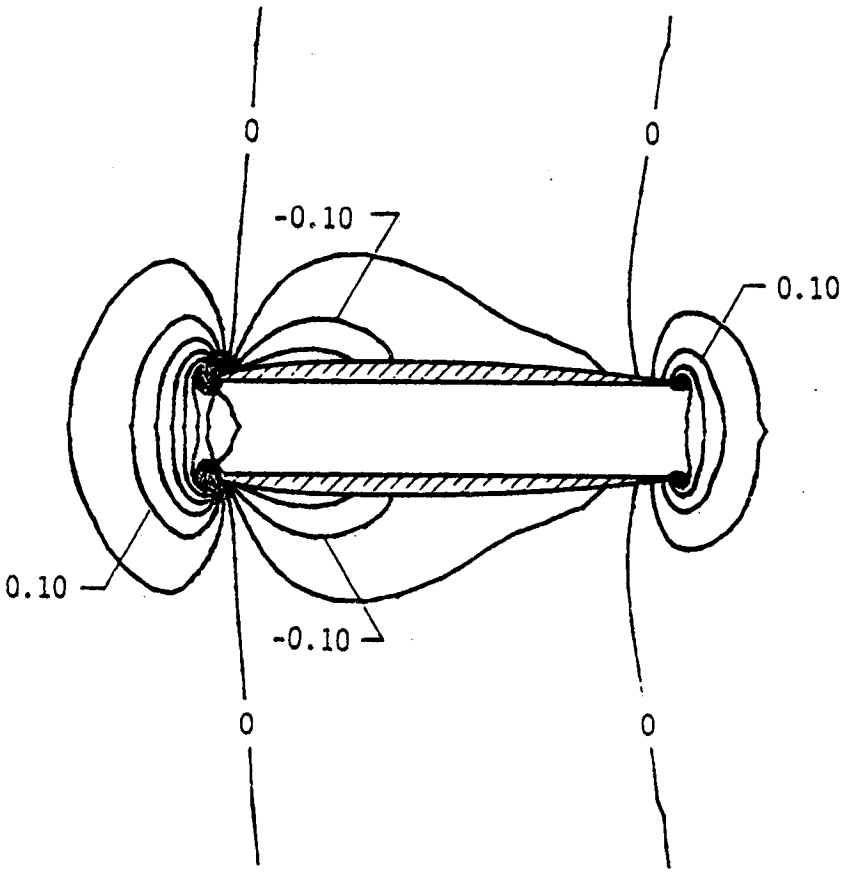

(b) Pressure coefficient contours.

Figure 4. Concluded.

tal data shows that the comuptational technique predicts the general features of the flow and the magnitude of the pressures.

Specifically, the calculations predict the correct axial location of the leading edge suction pressure peak; however, they underpredict its magnitude by about 20 precent. The compression and reexpansion over the middle portion of the nacelle is also predicted by the calculations. The large local gradient and reexpansion is the result of discontinuities in the curvature of the external nacelle surface. Although the slope of the nacelle surface is continuous, the juncture of the cylindrical section with the inlet and afterbody sections has a discontinuous curvature. Similar to the leading edge pressure peak, the predicted compression and reexpansion are in the correct axial location but the compression is somewhat smeared by the calculations. The tendency of the computational technique to smear the gradients is at least partly due to the sparseness of the grid over the middle portion of the nacelle coupled with the inclusion of numerical damping in the solution technique. For example, over the region where the compression occurs, there are only 5 or 6 axial grid stations which appear to be an insufficient number to resolve the gradient. The sparseness of the grid may also lead to excessive numerical dissipation in this region.

Part (b) of figure 4 presents computed pressure coefficient contours in the vertical plane for the nacelle at 0^{o} angle of attack. The contours illustrate that even though the computational technique is three dimensional, the solution at 0^{o} angle of attack exhibits the proper axisymmetric behavior.

Effect of grid refinement. A solution was obtained with twice as many grid points in the axial direction as for the calculations presented in figure 4. The fine grid resulted in the maximum number of grid points possible for the implicit technique before the incore storage capacity of the Cyber 203 was exceeded. The solution with this grid, which is presented in figure 5, shows a considerable improvement in the agreement between the computations and experiment on the external surface. It has a more negative leading edge suction pressure peak, and the compression in the mid-nacelle region is stronger and has a steeper gradient. In addition, the computed reexpansion region on the nacelle is in quite good agreement with the wind-tunnel data.

Nacelle at angle of attack. A solution for the flow around the nacelle was also obtained at a free-stream Mach number of 0.80 and an angle of attack of 4.0°. Figure 6 presents a comparison of the calculated pressures with the experimental data of Re and Peddrew for the side meridian of the nacelle, $\phi = 90^{\circ}$. The computational technique predicts the qualitative and quantitative character of the flow well, and the general comments about the comparison of the calculations with experimental data at 0° angle of attack apply. For this calculation, however, it was necessary to average the internal and external flow quantities at the leading edge in order to obtain a solution.

The computed pressure distributions for the top, side, and bottom rows of the nacelle are presented in figure 7. The external distributions, presented in figure 7(a), demonstrate the three-dimensional character of the flow with the nacelle at angle of attack. The majority of the three-dimensional effect is confined to the forward portion of the

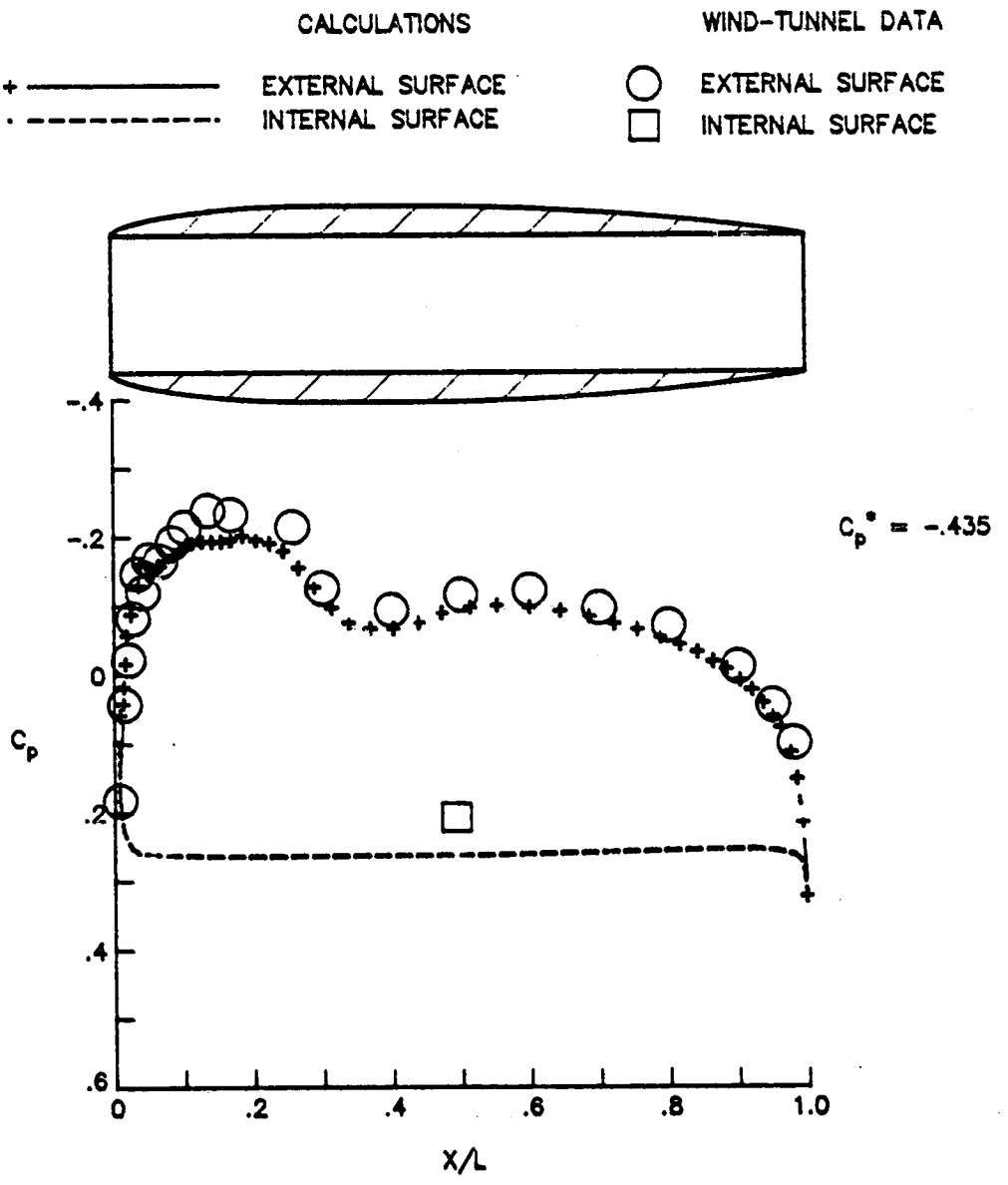

Figure 5. Fine grid solutions calculated with the implicit computational procedure. ($M_\infty = 0.80$, $\alpha = 0.0^o$.)

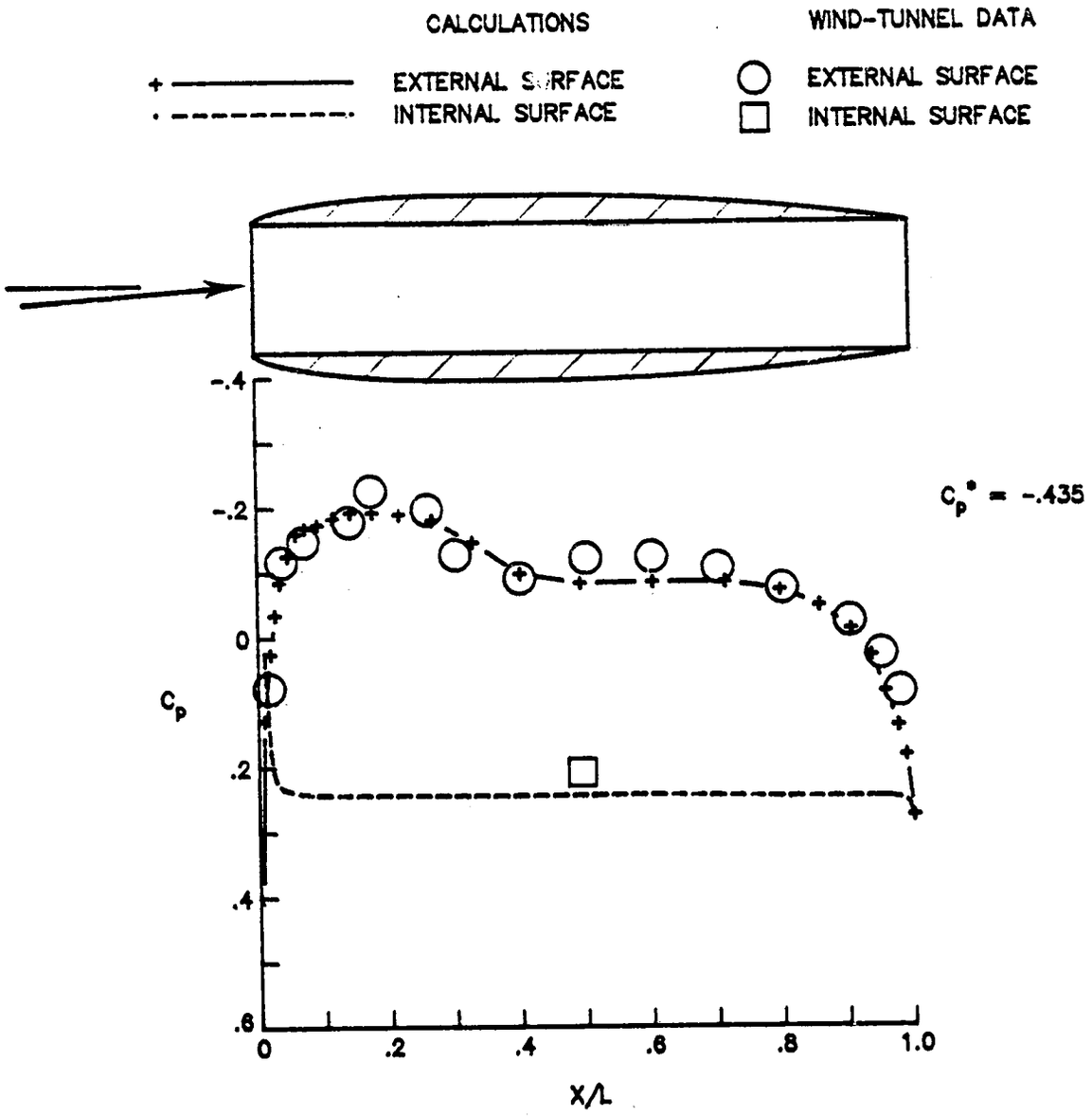

Figure 6. Computed and experimental surface pressure coefficient distributions at angle of attack. ($M_\infty = 0.80$, $\alpha = 4.0^0$, side row, implicit code.)

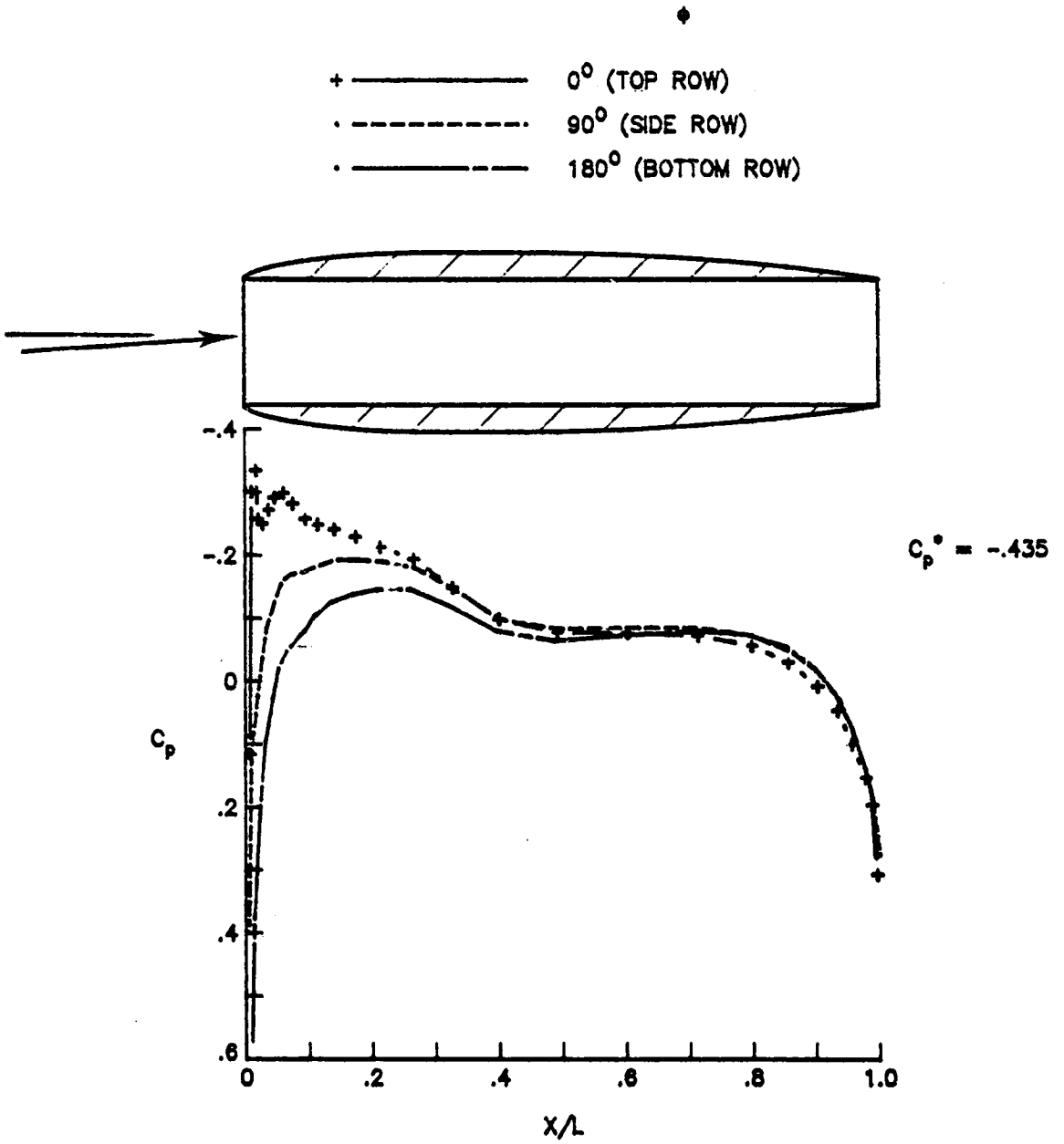

(a) Outside surface.

Figure 7. Computed surface pressure coefficient distributions for several rows at angle of attack. ($M_\infty = 0.80$, $\alpha = 4.0^\circ$, implicit code.)

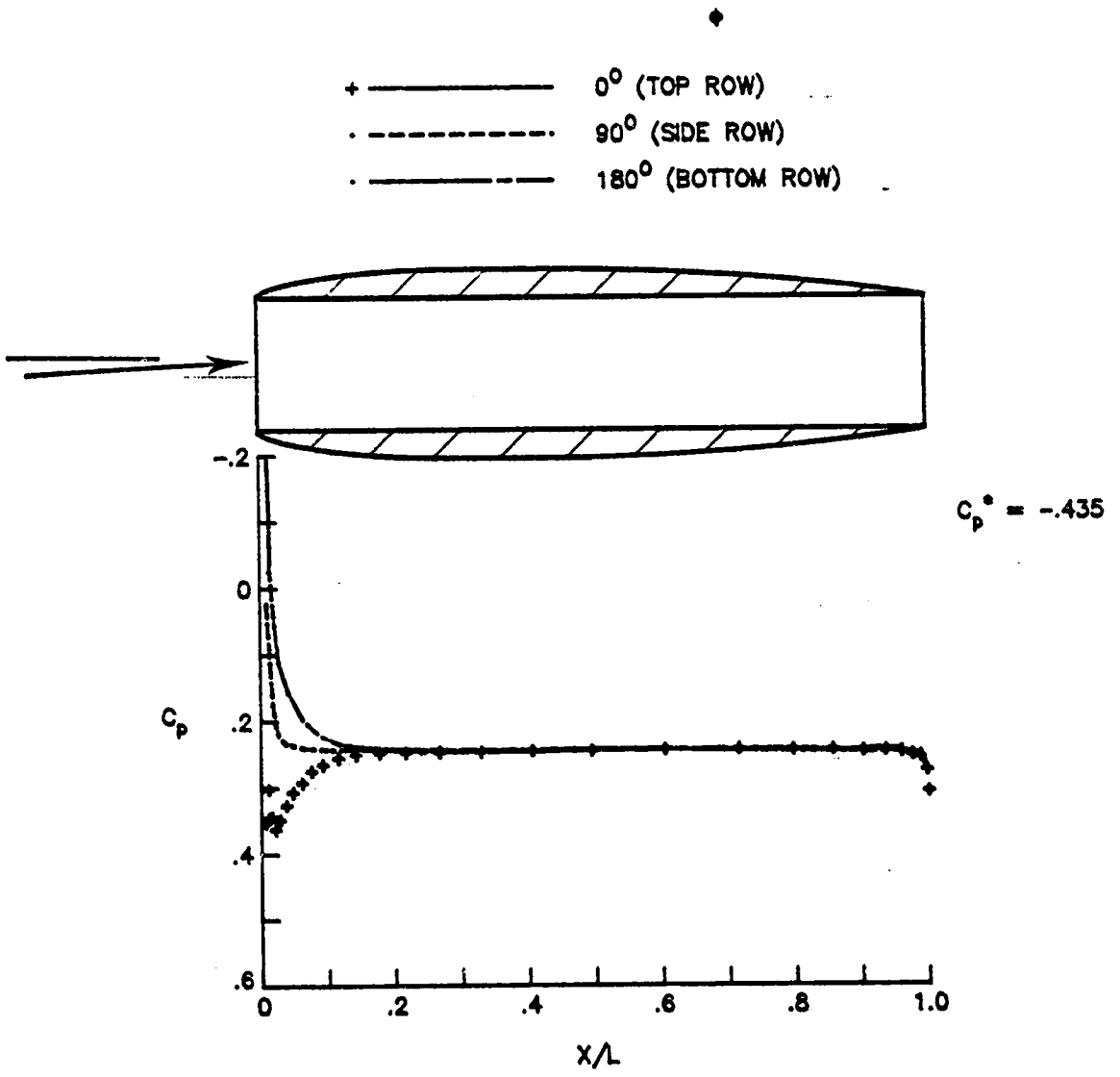

(b) Inside surface.

Figure 7. Concluded.

nacelle where the calculations show that a large suction peak is being generated at the leading edge of the top meridian. The internal pressure coefficients, presented in figure 7(b), are influenced by the three-dimensionality of the flow only in a relatively small region at the nacelle leading edge.

Contours of the computed pressure coefficients in the vertical plane with the nacelle at an angle of attack of 4.0^{o} are presented in figure 8. The contours also illustrate the three-dimensionality of the computed flowfield with the nacelle at angle of attack. A comparison of these contours with those at 0.0^{o} angle of attack, presented in figure 4(b), illustrates the more pronounced pressure gradient on the inside of the nacelle at $\alpha = 0.0^{o}$, and the differences between the pressure gradients on the inner and outer surfaces near the leading edge. It also illustrates the greater expansion of the external flow on the top of the nacelle at the higher angle of attack.

Explicit Computational Results

Solutions for the flow past the flow-through nacelle were also computed using the explicit Runge-Kutta computational procedure with implicit smoothing of the residuals described in Chapter IV. The results obtained with the explicit procedure are presented in figures 9 through 12.

Basic solution. The basic solution at a Mach number of 0.80 and an angle of attack of 0^{o} is presented in figure 9. Like the implicit computational technique, the explicit technique predicts all of the general features of the flow, and the pressures on the external surface agree quite well with the wind-tunnel data (see part (a) of the figure).

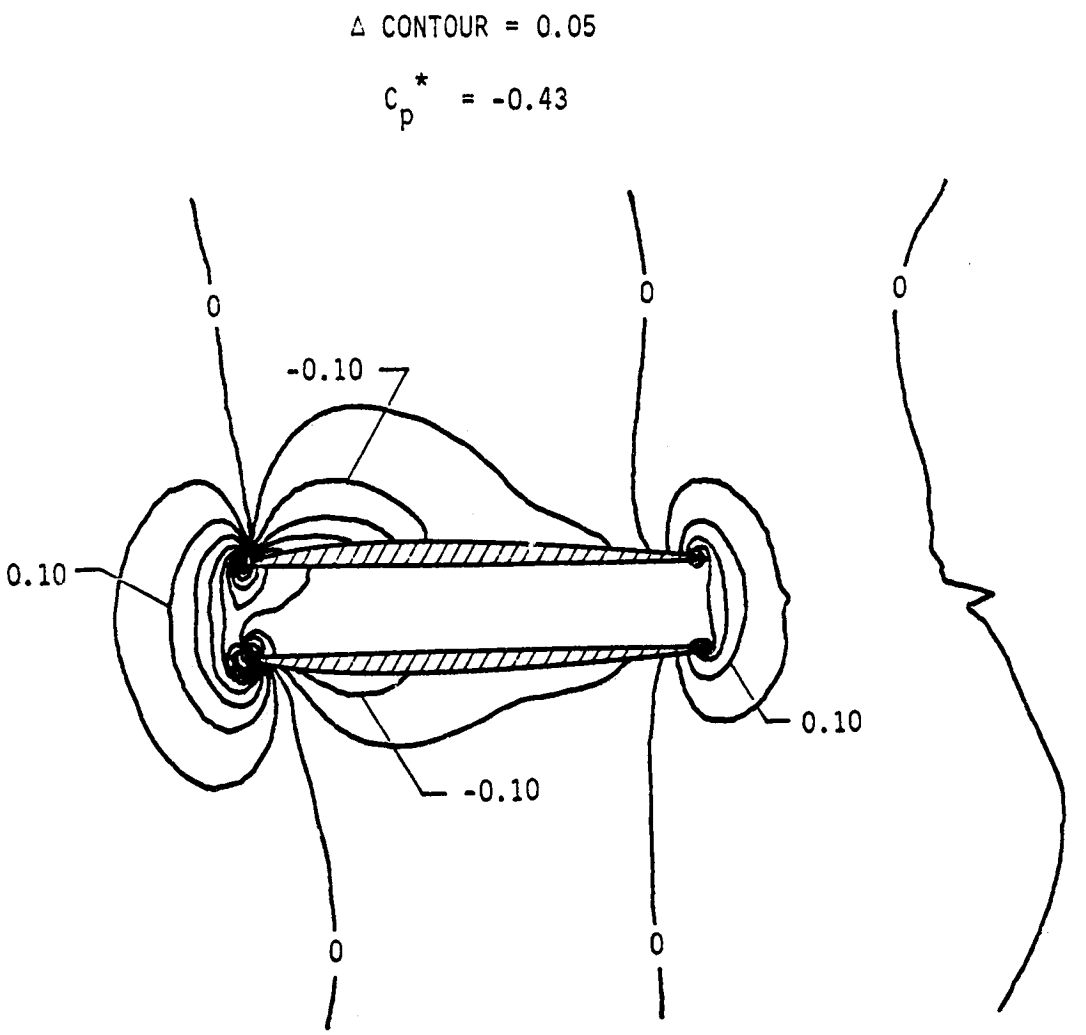

Figure 8. Pressure coefficient contours for the computations at angle of attack. (M_∞ = 0.80, α = 4.0°, vertical plane, implicit code.)

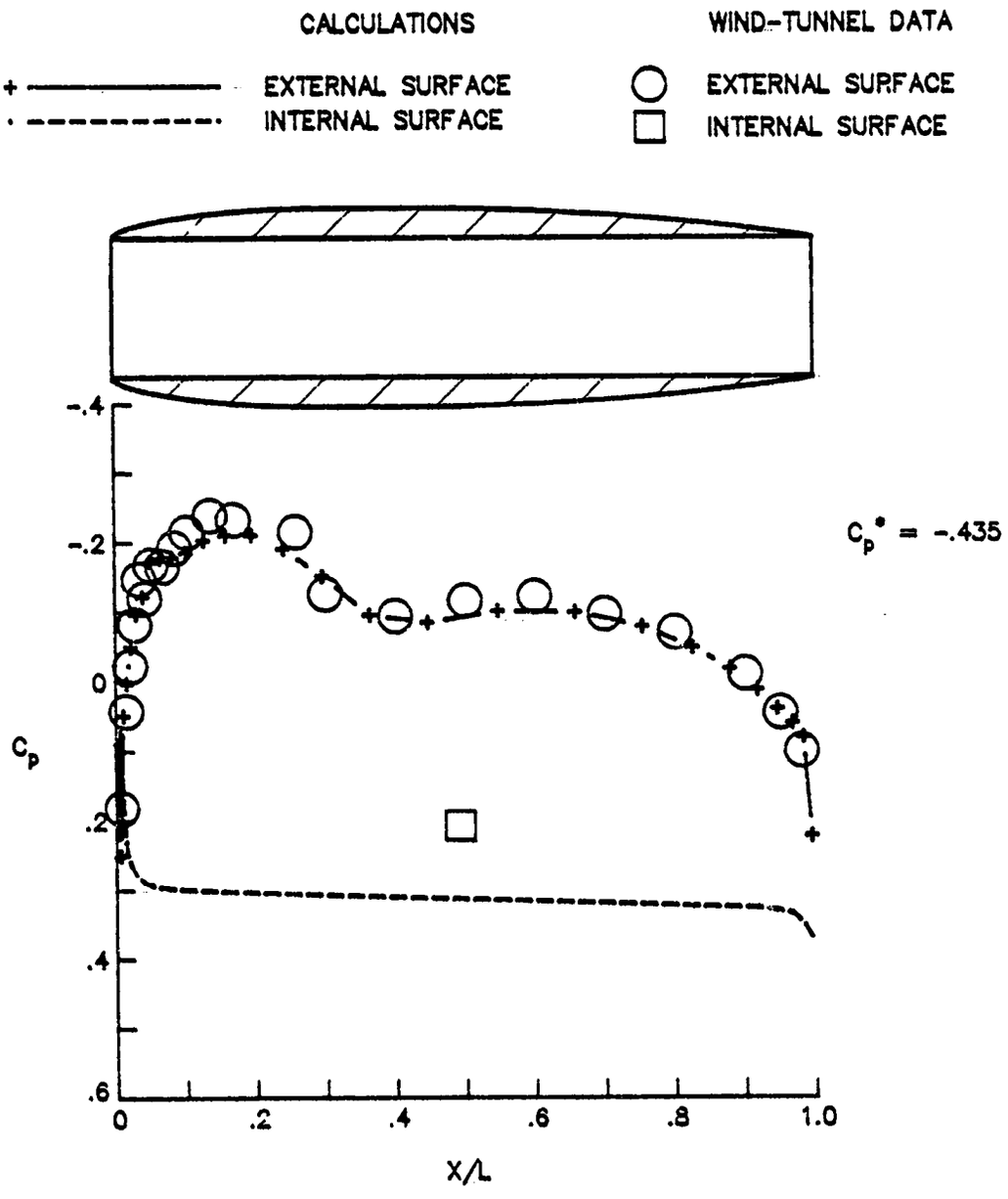

(a) Pressure distributions.

Figure 9. Basic solution computed with the explicit computational procedure. ($M_\infty = 0.80$, $\alpha = 0.0^o$.)

Δ CONTOUR = 0.05

C_p^* = -0.43

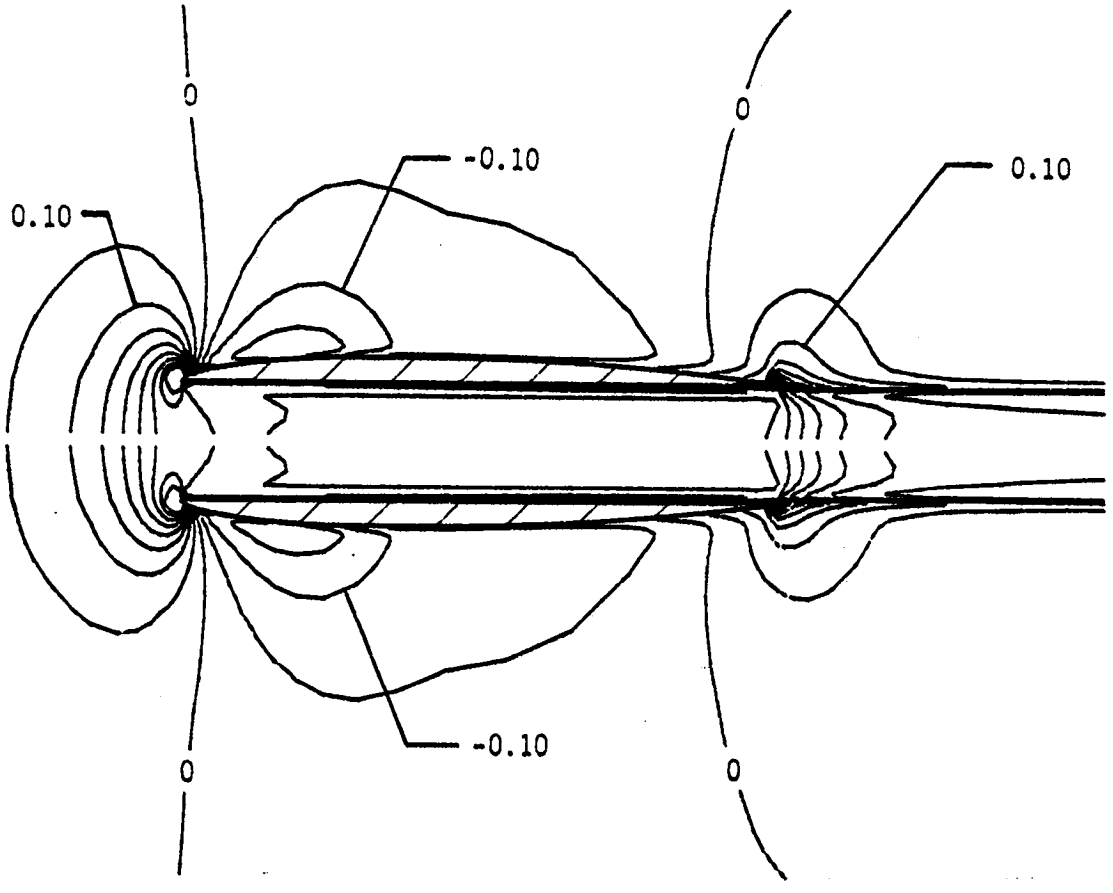

(b) Pressure coefficient contours.

Figure 9. Concluded.

By comparing these pressure distributions with the ones calculated by using the implicit procedure, figures 4(a) and 5, one can see that the explicit procedure gives a more accurate solution on the external surface for the same number of grid points. This is particularly evident in the region of the rapid compression and reexpansion which occurs on this surface. Here the explicit procedure captures the gradients much better than the implicit procedure and comes close to matching the resolution of the pressure distribution computed by using the implicit procedure with twice as many grid points. The computed pressures on the internal surface are much more positive than the data.

Pressure coefficient contours for the explicit solution are presented in part (b) of figure 9. The region of low pressures which is affected by the nacelle is slightly larger for the explicit calculations than for the implicit calculations (see figure 4). The differences in both the external surface pressures and the pressure coefficient contours between the two solutions may be the result of the slightly different implementation of the surface boundary condition.

Grid refinement study. An attempt was made to look at the effect of grid resolution for the explicit computational technique. It was possible to add 10 grid stations axially along the surface of the nacelle, for a total of 40 grid stations along the surface, before the incore storage capacity of the Cyber 203 was exceeded. Figure 10 presents the solution for this finer mesh at a free stream Mach number of 0.80 and an angle of attack of 0.0^{o}. By comparing the computed pressures, which are presented in figure 10(a), with the pressures for the coarser mesh, one can detect a slight improvement in the agreement with the wind-tunnel data as the mesh

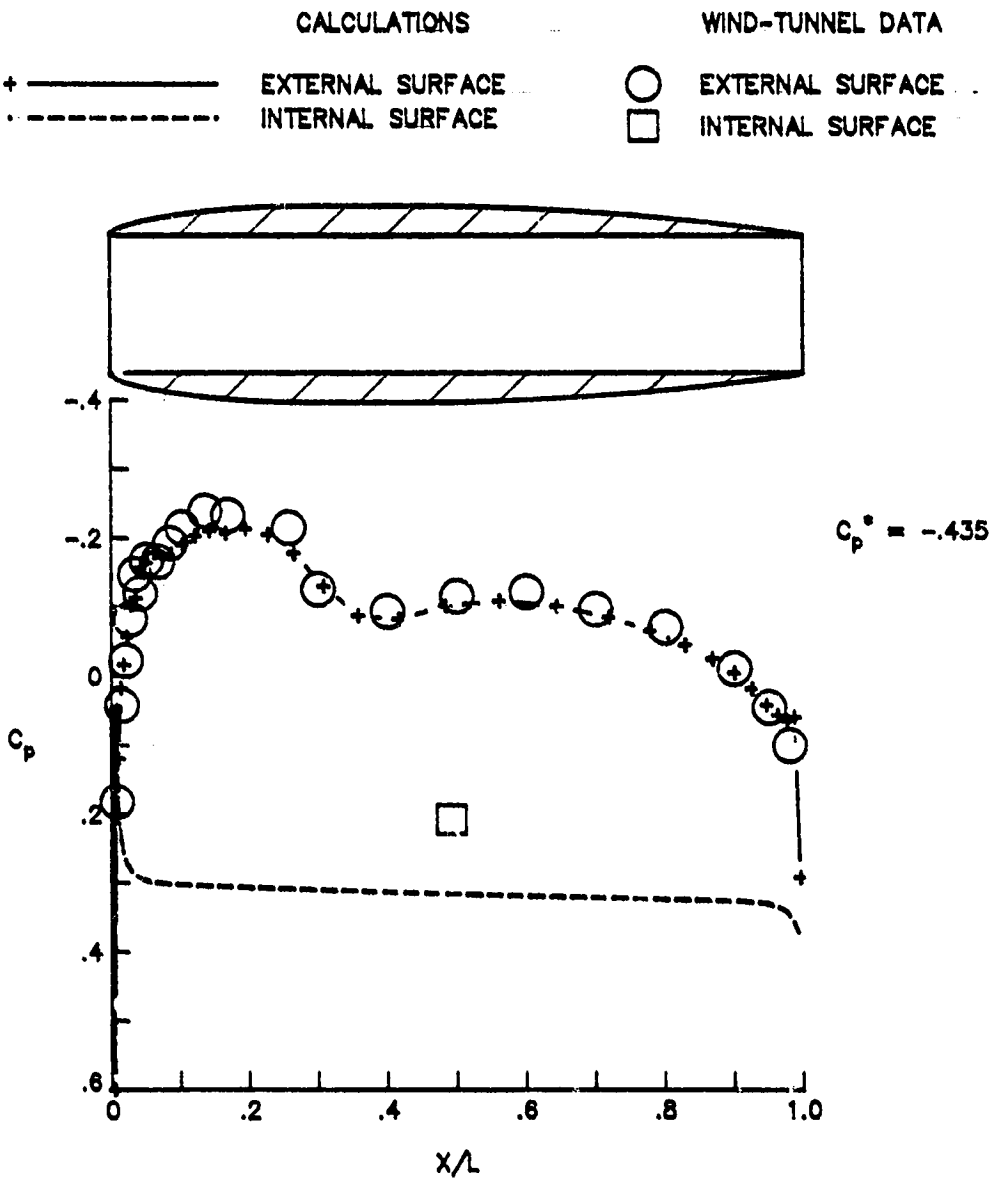

(a) Pressure distributions.

Figure 10. Solution for the finer grid and the explicit computational procedure. ($M_\infty = 0.80$, $\alpha = 0.0^0$.)

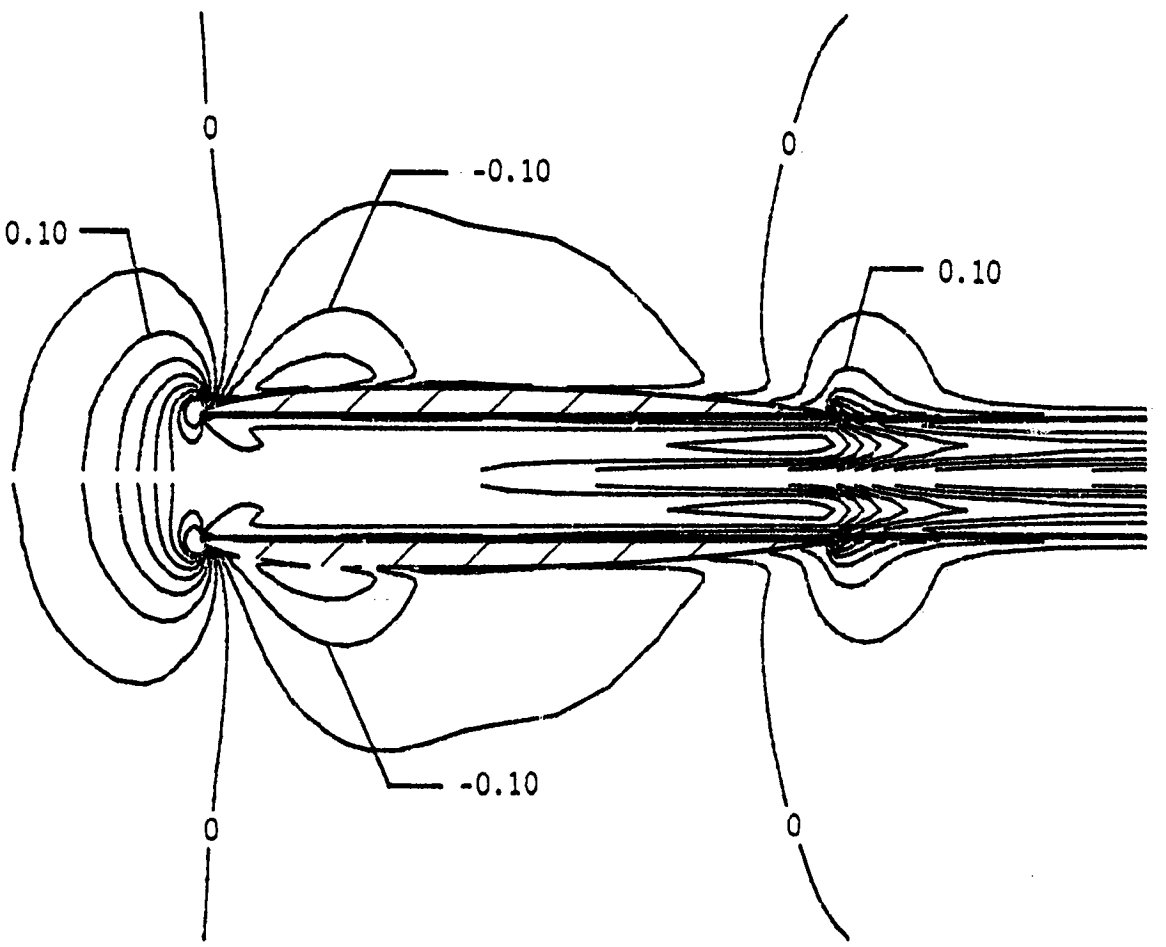

(b) Pressure coefficient contours.

Figure 10. Concluded.

is refined. The pressure coefficient contours for the refined grid case are presented in part (b) of figure 10. The contours are essentially the same as those for the coarser grid.

The modest increase in the number of grid points resulted in a slight improvement in the correlation between the explicit solution and the wind-tunnel data. Even though the overall level of the correlation is very good, a greater increase in the number of grid points may further improve the agreement in the region of the peak expansion and the following compression.

Internal pressure level. The addition of more grid points along the surface did little to improve the correlation between the computations and the wind-tunnel data on the internal surface. The results of the implicit technique agree much better with experiment inside the nacelle, and hence seem to be more accurate. However, the implicit technique has a Kutta-like condition imposed at the trailing edge. A calculation with a version of the implicit code which did not contain the "Kutta" condition shows the same basic trends as the explicit code as can be seen from figure 11. In a similar observation, Miranda[36] indicates that inviscid potential solutions for similar configurations frequently give good solutions for the external flow but yield the incorrect internal mass flow ratio. These results lead one to speculate that the Euler "non-Kutta" solutions possess the correct internal trends for inviscid flow. Chapter VII examines in detail the possibility that the discrepancy between the data and the calculations is due to viscous dissipation present in the experiment.

Supercritical solution. In addition to the solution at a Mach number of 0.80 and an angle of attack of 0^{o}, a solution with the explicit

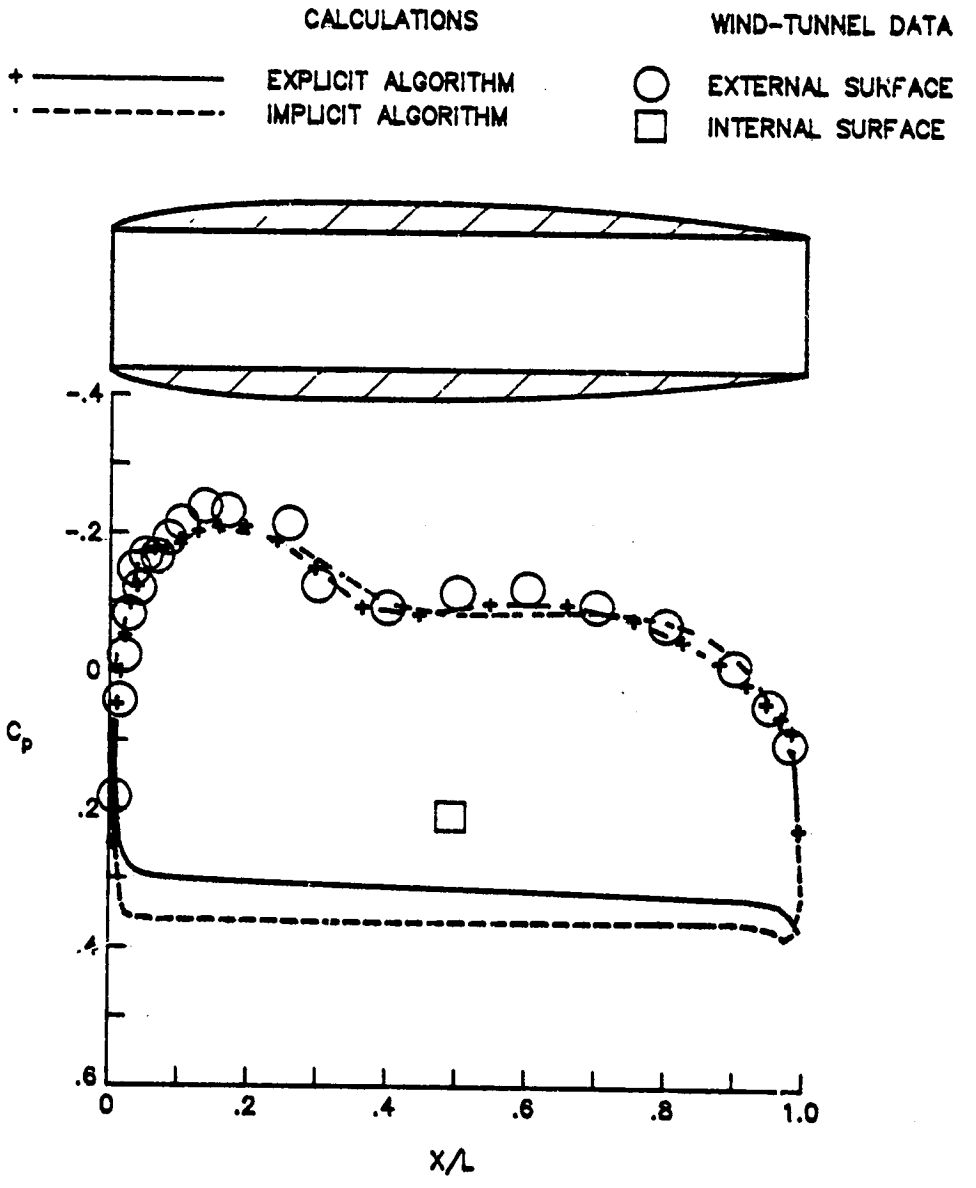

Figure 11. Comparison of experimental and calculated pressures for the inviscid Euler equations. ($M_\infty = 0.80$, $\alpha = 0^o$.)

procedure was obtained at a Mach number of 0.94 and 0^0 angle of attack. The experimental data indicated that 0.94 was the highest Mach number for which the flow on the nacelle was not separated. The calculation was made with the finer computational mesh described in the earlier section on grid resolution.

The computational results agree very well with the measured pressures on the external surface of the nacelle as figure 12(a) illustrates. On the internal surface, just as they did at the Mach number of 0.80, the calculations predict higher pressures than the wind-tunnel data. Even though the predicted peak expansion near the leading edge is low, the pressures agree with the data everywhere except at the very peak. Probably grid resolution or excessive dissipation due to the large changes in the pressures in this region of the flow is responsible for the discrepency. The calculations both qualitatively and quantatively predict the rearward movement of the leading edge negative pressure peak with increasing Mach number. Notice that the general shape of the leading edge expansion and subsequent recompression has changed from the lower Mach number. At the higher Mach number, the expansion continues until it is abruptly terminated by a strong compression, or possibly a shock. The calculations correctly reflect this shape change. Also, at the higher Mach number, the more pronounced hump in the pressures on the rear of the nacelle is predicted and the calculations match the data very well in this region.

Parts (b) and (c) of figure 12 present pressure contours in the vertical plane for the calculation. Part (b) of the figure shows the overall region in the vicinity of the nacelle, and part (c) presents a detailed view of the leading edge region. The pressure contour

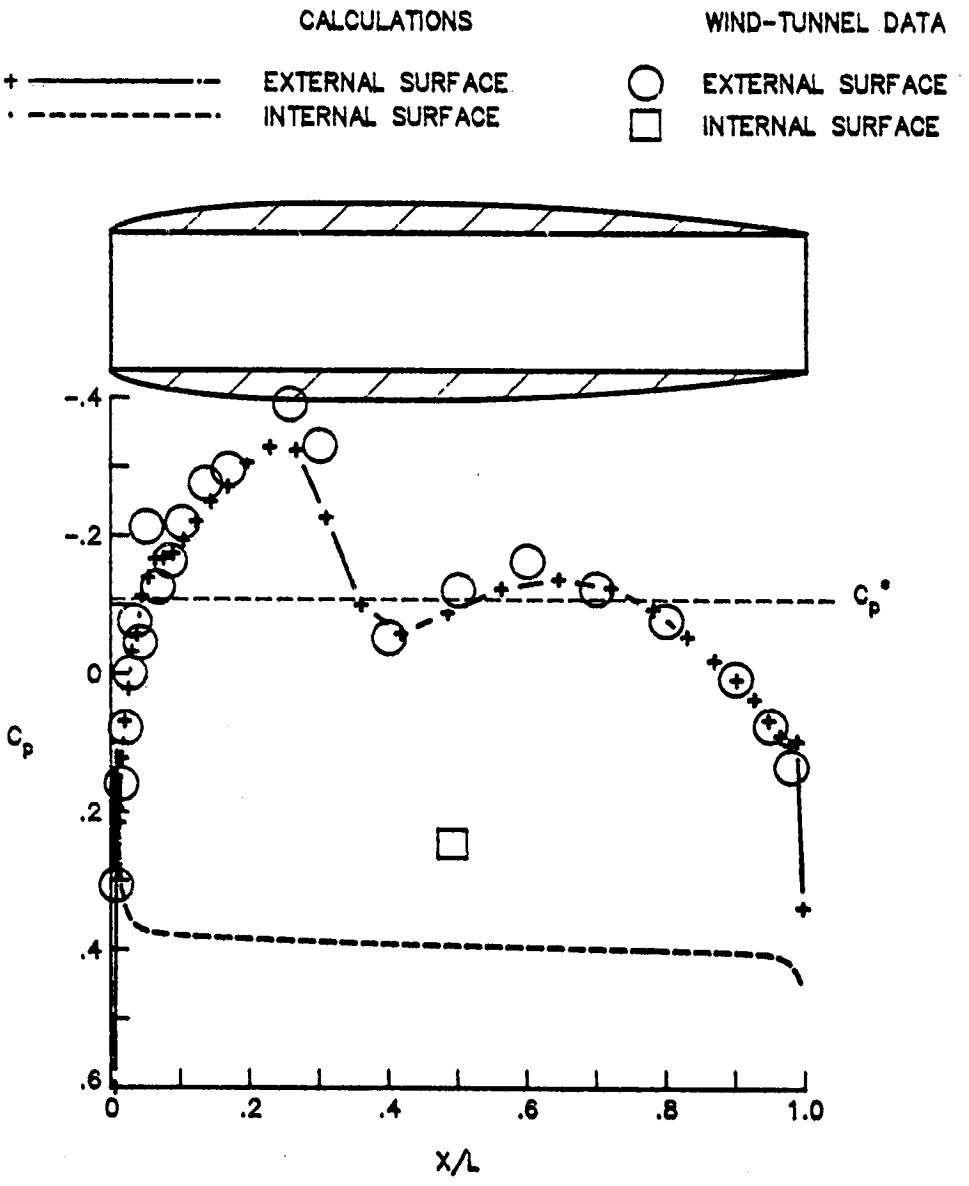

(a) Pressure distributions.

Figure 12. Supercritical solution calculated with the explicit computational procedure. ($M_\infty = 0.94$, $\alpha = 0.0^o$.)

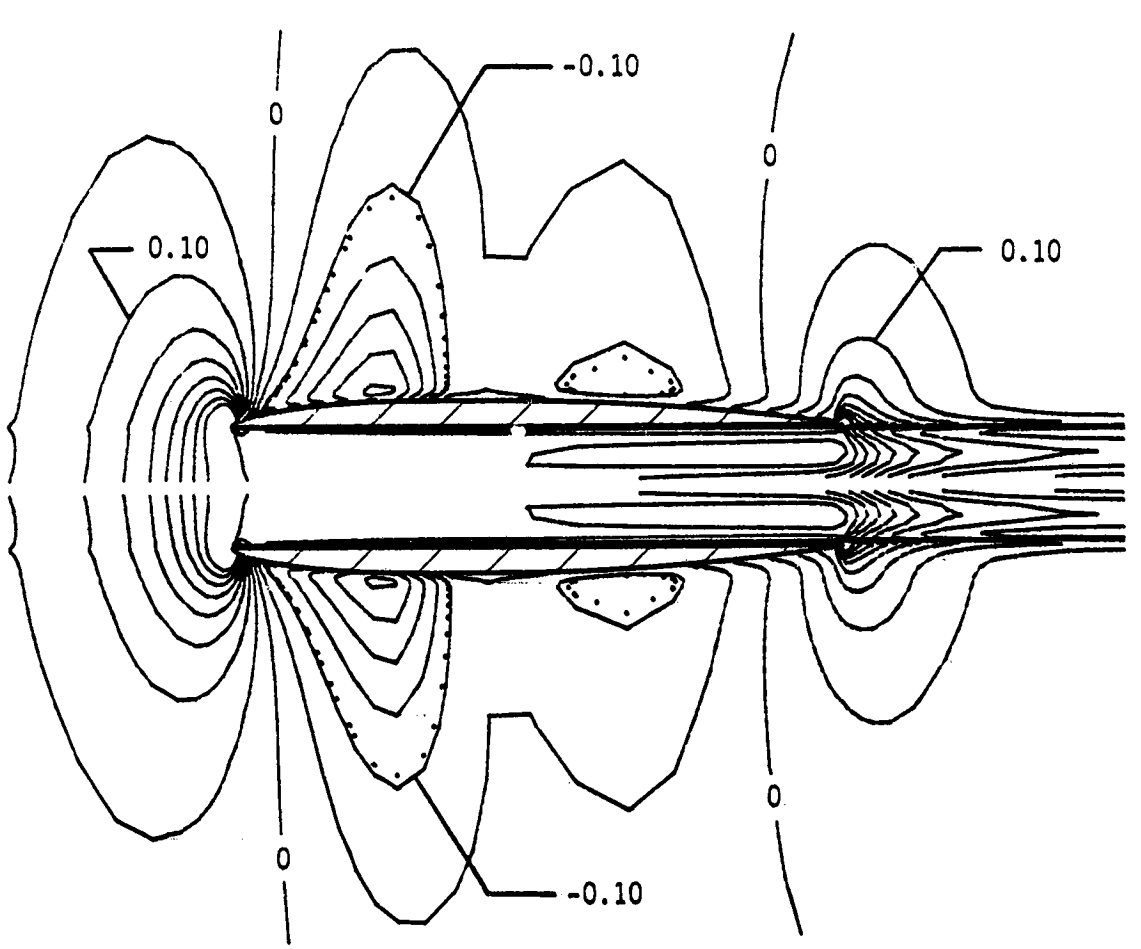

(b) Pressure coefficient contours.

Figure 12. Continued.

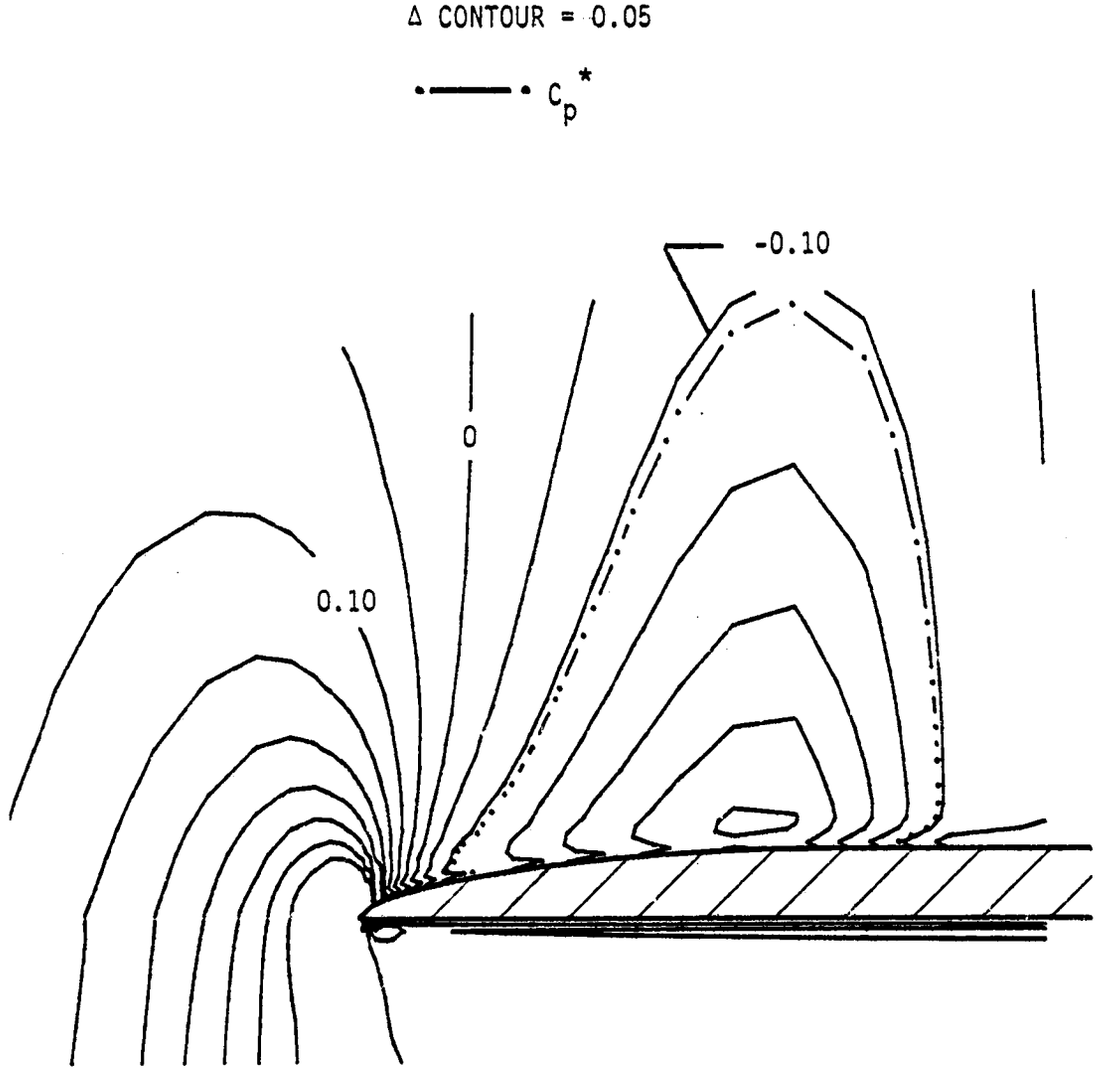

(c) Pressure coefficient contours in the vicinity of the leading edge region.

Figure 12. Concluded.

corresponding to a local Mach number of 1.0 is represented by a dashed line. The contours illustrate the extent of the supersonic bubble on the forward part of the nacelle, and also show that there is a small supersonic bubble on the afterbody. In addition, they illustrate that the zone influenced by the nacelle, both the compression zones originating at the leading and trailing edges and the expansion zones, extend further outward in the radial direction. One might expect this general change in the nature of the flow at the supercritical Mach number.

The calculations have correctly predicted the changing nature of the flow from the lower to the higher transonic Mach number, and also predicted the quantitive results at the two Mach numbers very well. Combined with the good predictions at angle of attack, these results demonstrate the potential of the Euler equations in solving flows of this complexity.

Numerical Problem Areas

During the development of the implicit computational procedure, and the subsequent numerical studies using both the implicit and explicit procedures, two unexpected numerical difficulties were discovered and investigated. The first difficulty concerns the stability properties of the implicit algorithm. The second pertains to a numerically produced surface total pressure loss, and is inherent in both the implicit and explicit algorithms. While other researchers may have encountered similar difficulties, until recently a large segment of the computational community was unaware of the stability problem.[37] The total pressure problem still remains largely unreported.[37] The investigation of these areas is discussed in this section.

Effect of boundary conditions on implicit convergence. In the early 1980's, when the development of the implicit computational procedure was initiated, the Beam and Warming alternating-direction-implicit numerical algorithm was relatively new and untested, particularly in three dimensions. Difficulties with its stability properties in three dimensions were then known or suspected by only a small community of researchers.[38-39] As noted in Chapter III, while the implicit phase of the present work was eing conducted, Abarbanel, Dwoyer, and Gottleib[23] proved that the undamped Beam and Warming scheme in three dimensions is weakly, but unconditionally, unstable. They also showed that the weak instability is only present in the very long wavelengths.

During the development of the implicit procedure, an instability manifested itself near the outflow boundary. The problem was investigated, and a radiation outflow boundary treatment was applied which enabled reasonably accurate engineering solutions to be obtained. These results which are reported by Compton and Whitesides in reference 14 tend to confirm the work of Abarbanel, Dwoyer, and Gottleib.[23] The results of reference 14 have helped clarify the weak instability in the undamped Beam and Warming algorithm when applied to the three dimensional Euler equations. This aspect of the development of the implicit computational procedure is described below.

Two parameters, $\Delta C_{p,max}$ and the maximum residual, were used to test the convergence of the numerical solutions obtained with the implicit numerical technique. At any given time level, ΔCp is defined to be the absolute change in the pressure coefficient between the present time level and the previous time level. The total residual at any time step is

defined to be the root mean square of the rate of change of all five of the normalized dependent variables. At every time step, ΔCp and the total residual are computed at each grid point and the entire computational region is searched for the maximum value of each parameter.

Figure 13 presents the iteration history for the solution obtained with the outflow boundary condition $p = p_\infty$ and extrapolation at the far-field boundary. The history of $\Delta C_{p,max}$ indicates that the solution is converging. However, the history of the maximum residual indicates that the solution is in fact diverging. Thus it is misleading to base convergence strictly on the change of a flow parameter. The increase in maximum residual coincides with its location gradually changing from the vicinity of the nacelle to the outflow boundary, implying that the outflow boundary condition $p = p_\infty$ equation (25), is partially reflective.

The nonreflecting outflow boundary condition of Rudy[25] was tried with mixed results in stabilizing the solution process. In addition, the Riemann-invariant method of treating the outflow boundary,[13] which was used very successfully in combination with the explicit computational procedure, was briefly investigated. However, a satisfactory solution was not obtained with this combination.

As a consequence of these results, the radiation boundary condition, equation (32), was derived and investigated. The iteration history of the residuals when the radiation boundary condition was used at both the outflow and far-field boundaries is presented in figure 13(b). The overall maximum residual indicates that the pressure disturbances passed through the outflow boundary more easily, delaying the emergence of the instability until approximately 1000 iterations. After the instability

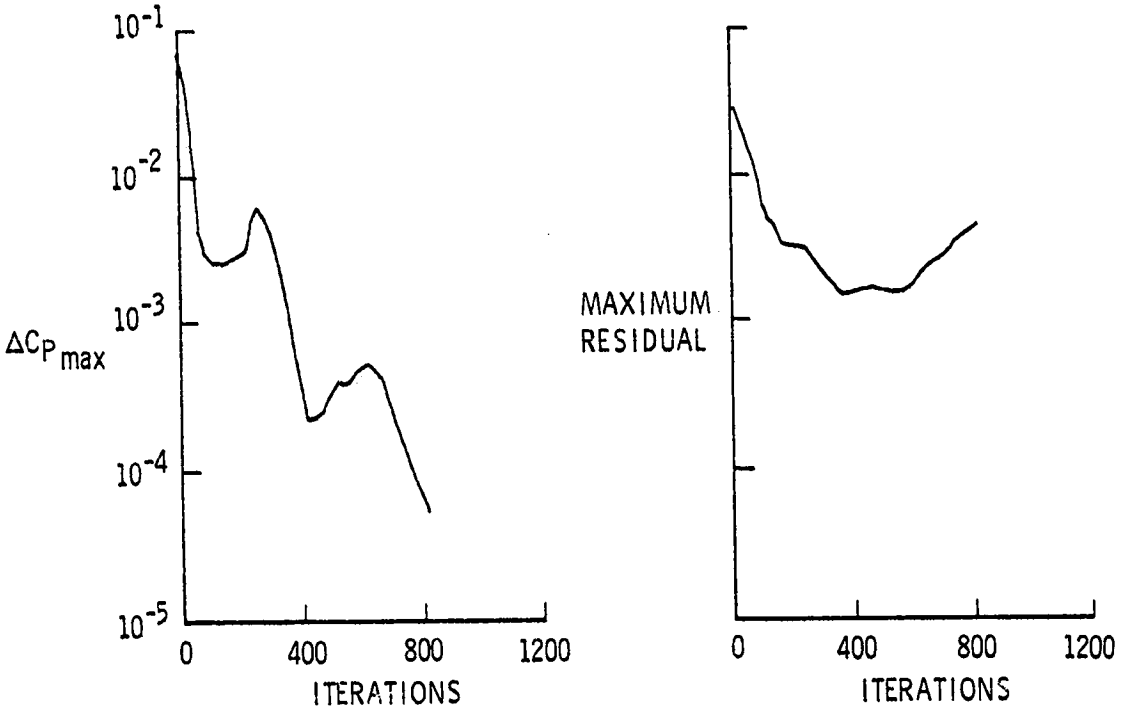

(a) Outflow boundary condition $p = p_\infty$.

Figure 13. Iteration history for the residual of the implicit computational procedure. ($M_\infty = 0.80$, $\alpha = 0.0^o$.)

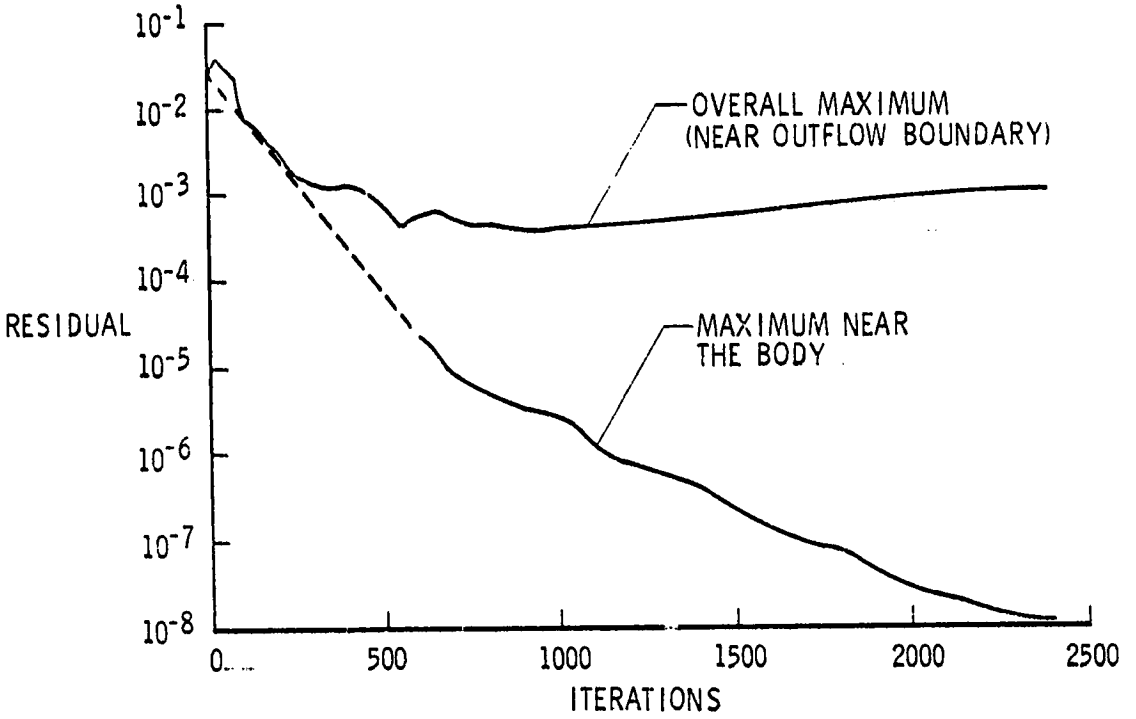

(b) Radiation outflow boundary condition.

Figure 13. Concluded.

emerges, the rate at which the overall maximum residual grows is reduced to near zero from the rapid growth associated with using equation 25.

Validity of the implicit solutions. The iteration history of the overall maximum residual presented in figure 13(b) tends to confirm the results of Abarbanel et. al. However, the boundary conditions were imposed explicitly which may degrade the convergence properties of the implicit scheme and increase the run time. The maximum residual near the nacelle is also plotted in figure 13(b). This local residual continues to decrease with a total drop of about 4 orders of magnitude in 1200 iterations, and 6 orders of magnitude in 2400 iterations, further indicating that the instability is associated with the boundary treatment.

Residual contours after 1200 iterations or time steps are presented in figure 14. These contours confirm that the maximum residuals do indeed occur near the outflow boundary and that the solution near the nacelle appears to be converging. Since the solution near the nacelle continues to converge and the local residual has decreased 4 orders of magnitude at 1200 time steps, the solutions near the nacelle should be reasonably accurate and useful for engineering calculations.

Explicit convergence properties. There does not appear to be a problem with the stability or convergence of the explicit computational procedure. The presentation of these properties of the explicit technique is placed in this sectior merely for comparison with the implicit algorithm. The residual upon which convergence is based for the explicit computational procedure is the difference between the computed enthalpy at any particular grid point and the free stream enthalpy. Figure 15 presents the iteration history of the maximum residual in the

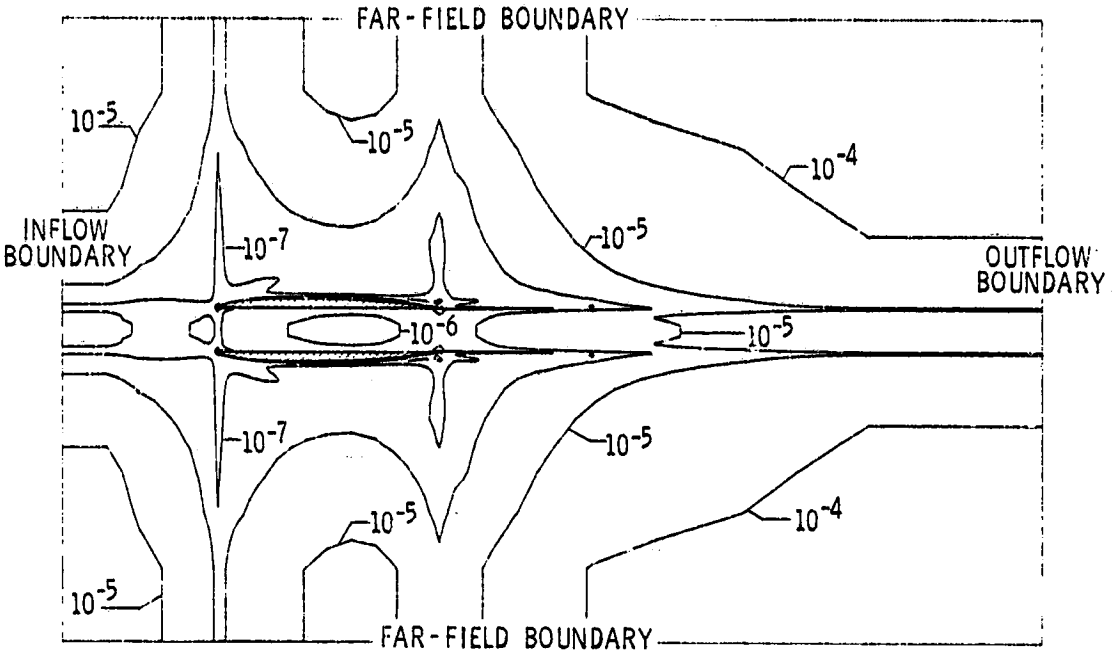

Figure 14. Residual contours for the implicit computations.
(M_∞ = 0.80, α = 0.0°, 1200 iterations, vertical plane.)

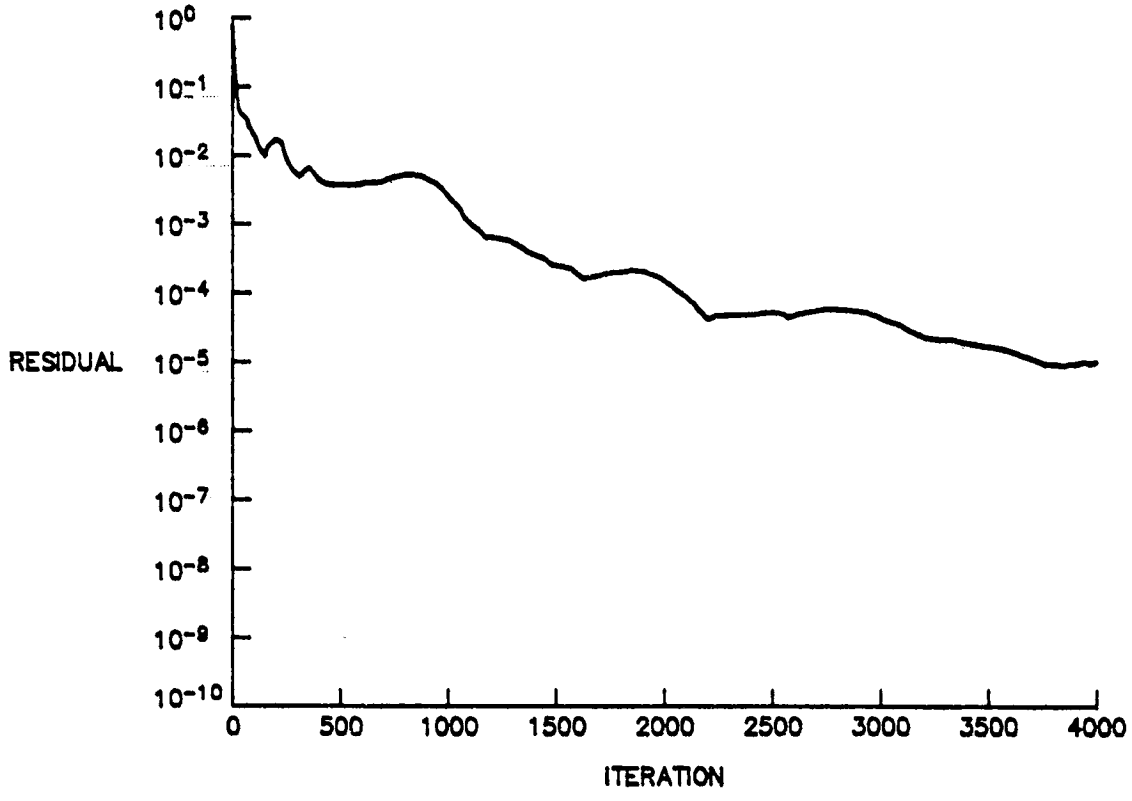

Figure 15. Iteration history for the residual of the explicit computational procedure. ($M_\infty = 0.80$, $\alpha = 0.0^{o}$.)

computational region for the basic solution. The history shows that the solution is stable and converging. The maximum residual initially drops rapidly, and although its rate of decrease levels off some, its general trend still continues down after 4000 time steps.

The solutions were obtained at a Courant number of 4 which was the largest Courant number for which numerical stability could be maintained. The optimum rate of convergence may be better than indicated by figure 15. However, no studies were made to determine the size of the damping parameters for the maximum rate of convergence. Numerical studies by Vatsa[40] indicate that the optimum values of the damping parameters for a maximum convergence rate depends upon the grid.

Total pressure loss at the surface. Calculations with both computer codes show a surface total pressure loss even at subsonic Mach numbers. This feature of the solutions, which is inconsistent with the physics of the inviscid flow, was first noticed in calculations made with the implicit computer code, and was reported in reference 14. However, an indepth investigation of the problem was not undertaken at the time. When solutions obtained with the explicit code also exhibited this characteristic, it was considered highly desirable to investigate it more fully. The resulting investigation of the problem is discussed in this section.

Since there are no supersonic regions, and hence no shocks in the present solutions for $M_\infty = 0.80$, and since the flow is inviscid, the total pressure in the entire flow field should be constant. However, the numerical calculations at this subsonic Mach number result in total pressure losses which are most noticeable on the internal surface of the

nacelle. Although the losses are confined to a small region in the immediate vicinity of the nacelle, they are sometimes quite large. The total pressure losses do not seem to affect the values of the static pressures, but as stated before, they are inconsistent with the correct physical nature of the problem.

Figure 16 presents the total pressure distributions on the nacelle surface, and illustrates the magnitude of the total pressure losses for the free stream Mach number of 0.80. The figure is typical for both the sparse and fine grids since refining the grid had little effect on the losses. Parts (a) and (b) of figure 16 present the surface total pressures calculated by using the implicit numerical procedure. The results presented in figure 16(a) were obtained with an early version of the code in which the flow variables for the top and bottom surface were averaged at the leading edge. While the total pressure on the external surface of the nacelle is essentially correct, the figure shows a loss in total pressure of approximately 5.0 percent on the internal surface of the nacelle. Initially, the loss was attributed to incorrect treatment of the the leading edge boundary (the implicit computational technique required a direct treatment of the leading and trailing edge boundaries). As a consequence, a wide variety of leading edge treatments was investigated in order to correct the problem.

The outcome of the leading edge study was to adopt the present treatment described in Chapter III in which the two surfaces were treated separately. Figure 16(b) shows the total pressure distributions resulting from the calculations using the new leading edge boundary condition. The loss is now split between the upper and lower surfaces, with a loss of about 2.5 percent on each surface. Considering the following results

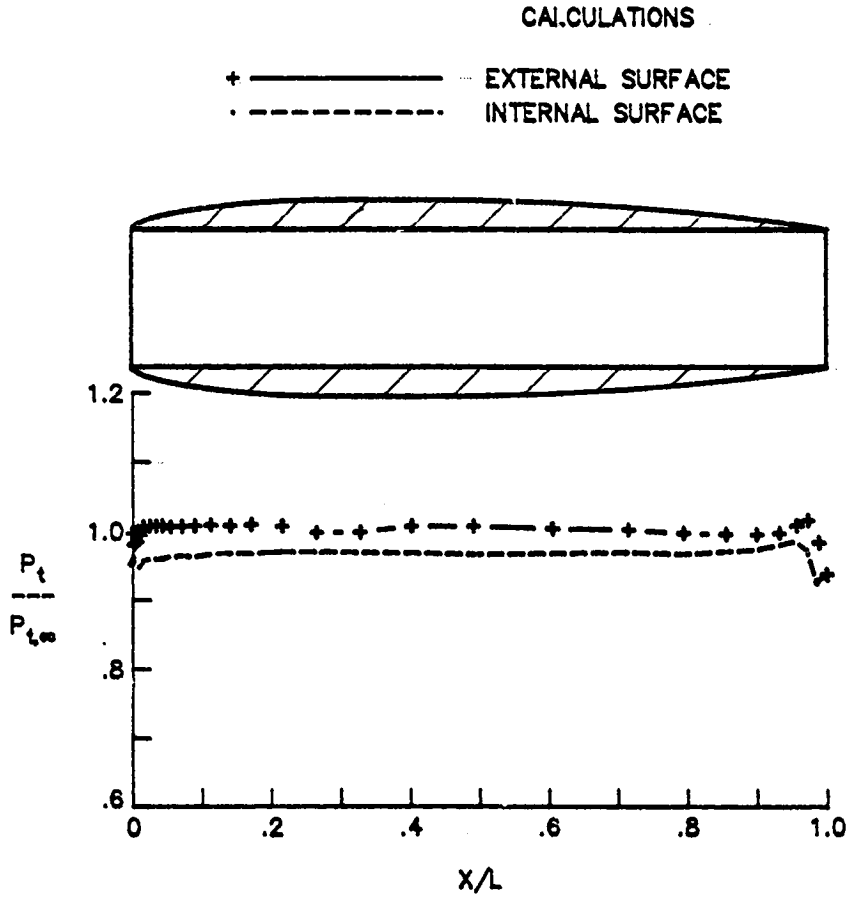

(a) Implicit computational procedure, dependent variables averaged at the leading edge.

Figure 16. Surface total pressure distributions.

(M_∞ = 0.80, α = 0.0°.)

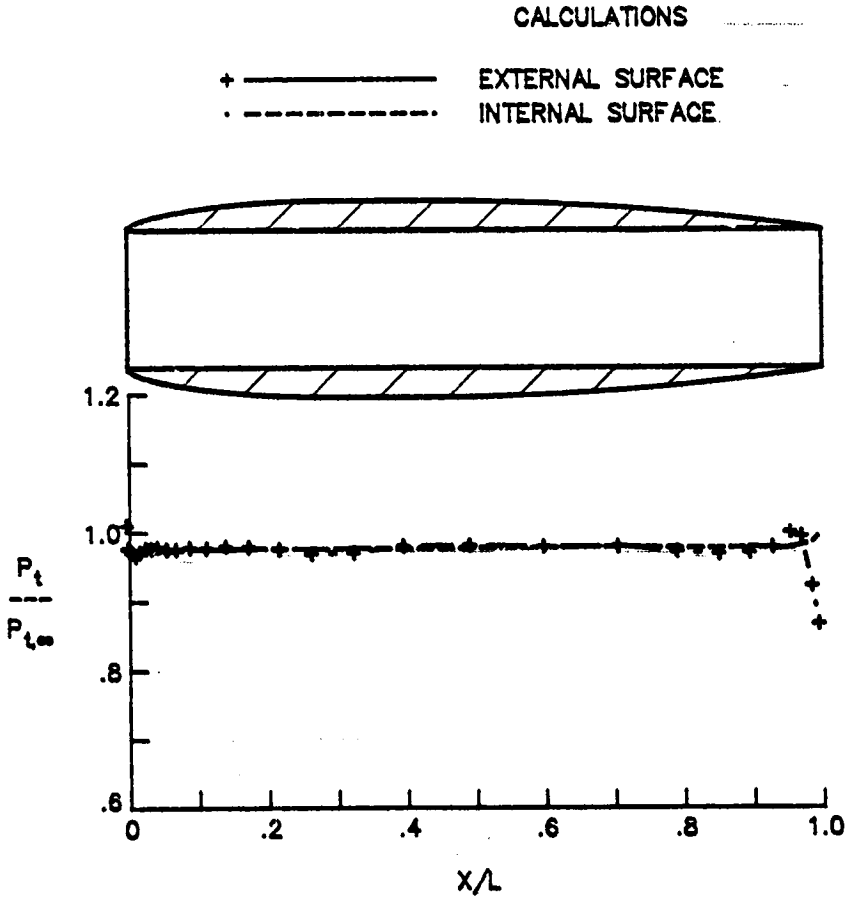

(b) Implicit computational procedure, dependent variables not averaged at the leading edge.

Figure 16. Continued.

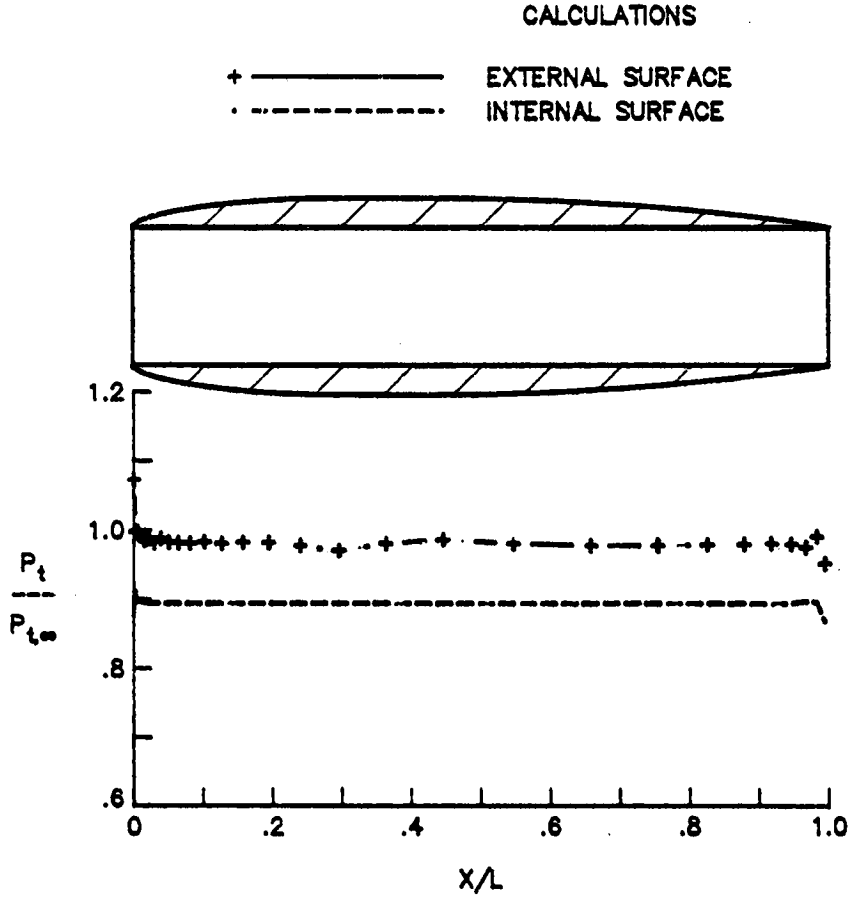

(c) Explicit computational procedure.

Figure 16. Concluded.

obtained with the explicit computational procedure, it is doubtful that the new boundary treatment results in a more physically correct solution.

Since the explicit computational procedure incorporates a finite volume differencing technique, and therefore does not require any direct treatment of the leading or trailing edge boundaries, it was not expected to give total pressure losses at a subsonic Mach number. However, as part (c) of figure 16 shows, the problem is magnified by the explicit technique. Like the results for the implicit technique with the earlier leading edge boundary treatment, the total pressure on the external surface is essentially correct. The losses on the internal surface, however, have increased to approximately 10 percent. These results indicate that the source of the loss is not associated with the treatment of the leading and trailing edge boundary conditions.

Origin of the total pressue loss. In order to help determine the source of the losses, additional numerical experiments were conducted with the explicit computational procedure using an unswept, untapered wing as the test configuration. Using the unswept, untapered wing resulted in a physical problem with two-dimensional flow, but retained the three-dimensionality of the computational procedure. The results of the experiments, which are presented in the appendix, indicate that the surface boundary condition as well as the rest of the explicit computer code was programmed correctly. The numerical studies on the wing also indicate that the origin of the total pressure loss is an expansion of the flow around the sharp leading edge of the nacelle. The sharp leading edge is a feature of the nacelle geometry made necessary by the H-grid. The

studies additionally indicate that by eliminating the nearly discontinuous expansion, the total pressure losses can be eliminated.

These ideas are demonstrated for the nacelle in figures 17 and 18. Figure 17 presents the solution for the computations made with the explicit numerical computational technique at a free stream Mach number of 0.80 and an angle of attack of 0.0^{o}. Parts (a) and (b) of the figure show respectively the Mach number contours and the velocity vectors in the vicinity of the leading edge of the nacelle. They illustrate that contrary to what one would expect at 0.0^{o} angle of attack, the flow stagnates on the external surface of the nacelle and expands around the sharp leading edge to the internal surface.

The stagnation point on the external surface can be seen most clearly from the Mach number contours. The clustering of the Mach number contours at the leading edge indicates the severity of the singularity created in the flow as it expands in traversing the discontinuity in the nacelle surface. The velocity vectors show an inward component of the flow immediately above and in front of the leading edge, and futher indicate that the direction of the flow at the leading edge is from the external surface, around the leading edge, and to the internal surface. Since the first-order damping terms become very large in regions with such strong gradients in the flow, a calculation was made with these dissipation terms turned off. Very little difference could be detected in the solution.

It is thought that this problem would be much less severe for a rounded leading edge coupled with the use of a locally embedded body normal grid such as those normally used for blunt bodies. However, as the appendix shows, care must be taken even with a rounded leading edge and a

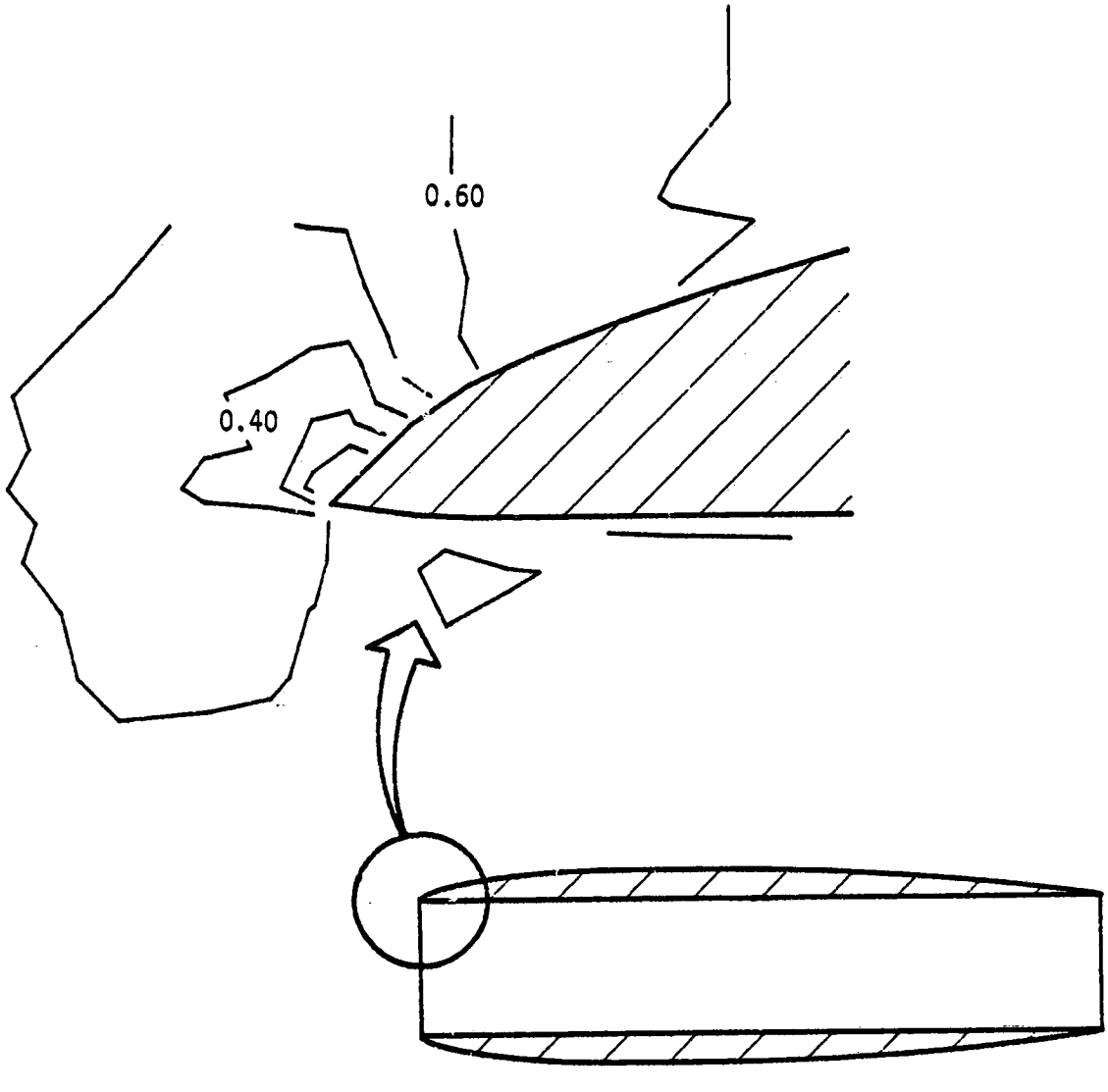

(a) Mach number contours.

Figure 17. Calculated flow-field in the vicinity of the leading edge of the flow-through nacelle. ($M_\infty = 0.80$, $\alpha = 0.0^\circ$, explicit procedure.)

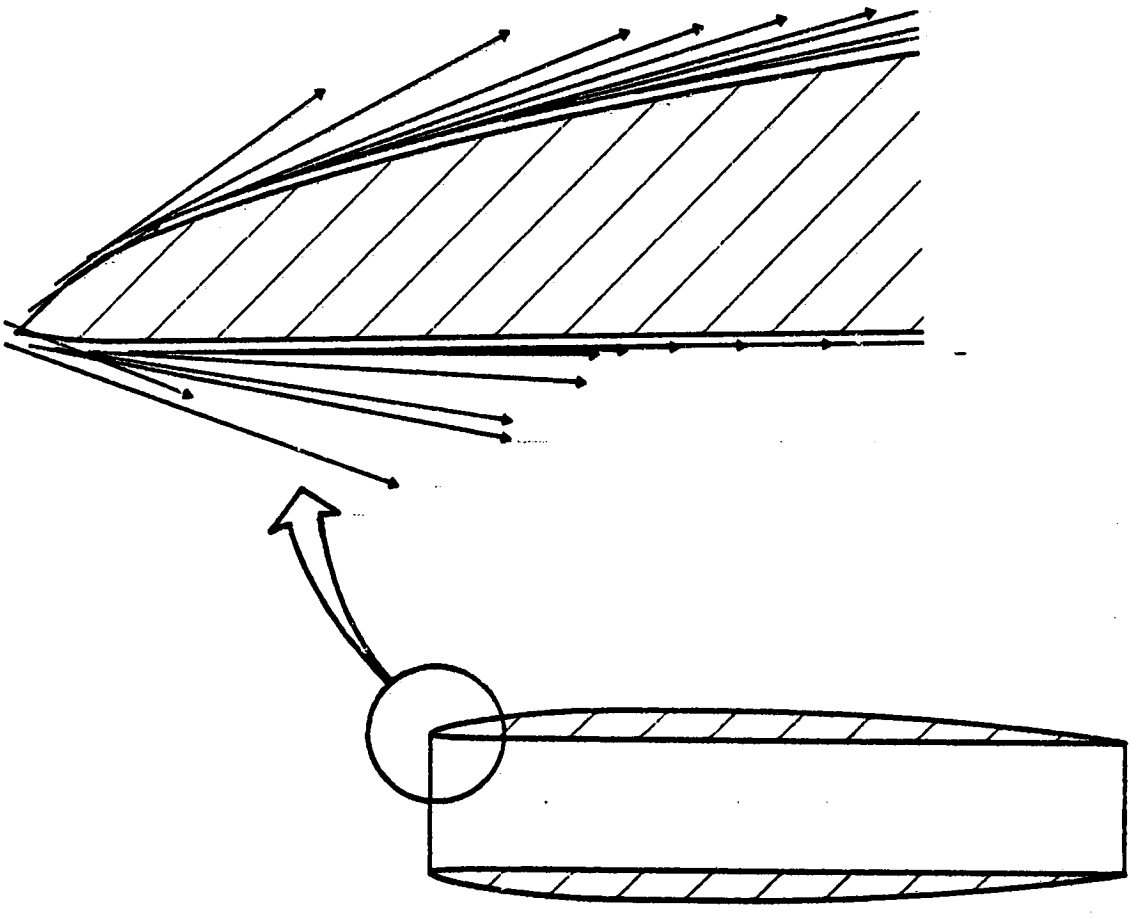

(b) Velocity vectors.

Figure 17. Concluded.

C-type grid. Even with this type grid, the strong gradients generated as the flow expands around the rounded leading edge can for all practical purposes appear as discontinuites unless there are sufficient grid points to resolve the rapid changes in the flow variables.

Eliminating the total pressure loss. To demonstrate that the total pressure losses on the internal surface of the nacelle can be eliminated by eliminating the expansion around the sharp leading edge, calculations were made for a modified flow-through nacelle. The modification to the nacelle consisted of adjusting the mean camber line of the nacelle's airfoil so that the flow stagnated precisely at the leading edge instead of on the external surface. Thus the expansion of the flow around the sharp leading edge was eliminated.

The camber was decreased to 75 percent of the original camber at the leading edge. Along the airfoil, the reduction in camber was progressively decreased according to the square of the cord so that at the trailing edge, the camber remained 100 percent of the original value. The change in the mean camber line necessary to adjust the stagnation point was most noticeable in the first 25 percent of the cord. Figure 18 presents the solution for the modified nacelle with part (a) of the figure showing the pressure coefficient distributions. The pressures look reasonable; however, comparisons with experiment could not be made since no wind-tunnel data was available for the modified configuration.

Mach number contours in the vicinity of the leading edge are presented in part (b) of the figure. They illustrate the fact that the flow does stagnate precisely at the leading edge, and hence does not expand around around the corner. The result, shown in figure 18(c), is

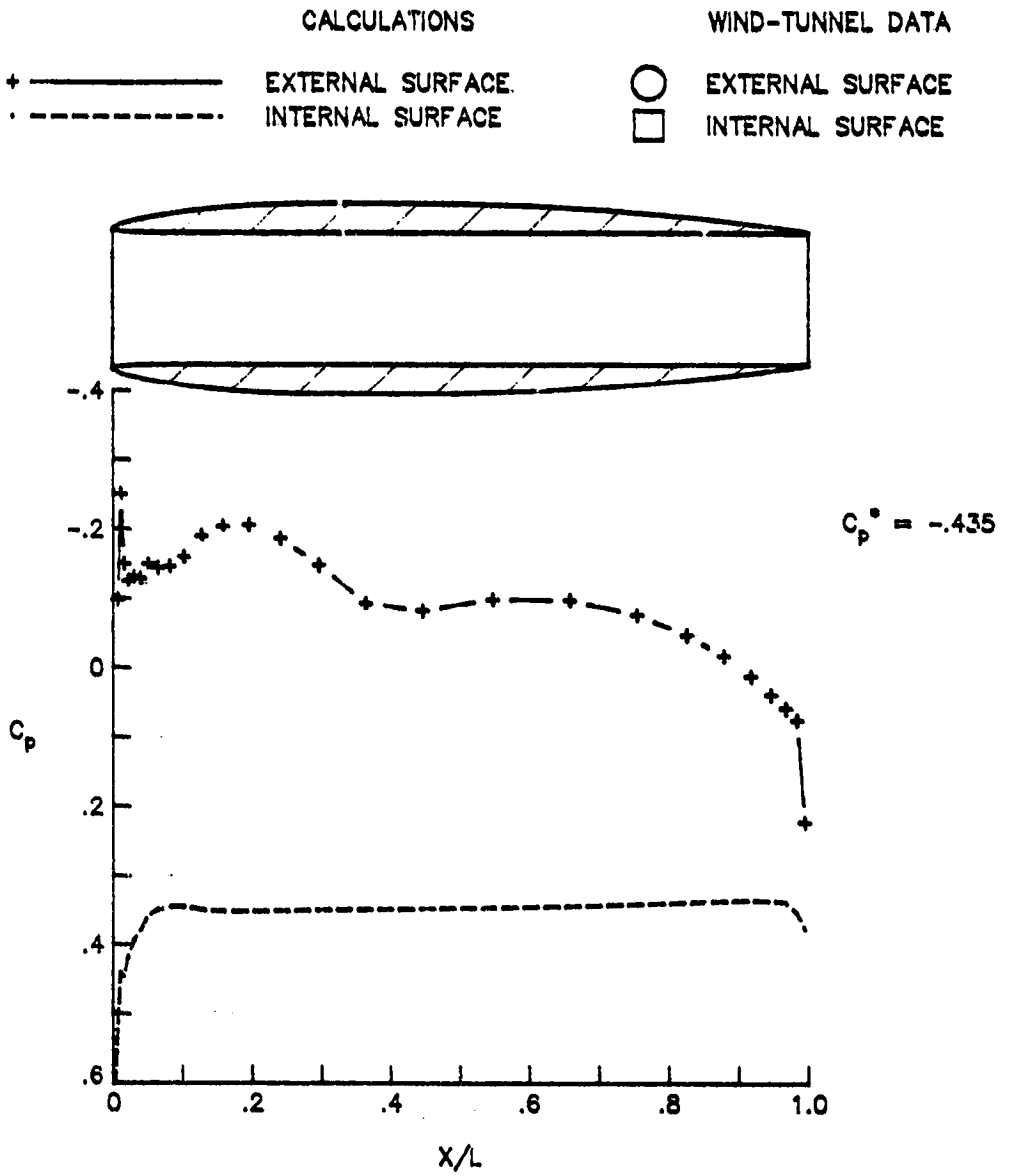

(a) Surface pressure coefficient distributions.

Figure 18. Solution for the modified flow-through nacelle. (M_∞ 0.80, $\alpha = 0.0^0$, explicit procedure.)

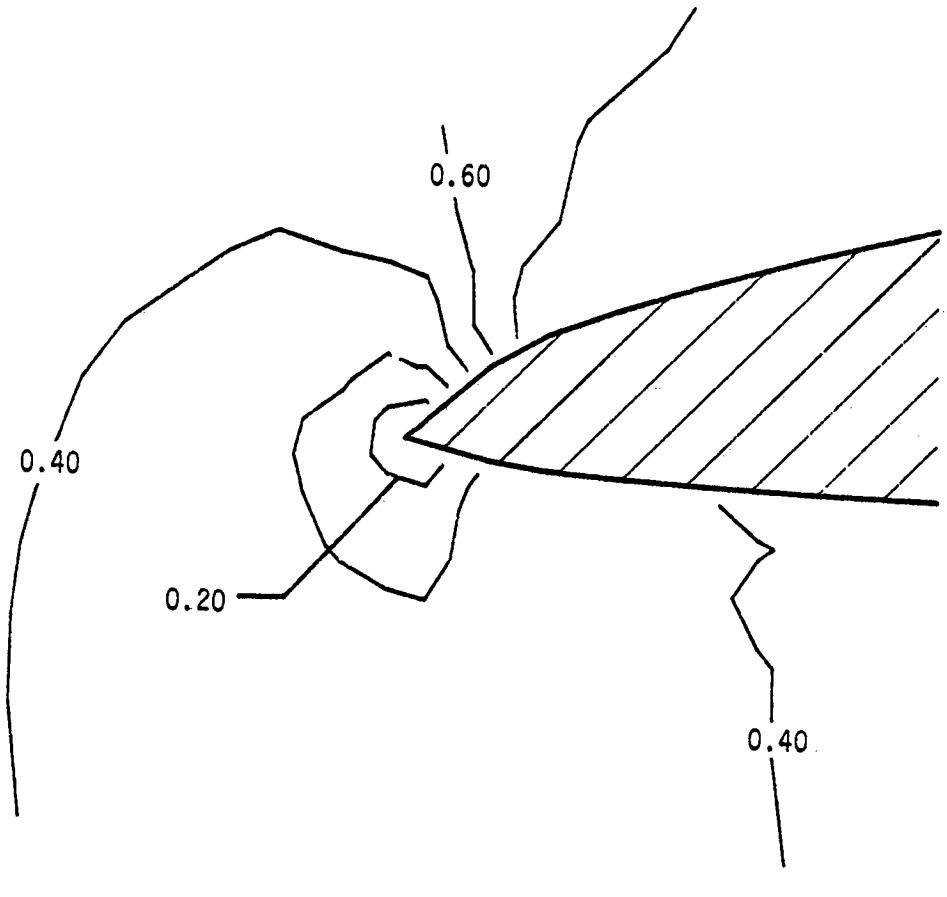

(b) Mach number contours in the vicinity of the leading edge.

Figure 18. Continued.

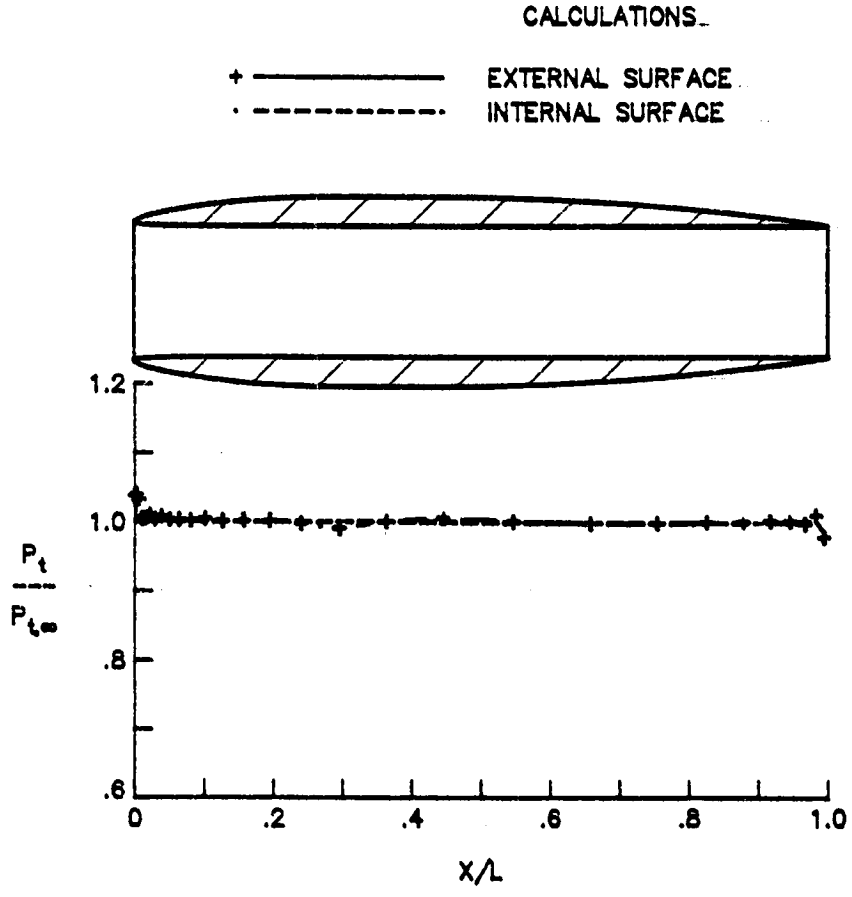

(c) Surface total pressure distributions.

Figure 18. Concluded.

that the total pressure on both the external and the internal surfaces of the nacelle maintains its free stream value. An indication of the amount of change in the nacelle's mean camber line necessary to adjust the stagnation point can be seen by comparing the modified nacelle contour depicted in figure 18(b) with the original nacelle contour depicted in figure 17(a).

The source of the total pressure loss on the surface of the nacelle has been identified as an expansion around the discontinuity in the nacelle's surface at the leading edge. It has also been demonstrated that by eliminating the expansion around the sharp leading edge, the free stream total pressure can be maintained.

Comparison of Techniques

The previous sections in this Chapter have presented a discussion of the solutions calculated by the two computational techniques, an implicit technique employing the three-dimensional Beam and Warming numerical algorithm, and an explicit technique employing the four-stage Runge-Kutta algorithm with implicit residual smoothing. The quality of the solutions obtained with these techniques was compared during the discussion. The comparison on the basis of solution quality will be summarized in this section, and, in addition, practical considerations of implementing the two techniques on the computer will be discussed.

Processing time and computer storage requirements. All numerical calculations were processed on a Control Data Corporation Cyber 203 computer in the scalar mode. For the implicit code, a typical calculation was processed for approximately 1100 time steps on a computational grid containing 18,502 grid points. The calculations were made at a Courant

number of order 11 based on the minimum grid spacing in the axial direction. The processing time on the Cyber 203 was approximately 6.7 hours or 1.22 milliseconds per grid point per time step. The code was written for maximum visibility of the form of the equations, and hence contained many divisions by quantities whose value were 1.00. By eliminating these divisions, and optimising the code for speed of computation, a considerable reduction in processing time should be realized.

The explicit code required an average of 3000 time steps to reach a steady state solution. For the same computational grid, this yielded a computer processing time of approximately 2.1 hours or 0.16 milliseconds per grid point per time step or approximately one third the computational time of the implicit code. Although neither the implicit code nor the explicit code was vectorized, vectorization of the codes should result in a decrease in the processing time.

In order to calculate flows around more complicated configurations, additional grid points will be required. The maximum number of grid points possible for the implicit computer code as it was written was approximately 37,000 before the incore storage capacity of the Cyber 203 computer was exceeded. By deleting all possible arrays in the computer program, and by recomputing the necessary parameters from the deleted arrays every time they were needed, approximately 63,000 grid points could be obtained before the computer's incore storage capacity was exceeded. The maximum number of grid points possible before the explicit code, which was not optimized for minimum storage requirements, exceeded the incore storage capacity of the Cyber 203 was approximately 20,000.

In general, the implicit code requires less computer storage while the explicit code runs faster. Both the run time and the computer storage requirements of each code are marginal for general design studies where many configurations need to be evaluated quickly unless optimization of programming for storage and run time can be realized. However, the cost of obtaining a given solution has steadily decreased by an order of magnitude every eight years for the past fifteen years.[41] Computers which have much more computing power and memory than the Cyber 203 will become available in the very near future. For example, NASA Langley Research Center received a 16 million word version of the Control Data Corporation Cyber 205 in the fall of 1984. Another example is the NAS facility discussed by Ballhaus.[41] With such advances in computer technology, coupled with advances in numerical techniques, computer codes based on solutions of the three-dimensional Euler equations should soon become practical for problems of this complexity.

Convergence. While reasonably accurate engineering solutions were obtained with the implicit technique, its overall convergence properties are unacceptable. The implicit application of the boundary conditions to this problem may enhance its stability and should be investigated, as should the effect of enthalpy damping on its stability characteristics. However, at present, the scheme has a weak instability when applied to this three-dimensonal problem with the result that the implicit solution never actually converges. The explicit scheme is stable and converges even though its rate of convergence is less than desirable.

Accuracy. The relative accuracy of the solutions obtained with the two numerical techniques has already been discussed in the previous

sections. Basically, the explicit technique yields more accurate solutions for the same number of grid points in that it captures the pressure gradients and peak pressure expansions better than the implicit technique. The better accuracy of the explicit code may be a result of the slightly different implementation of the surface boundary conditions in the two numerical procedures. Both procedures, however, give solutions that are in good agreement with experimental data on the external surface of the nacelle where the effects of viscosity are relatively small.

CHAPTER VII

VISCOUS-INVISCID INTERACTING RESULTS

In general, the inviscid solutions calculated by using the Euler computational techniques agree very well with the wind-tunnel data on the external surface of the nacelle. However, there are large differences between the inviscid solutions and the measured pressures inside the nacelle's duct. In Chapter VI, it was hypothesized that since the Euler equations model compressibility and rotationality, the discrepancy was due to viscous dissipation present in the experiement. In the physically realistic case, strong interactions often occur between the viscous boundary layer and the main stream even when the boundary layer does not separate. Typical examples of this type of flow occur near the trailing edge of an aft-loaded airfoil or at a shock-boundary-layer interaction. In these instances, modeling the frictional forces becomes essential if accuracy is to be maintained.

Therefore, to complete the study of the solution of the flow field for the flow-through nacelle, a preliminary assessment was made of the the influence of viscosity. The viscous-inviscid interacting computational model described in Chapter V was used for this phase of the research which was conducted at a free stream Mach number of 0.80 and an angle-of-attack of 0.0^{o}. These investigations, which have yielded new insight into the mechanics of the interactions between the internal and external flows, are described in the present chapter.

Results

Overall viscous effects. The overall result of including the boundary layer effects in the otherwise inviscid Euler solution is illustrated in figure 19. The figure presents the viscous-inviscid interacting solution as well as the inviscid solution, and illustrates that the viscous effects significantly change the internal pressures but leave the external pressures largely unchanged. Including the boundary layer and wake does result in a slight decrease in the external pressures very near the trailing edge. However, on the internal surface, it causes a significant decrease in the exit pressure, and produces a sizable axial pressure gradient in the nacelle's duct. The net effect improves the correlation between the computed internal pressures and the experimental data.

As pointed out previously, in addition to surface boundary layer thickness, this interacting procedure compensates for wake thickness but not wake curvature. Melnik[34] indicates that wake curvature, while not being as important as wake thickness, produces similar results. Hence, if allowance were made for wake curvature in the present calculations, the computations should match the internal pressure datum even better.

External and internal boundary layers. An attempt was made to determine the relative importance of the external and internal boundary layers in changing the character of the flow past the nacelle. Therefore, in addition to the inviscid and the complete viscous-inviscid interacting solutions, interacting computations were made with the the boundary layer and wake originating only from the external surface of the nacelle.

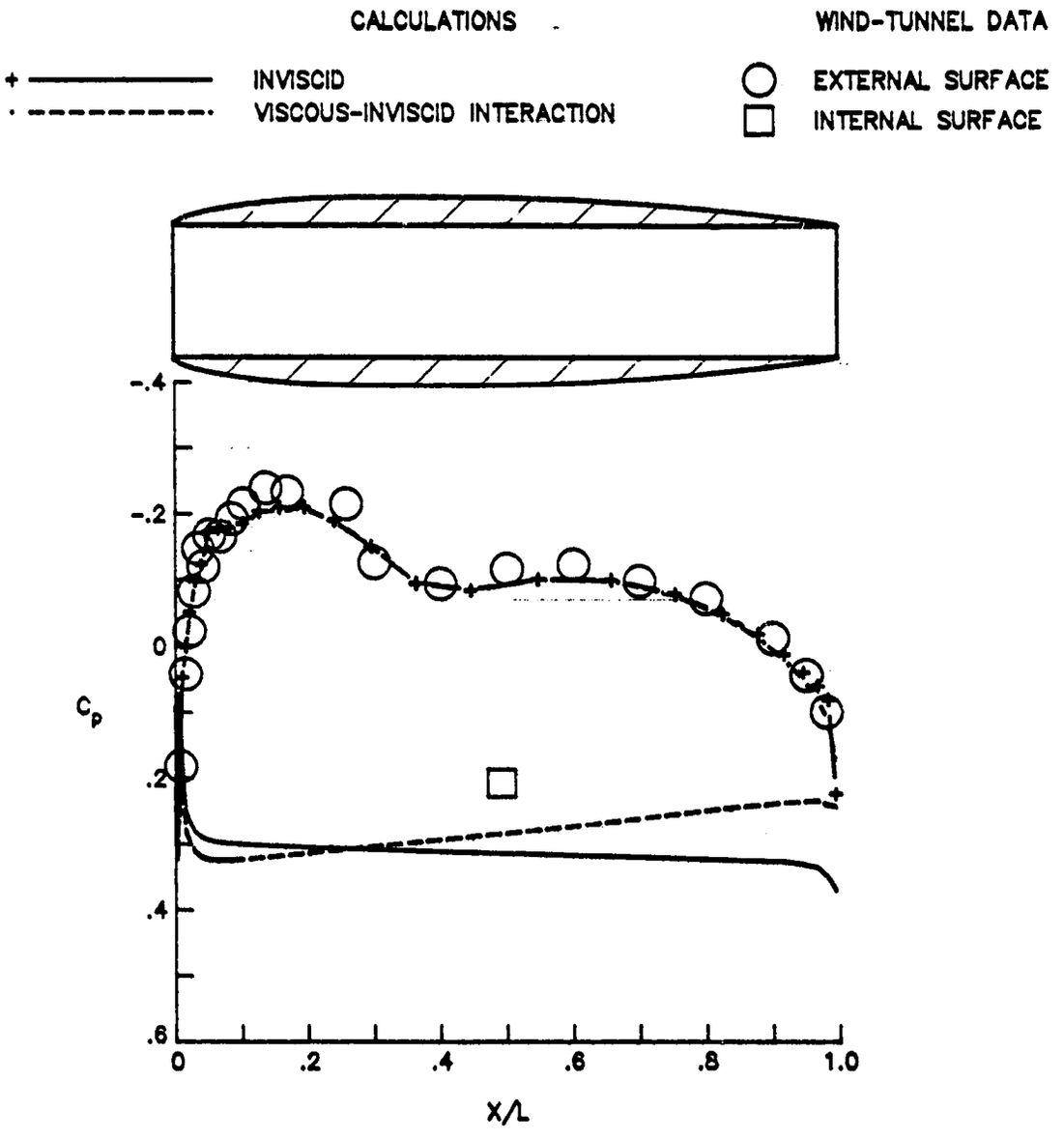

Figure 19. Effect of viscous-inviscid interaction on the nacelle pressures. (M_∞ = 0.80, α = 0.0°.)

Similar computations were also made with the boundary layer and wake originating only from the internal surface.

Figure 20 presents the computed pressure distributions on the external surface of the nacelle for all four solutions, and shows that neither the external nor the internal boundary layers greatly influence the outside pressures. The viscous effects on the internal nacelle pressures are illustrated in figure 21. These effects are substantial, and consist of both a change in the overall pressure level and the generation of a pressure gradient in the axial direction.

First consider the influence of the boundary layer and wake originating from only the external surface of the nacelle. Part (a) of figure 21 contains the pressure distributions for the complete viscous-inviscid interacting solution, and for the solution which includes the viscous effects produced by only the external nacelle surface. The common factor between the curves is that each includes the viscous effects originating from the external surface of the nacelle. Even though there are differences in the pressure gradients between the two calculations, the exit pressures in both cases are the same.

In part (b) of figure 21, the viscous effects due to the external nacelle surface are absent. Part (b) presents the inviscid solution and the interacting solution with only the internal boundary layer and wake. As in part (a), the pressure gradients are different but the exit pressures of both curves are equal. The message of the comparisons is that the external boundary layer and its wake in combination with the inviscid flow determine the exit pressure and hence the overall pressure level of the internal flow. The internal boundary layer has very little effect on the exit pressure. Comparing parts (a) and (b) also illustrates

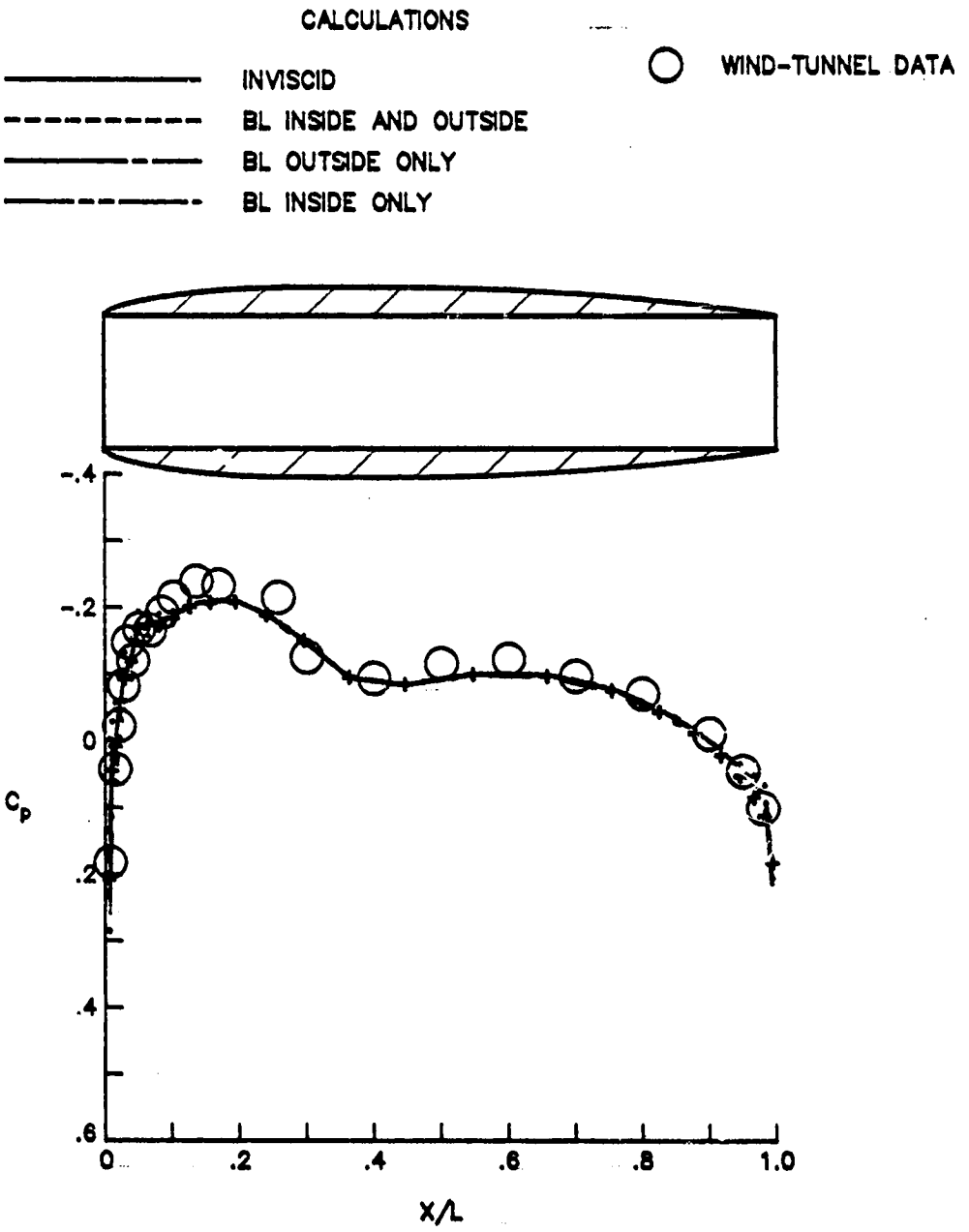

Figure 20. Viscous effects on the external nacelle pressures.

(M_∞ = 0.80, α = 0.0°.)

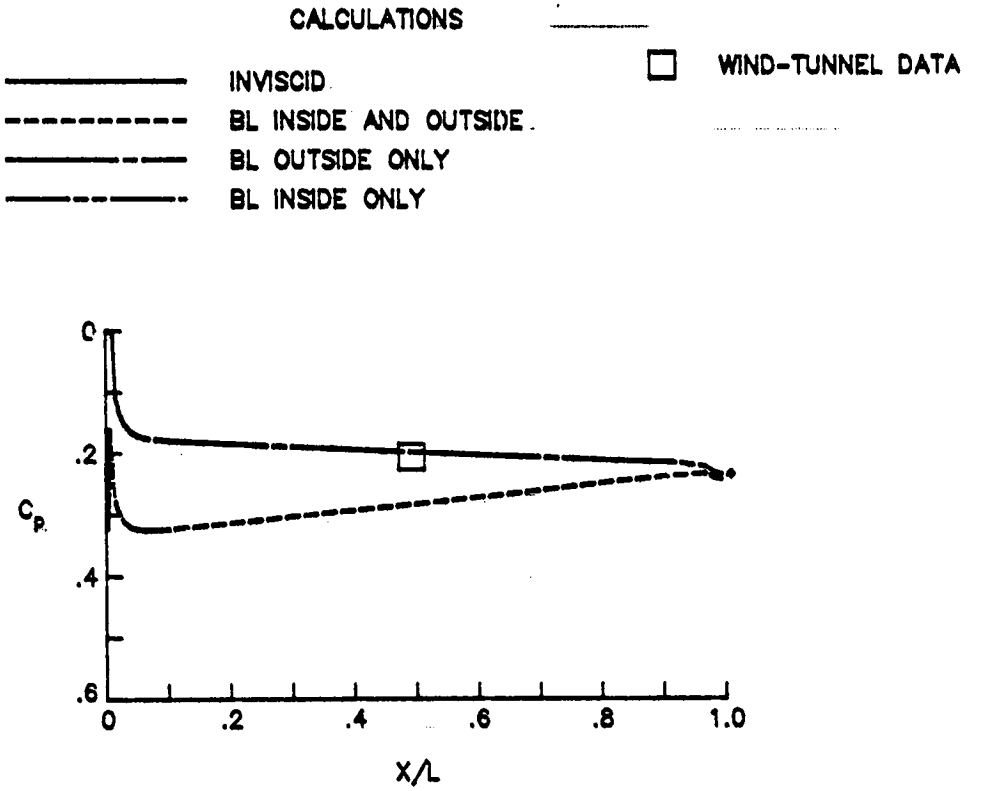

(a) Total versus external viscous-inviscid interaction.

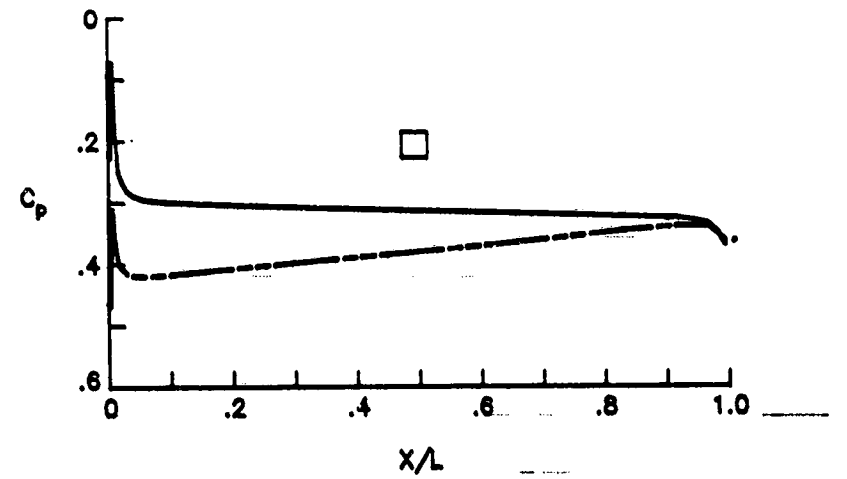

(b) Inviscid versus internal viscous-inviscid interaction.

Figure 21. Viscous effects on the internal nacelle pressures.

(M_∞ = 0.80, α = 0.0°.)

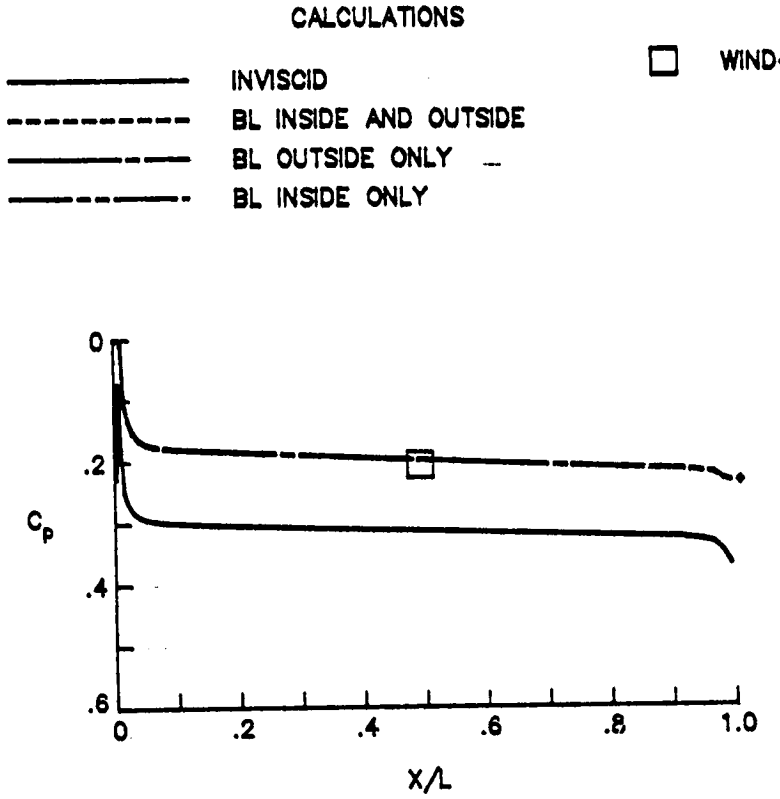

(c) Inviscid versus external viscous-inviscid interaction.

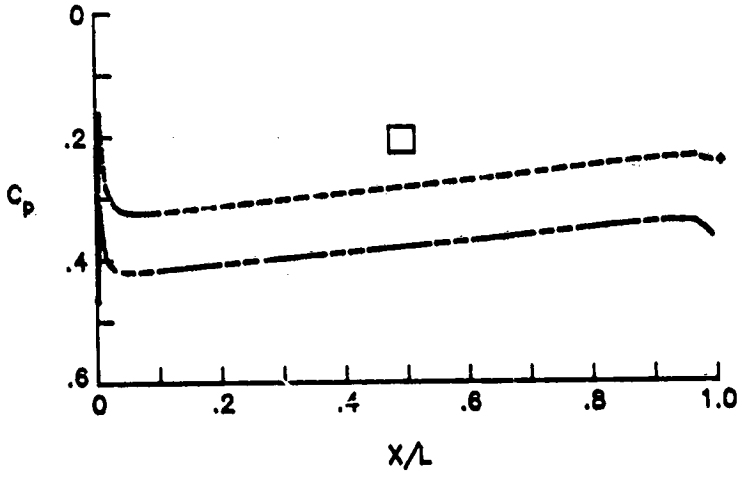

(d) Total versus internal viscous-inviscid interaction.

Figure 21. Concluded.

that the external viscous effects produce a lower exit pressure and hence a lower overall internal pressure that is in better agreement with the wind-tunnel data.

Next, consider the effect of the boundary layer originating from only the internal surface of the nacelle. In parts (c) and (d) of figure 21, the correlating factor is the viscous effects produced by the inside nacelle surface. In part (c), both pressure distributions are the result of calculations in which the internal viscous effects are absent, and in part (d) both are the result of calculations with them present. An examination of both sets of pressure distributions illustrates that the boundary layer on the internal surface of the nacelle produces a pressure gradient in the nacelle duct. In addition, it shows that the gradient is essentially unaffected by the boundary layer on the outside surface. One dimensional axisymmetric calculations demonstrate that the gradient is the result of the change in the effective duct area due to the growth of the internal boundary layer. For example, the one-dimensional calculation yielded a pressure coefficient gradient of 0.13 versus the gradient of 0.11 given by the present viscous-inviscid calculation.

Interacting mechanism. A more complete understanding of the mechanism by which the boundary layer produces these results, and of the relative influence of each boundary layer on the overall flow pattern can be gained by also considering figures 22, 23 and 24. Figure 22 shows the strength of the sources and sinks that are imposed on the nacelle surface and in the wake in order to satisfy the transpiration boundary conditions for the continuity equation. The strengths are equivalent to the streamwise rate of change of the mass flow deficit produced by the boundary

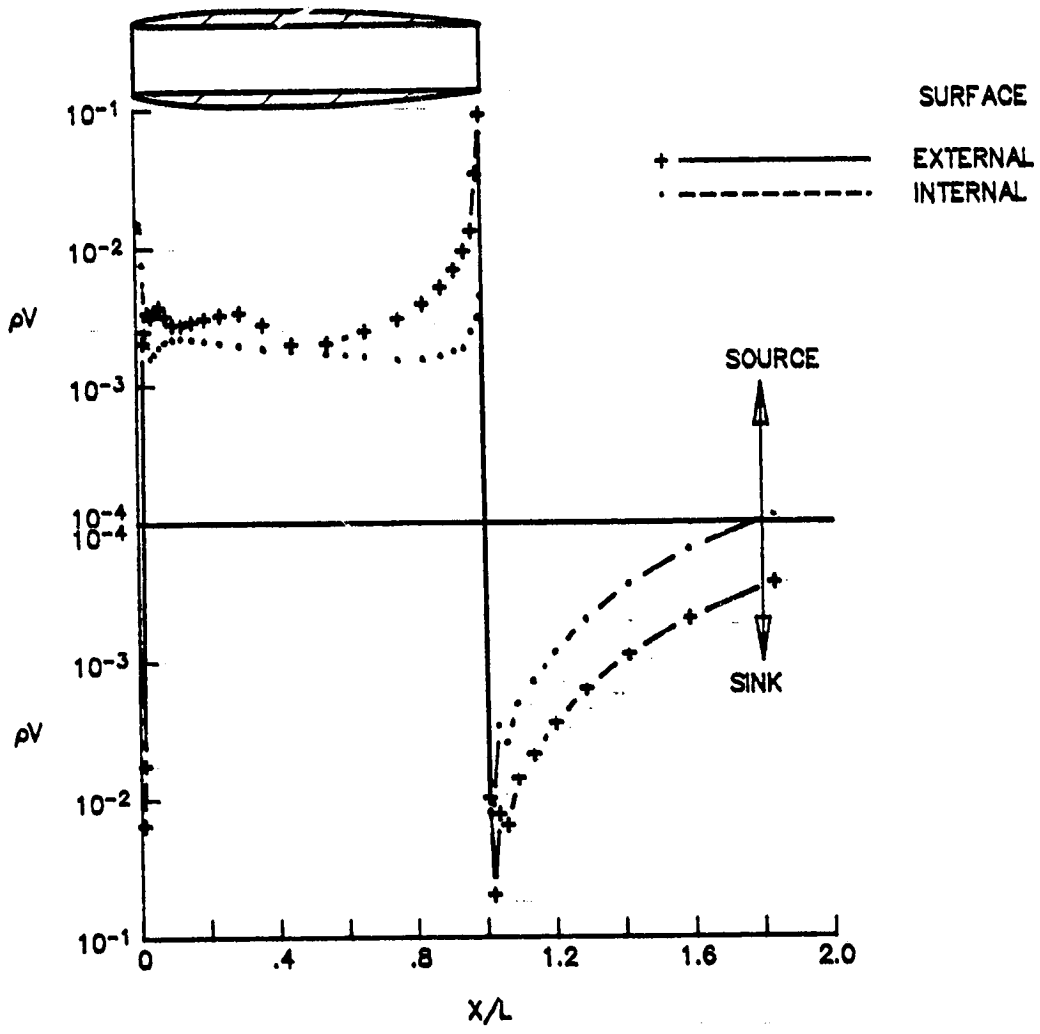

Figure 22. Transpiration boundary condition parameters for the continuity equation. (M_∞ = 0.80, $\alpha = 0.0^o$.)

layer or wake. The figure illustrates that the external boundary layer and its associated wake result in boundary conditions that are nearly an order of magnitude larger than those associated with the internal boundary layer and wake. The figure further shows that the dominating portion of the external viscous effects comes from the trailing edge region where there is a rapid deceleration of the external flow and consequently a rapid buildup of the boundary layer.

The influence of these viscous boundary conditions on the flow field in the vicinity of the trailing edge is illustrated in figure 23. Part (a) of the figure shows the velocity vectors in the vicinity of the trailing edge for the inviscid solution, and part (b) the corresponding vectors for the interacting solution. Comparing the two velocity vector plots illustrates the difference in the basic nature of the two solutions; the inviscid solution possesses a greater inward radial component of the flow which suggests a greater circulation.

A quantitative comparison of the viscous boundary conditions on the velocity vectors immediately downstream of the trailing edge of the nacelle is presented in figure 24. Part (a) of the figure presents the velocity vectors of the inviscid Euler solution, and the interacting solution with only the external viscous effects. It shows that the viscous effects originating from the external surface straighten out the streamlines, thus reducing the circulation in the trailing edge region. The effects of viscosity produced by the internal surface, part (b), show the opposite effect, but are much smaller in magnitude as would be expected from the results presented in figure 22. The net effect on the velocity vectors immediately downstream of the trailing edge is presented in figure 24(c). Basically, the viscous effects reduce the inward radial

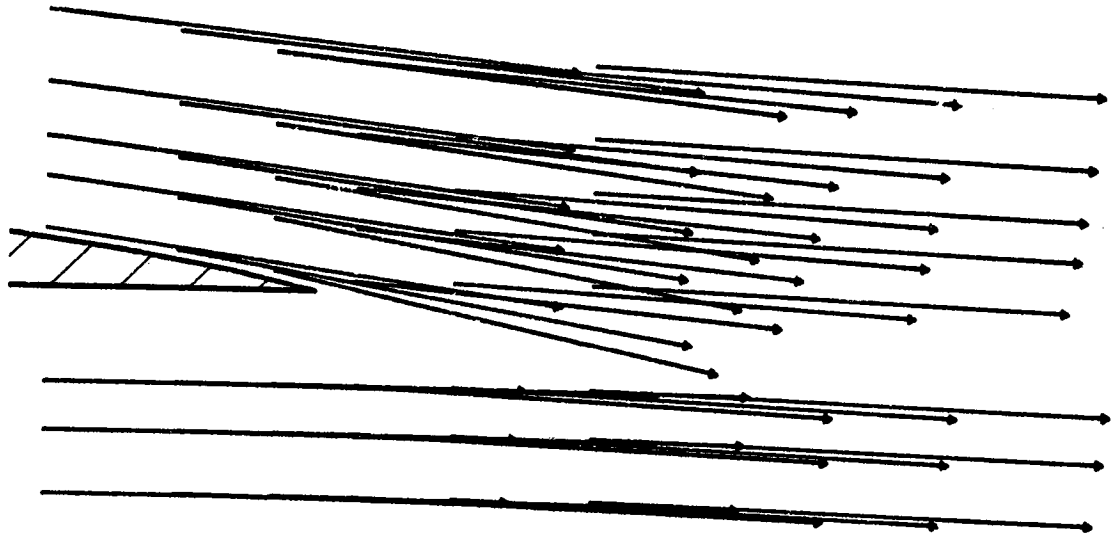

(a) Inviscid velocity vectors.

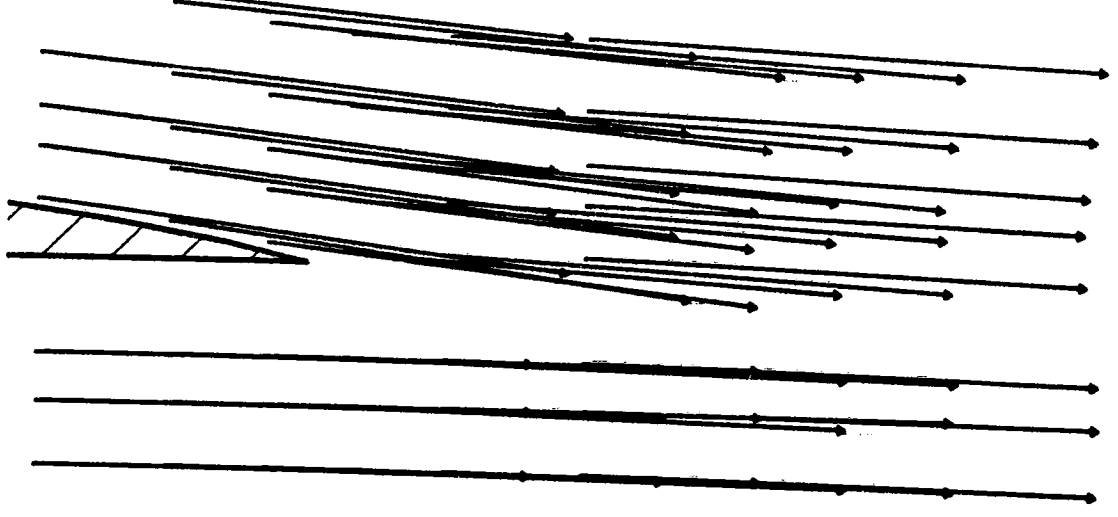

(b) Viscous-inviscid interacting velocity vectors.

Figure 23. Viscous effects on the velocities in the vicinity of the trailing edge. (M_∞ = 0.80, α = 0.0°.)

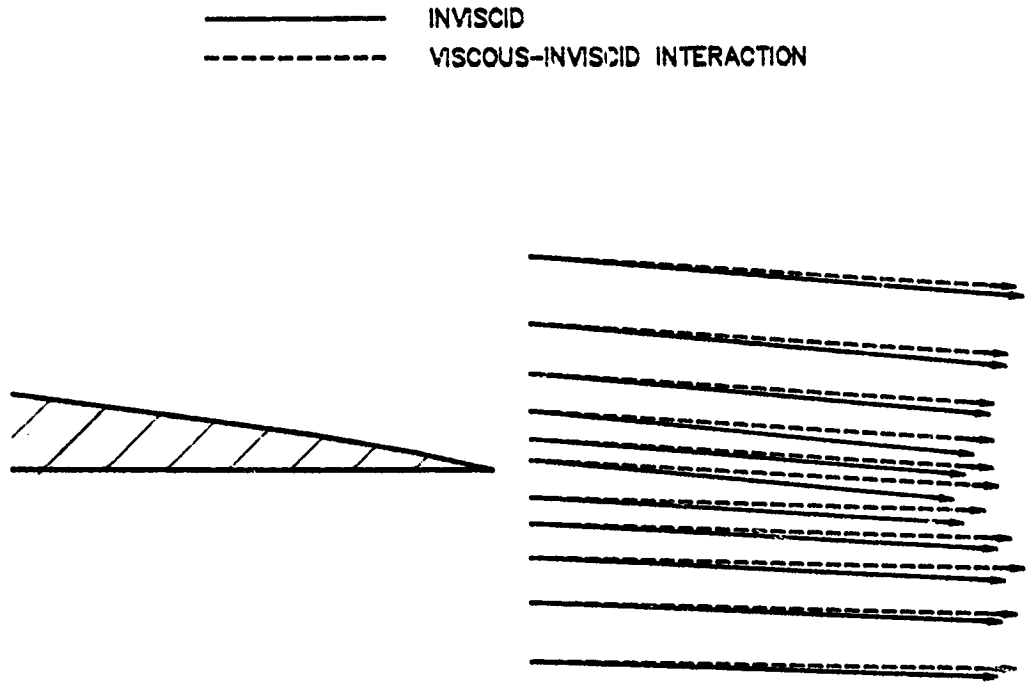

(a) Inviscid versus external viscous-inviscid interaction.

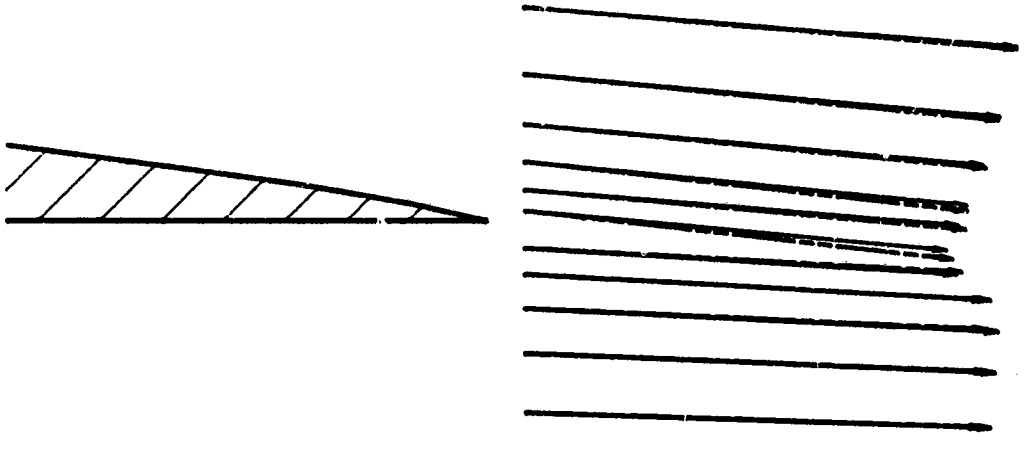

(b) Inviscid versus internal viscous-inviscid interaction.

Figure 24. Detailed comparison of velocities immediately downstream of the trailing edge. (viscous and inviscid solutions, $M_\infty = 0.80$, $\alpha = 0.0^0$.)

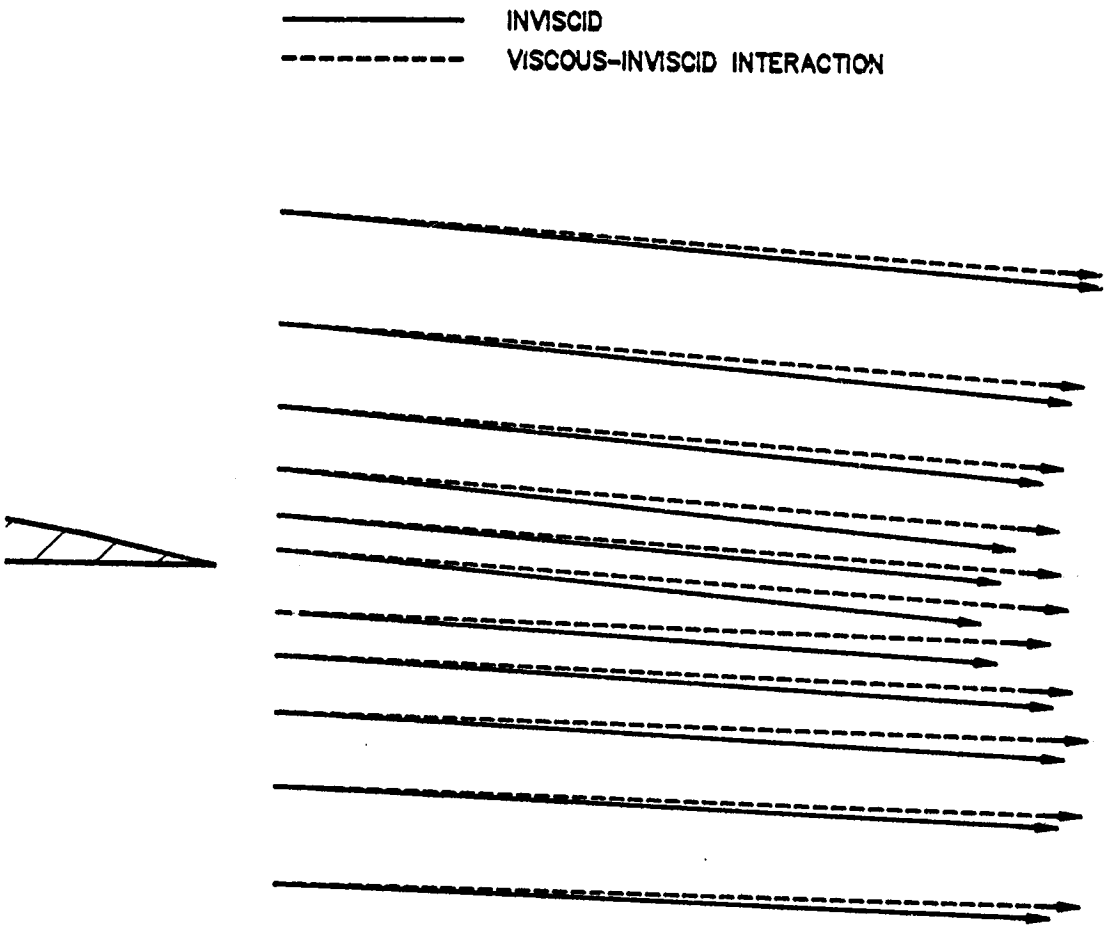

(c) Inviscid versus complete viscous-inviscid interaction.

Figure 24. Concluded.

velocity component of the mainstream and increase its streamwise component.

Decambering concept. The external viscous effects produce a change in the stream velocities that is similar to a change that would be produced by decambering the nacelle's airfoil. The analysis presented above strongly indicates that the decambering effect is responsible for decreasing the exit pressure and the overall internal pressure level from their inviscid values. This theory can be further evaluated by two completely inviscid tests. For the first test, recall the comparison of the two inviscid solutions which were calculated with the implicit computational procedure (see figures 3(a) and 11). For the "non-Kutta" calculation presented in figure 11, a substantial inward radial velocity existed at the trailing edge of the nacelle. For the "Kutta" calculation presented in figure 3(a), this velocity was set equal to zero. As would be expected, imposing the "Kutta" condition lowered the internal pressure level so that it agrees much better with experiment.

The second test was conducted with the explicit Euler code. In this test, an infinitely thin trailing edge extension, or tab, was attached to the nacelle parallel to its axis of symmetry. Calculations using this configuration produced even more dramatic results than those of the first test. The internal pressure coefficient was lowered from 0.3, a value which was higher than the experimental pressure coefficient, to 0.1, a value approximately one half the experimental pressure coefficient.

The results presented above show that the external boundary layer effectively decambers the airfoil of the nacelle and alters the overall flow pattern by redirecting the streamlines closer to the free stream

direction. A sketch of the inviscid and viscous streamlines is presented in figure 25. The compression on the external surface of the nacelle is thus weakened, resulting in a less positive exit pressure and a less positive internal pressure level which agrees better with wind-tunnel data than the inviscid computations.

Implications of viscous effects. It is obvious that the magnitude of these results is configuration dependent. However, one concludes that, in the absence of any artificial "Kutta" condition, the Euler equations give the correct inviscid trends. That is, that the inviscid pressure level inside the nacelle's duct is more positive than would be experienced in reality. Hence, if simulation of the correct mass flow through the nacelle's duct is important in analyzing a fluid flow problem, then viscous effects must be included in the computational model.

These implications also extend to wind-tunnel testing of models with flow-through nacelles. In the early stages of developing a new aircraft, when many different configurations must be tested, the complications and expense associated with testing powered models necessitates the use of models with flow-through nacelles. Adjustments to the flow-through data are then determined by testing powered versions of the most promising configurations. This experimental procedure was followed by Capone et. al[42] in determining the overall aerodynamic characteristics of a new fighter aircraft. As the present viscous-inviscid investigation shows, the external boundary layer on the nacelles can affect the internal mass flow as well as the pattern of the streamlines both behind and in front of the nacelle. Thus, the accuracy of simulating the nacelle boundary layer could significantly impact the measured aerodynamic characteristics of the

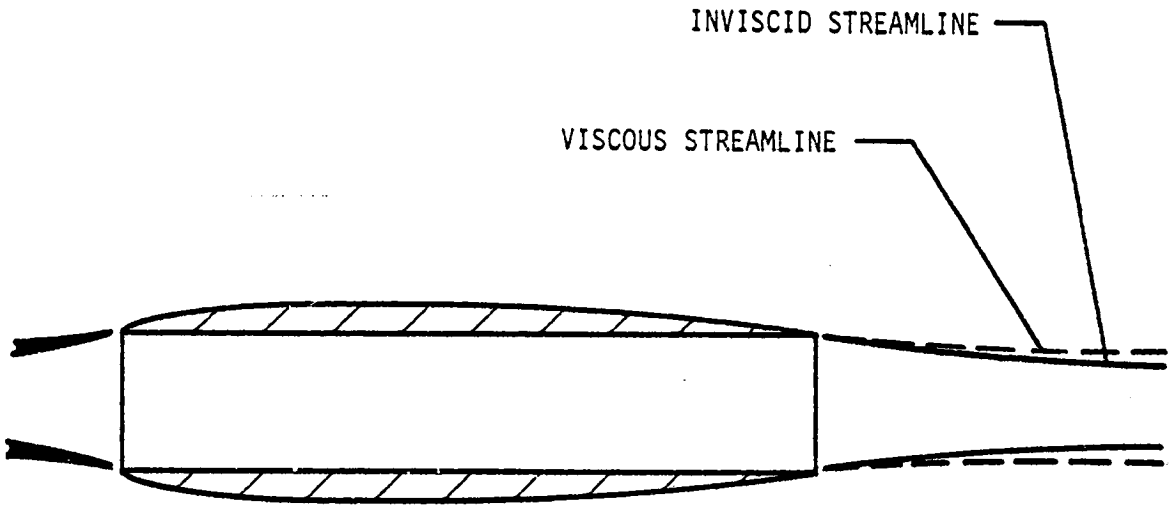

Figure 25. Sketch of the inviscid and viscous streamlines.

configuration.

Summary of the Viscous Effects

In summary, for predicting the flow on the external surface of the nacelle, viscous effects were relatively unimportant and the Euler equations gave good solutions. In contrast, for predicting the flow inside the nacelle's duct, the viscous effects are extremely important and both the external and internal boundary layers and wakes must be simulated. The internal boundary layer creates an axial pressure gradient in the nacelle's duct, but essentially does not affect the overall pressure level. The external boundary layer and its associated wake change the overall pattern of the inviscid flow. They displace the streamlines away from the external surface of the nacelle thus effectively decambering the nacelle's airfoil. As a result, the compression at the trailing edge is weakened. This gives a less positive exit pressure, and hence a less positive overall internal pressure level which is closer to the free stream value and agrees better with wind-tunnel data than the inviscid computations. Hence, if simulating the correct mass flow through the nacelle's duct is important, then viscous effects must be included in the computational model.

CHAPTER VIII

CONCLUDING REMARKS

A study has been made of the solution of the three-dimensional flow field for a flow-through nacelle. Both inviscid and viscous-inviscid interacting solutions were examined. Inviscid solutions were obtained with two different computational procedures for solving the three-dimensional Euler equations. The first procedure employs an approximately-factored alternating-direction-implicit numerical algorithm, and required the development of a complete computational model specifically geared to the nacelle problem. The second computational technique employs a fourth-order Runge-Kutta numerical algorithm which was modified to fit the nacelle problem. Viscous effects on the flow field were evaluated with a viscous-inviscid interacting computational model. This model was constructed by coupling the explicit Euler solution procedure with a "lag-entrainment" boundary layer solution procedure in a global iteration scheme. The computational techniques have been used to compute the flow field for a long-duct turbofan engine nacelle at free-stream Mach numbers of 0.80 and 0.94 and angles of attack of 0^{o} and 4^{o}.

The numerical experiments show that for predicting the flow inside the nacelle duct, the viscous effects are extremely important and both the external and internal boundary layers and wakes must be simulated. The internal boundary layer creates a pressure gradient in the nacelle duct. The external boundary layer and wake displace the streamlines away from

the external surface of the nacelle, thereby reducing the compression at the trailing edge. This gives a less positive exit pressure, and hence a less positive overall internal pressure level which agrees better with experiment than the inviscid computations.

In contrast to the internal surface, viscous effects were relatively unimportant for predicting the flow on the external surface of the nacelle. Good agreement is shown between the computational results of both Euler numerical procedures and wind-tunnel data on the external surface of the nacelle. The solutions at 0^{o} angle of attack exhibit the proper axisymmetric behavior even though the computational techniques are three dimensional. At 4^{o} angle of attack, the solution has a definite three-dimensional character. The calculations correctly predict the changing nature of the flow at the supercritical free stream Mach number of 0.94, and predict the quantitative results at this Mach number very well.

The solutions using both Euler computational techniques exhibited a total pressure loss on the internal surface of the nacelle. An investigation of the loss proved that it was the result of the flow stagnating on the external surface and expanding around the sharp discontinuity in the surface of the nacelle at its leading edge. The studies indicate that the use of C-type grids could probably eliminate the loss, although even with the C-grid, care must be taken to use sufficient grid resolution to resolve the stagnation region near the leading edge. However, for sharp leading edges or where the H-type grid is otherwise desirable, it appears that some (problem-dependent) total pressure loss is inherent to numerical Euler-equation solutions.

Finally, in comparing the two numerical techniques, the explicit computational technique gives a more accurate solution for the same number of grid points than the implicit technique. The implicit computer code requires less computer storage while the explicit code runs faster. For the implicit computational procedure, it was found that a radiation boundary condition imposed at the far-field and outflow boundaries gives better convergence of the computations than the condition $p = p_\infty$. Even though reasonably accurate engineering solutions were obtained with the implicit computational procedure, a weak instability was discovered in it when applied to the three-dimensional nacelle problem and the solutions never actually converged. This instability would severly restrict the use of this implicit method for studying problems of this type. The explicit computational technique is stable; however, its convergence rate is less than desirable. The weak instability of the implicit scheme coupled with the slow rate of convergence of the explicit scheme provides motivation for further algorithm development.

APPENDIX

TWO-DIMENSIONAL INVESTIGATION OF THE TOTAL PRESSURE LOSS

In Chapter VI, part of the discussion centered upon a total pressure loss in the computed flow on the internal surface of the nacelle, a feature of the flow that is physically incorrect. It was stated that the loss was first noticed for the solutions obtained with the alternating-direction-implicit computational procedure, and that at the time, it was attributed to incorrect treatment of the leading edge boundary. The explicit Runge-Kutta computational procedure does not contain a direct treatment of the leading edge boundary. Therefore, when solutions computed by the explicit procedure contained a similar loss in total pressure an investigation to determine the cause of the loss was considered desirable. This appendix summarizes the resulting investigation.

For the more detailed investigation into the source of the loss, an unswept, untapered wing was chosen as the test configuration. Using the unswept, untapered wing resulted in a physical problem with two-dimensional flow, but retained the three-dimensionality of the computational procedure. Symmetry of the boundary conditions could be maintained. Also, by adopting a symmetrical airfoil, and by comparing the solutions on the top and bottom surfaces of the wing, the coding of the surface boundary condition inside the nacelle could be verified. This was possible because the boundary conditions, and hence the computer codings,

for the bottom surface of the wing and for the inside surface of the nacelle are identical.

Solutions for the wing were obtained using the explicit Runge-Kutta algorithm for both a symmetrical airfoil and a cambered airfoil with H-grids and C-grids. Figure A-1 shows examples of the two types of grids. The H-grid resembled as closely as possible the grid used for the nacelle. All calculations presented in the appendix are at an angle of attack of 0.0^{o}.

Figure A-2 presents the solution at a free stream Mach number of 0.80 for a wing with a symmetrical airfoil and an H-grid. The solution is symmetrical about the cord line, and, even though there are regions of supersonic flow, the total pressures on both surfaces are essentially at the free stream value. The slight variation in the total pressures where the flow compresses from the negative pressure peak is possibly the result of excessive numerical dissipation. The symmetry of this solution, and the equality of the total pressures on the surface to the free stream total pressure strongly indicates that the surface boundary condition is programed correctly.

The computed total pressures for the wing with a cambered airfoil having the same cross-section as the nacelle and an H-grid are presented in figure A-3. This solution is also at a free stream Mach number of 0.80 and an angle of attack of 0.0^{o}. The figure shows that there is a larger total pressure loss on the bottom surface of the wing than on the corresponding inside surface of the nacelle, and there is even a loss on the top surface.

In order to investigate the effect of rounding the leading edge, it's contour was changed to a circular arc which was tangent to the top

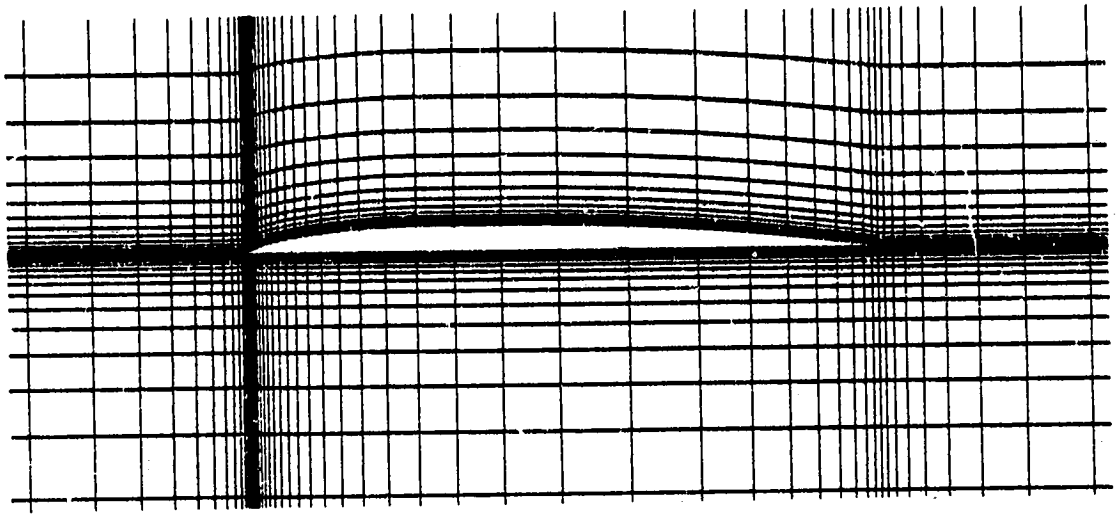

(a) H-type grid.

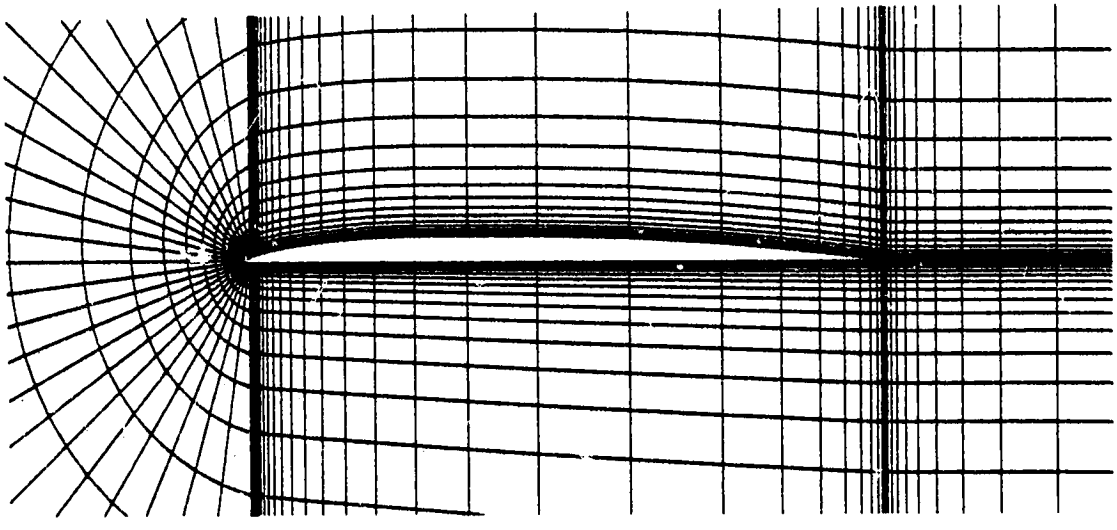

(b) C-type grid.

Figure A-1. Typical wing grids.

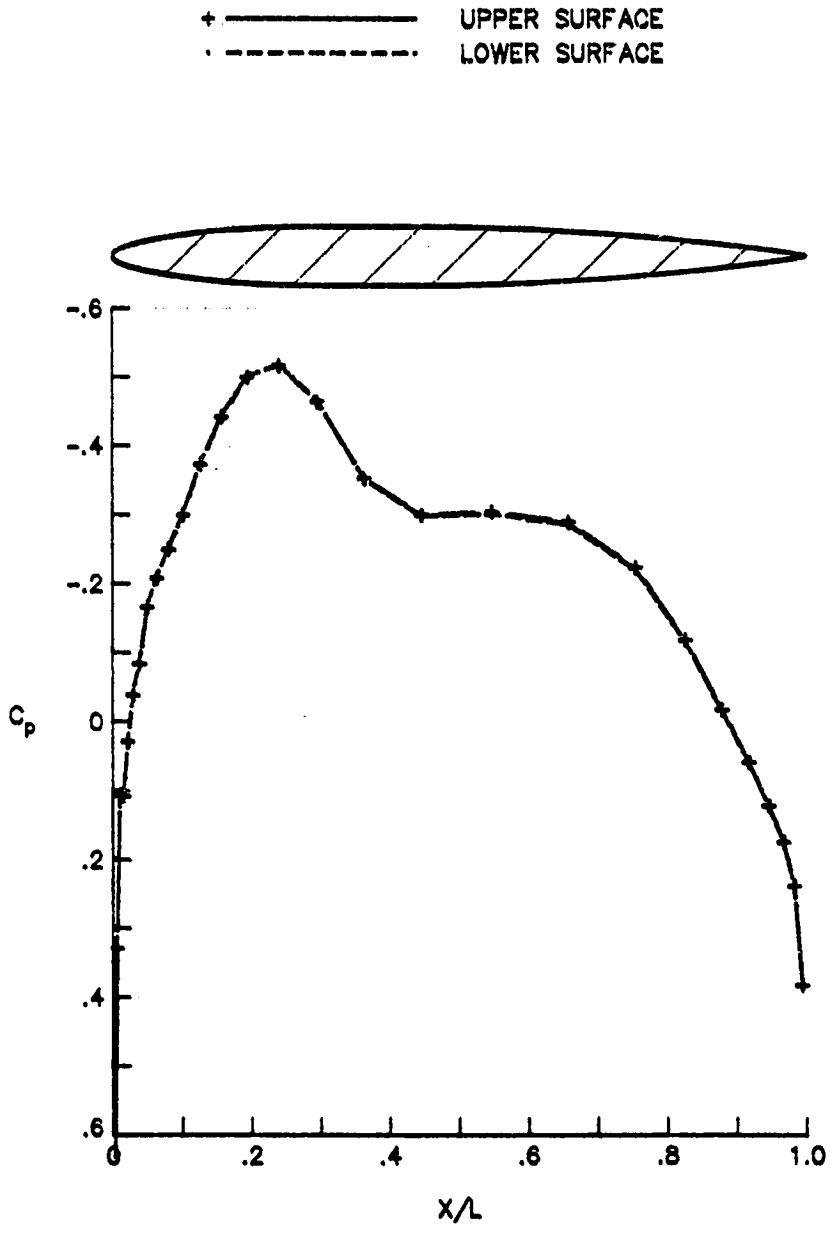

(a) Pressure coefficient distributions.

Figure A-2. Solution for the wing with a symmetrical airfoil.

(M_∞ = 0.80, α = 0^o, H-grid.)

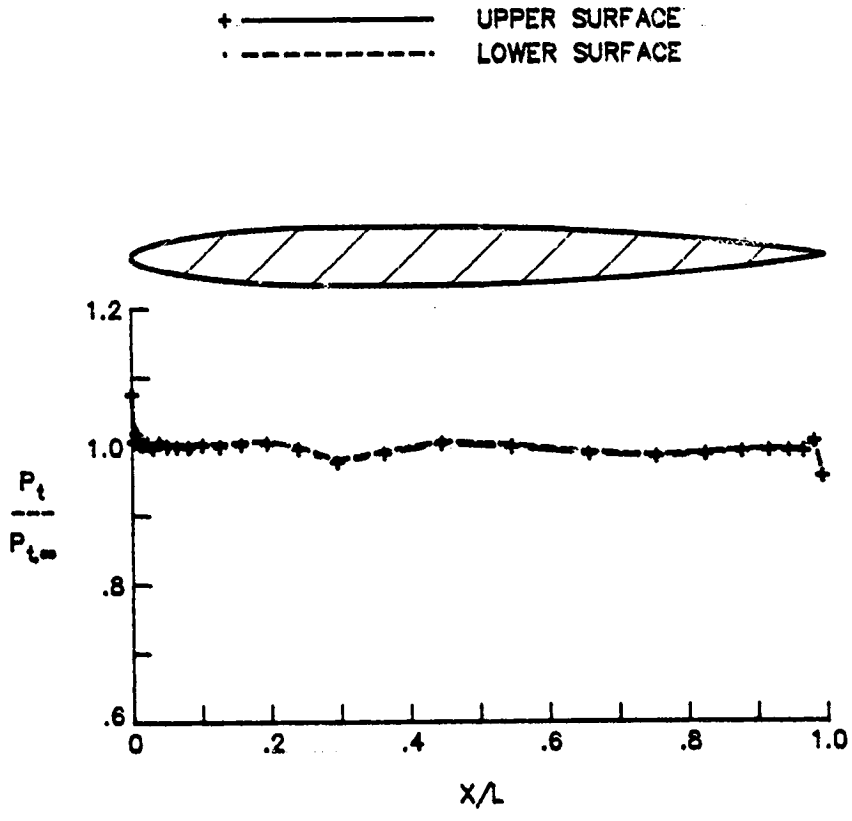

(b) Total pressure distributions.

Figure A-2. Concluded.

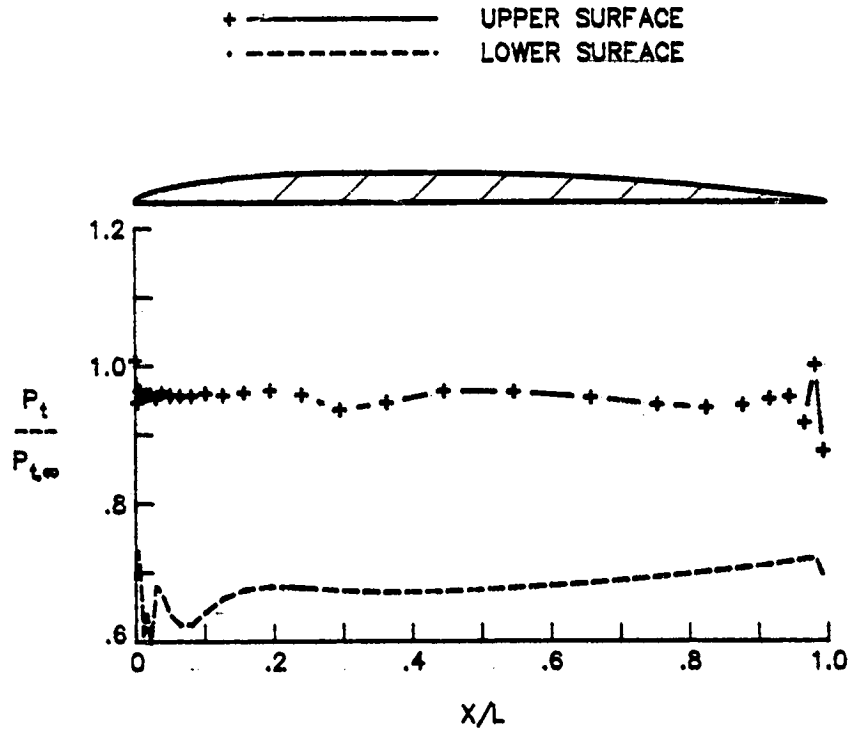

Figure A-3. Computed total pressures for the wing with a cambered airfoil and an H-grid. (M_∞ = 0.80, $\alpha = 0.0^o$)

and bottom surfaces of the airfoil, and a C-grid was adopted. Figure A-4(a) presents the total pressure distributions for this configuration at the same free stream conditions as the previous calculations. It shows that while the the total pressure is considerably closer to the free stream value than for the H-grid, it is now too high. Whether the calculated total pressures on the surface are higher or lower than the free stream value depends upon the interaction between the implementation of the boundary conditions and the numerical dissipation[43].

An examination of the Mach number contours for this calculation, presented in figure A-4(b) and (c), reveals two interesting features of the flow. The first feature is that the cambered airfoil is at 0.0^{o} angle of attack, and yet the flow stagnates on the upper surface of the wing near the leading edge. In addition, as the flow expands around the leading edge, a supersonic bubble with relatively high Mach numbers is created on the bottom surface. The gradients in the supersonic bubble coupled with the grid resolution and the numerical dissipation probably produce the change in total pressure on the bottom surface of the wing. Possibly a finer grid in this region could alleviate the problem. However, the present calculations resulted in near saturation of the incore storage of the Cyber 203 computer.

By eliminating the severe expansion around the leading edge, the total pressure losses on the surface of the wing can be prevented. This has been demonstrated for a symmetrical airfoil using the H-grid and was presented in figure A-2. It will also be demonstrated for the C-grid in two ways, first by going to a symmetrical airfoil as in the case for the H-grid, and second, by lowering the free stream Mach number. Figure A-5 presents the solution for the wing with the symmetrical airfoil and the C-

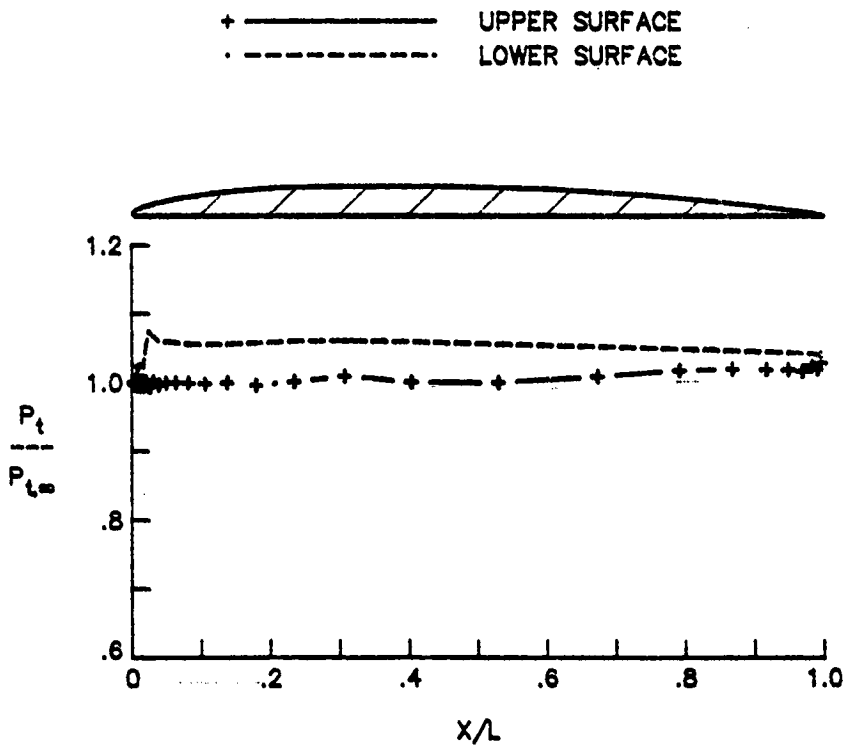

(a) Total pressure distributions.

Figure A-4. Solution for the wing with a cambered airfoil and a C-Grid. (M_∞ = 0.80, α = 0.0°)

Δ CONTOUR = 0.10

M = 1.00

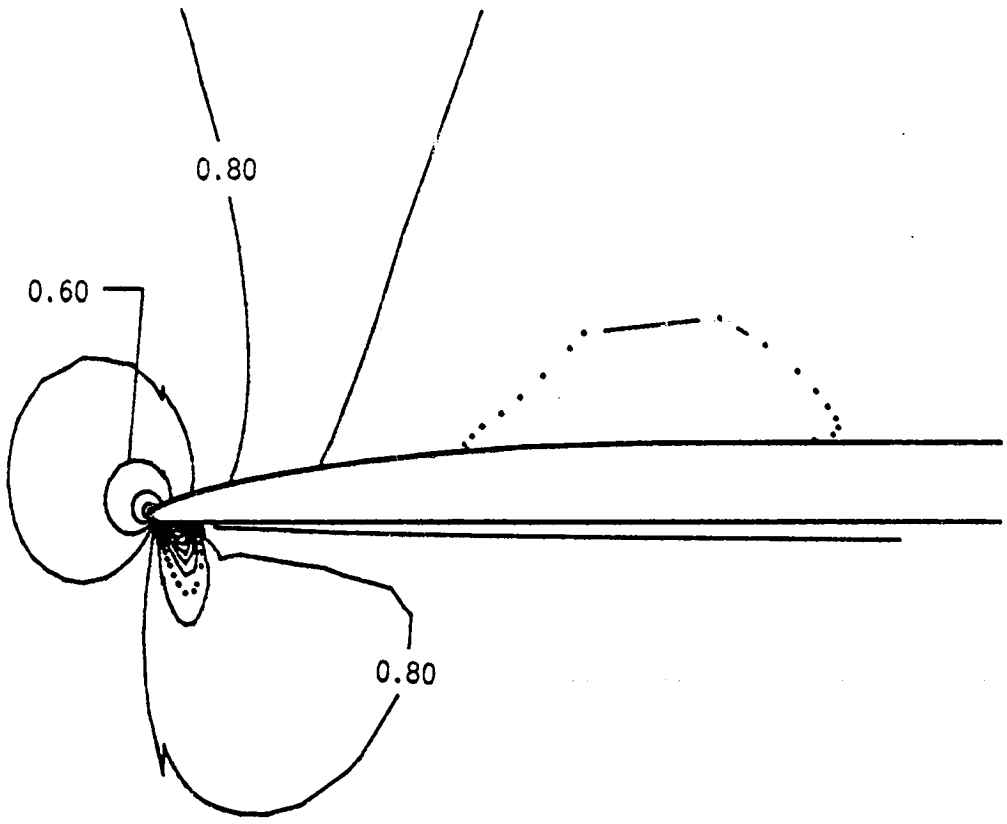

(b) Mach number contours in the vicinity of the leading edge.

Figure A-4. Continued.

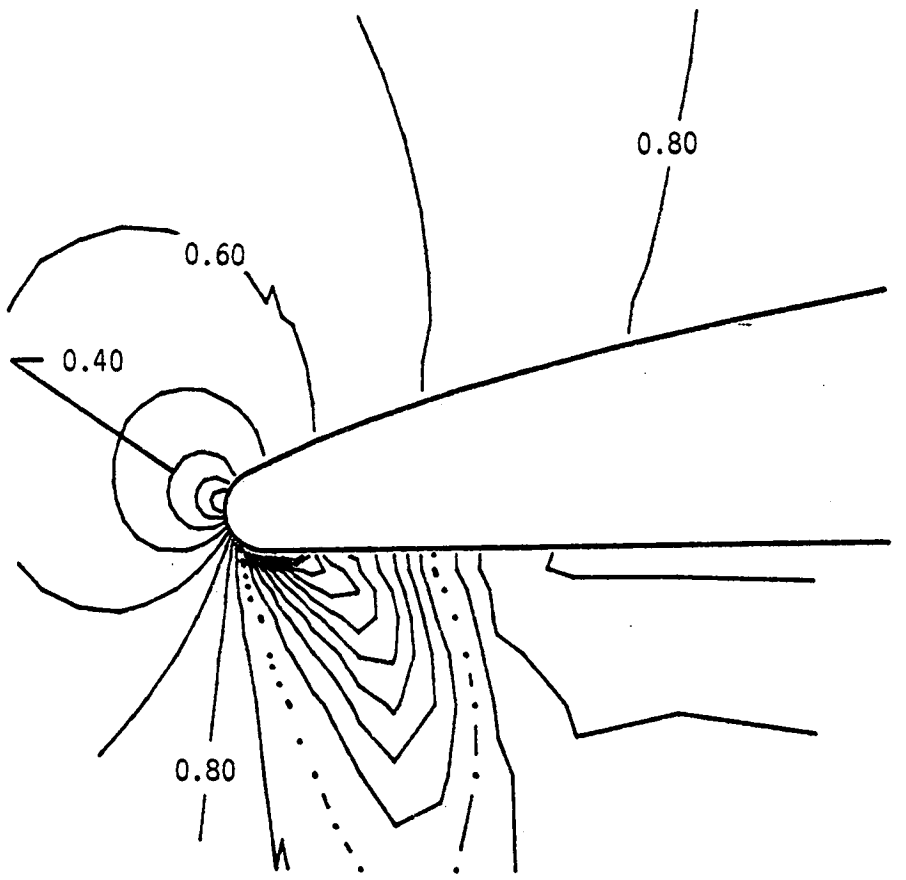

(c) Detail of the Mach number contours at the leading edge.

Figure A-4. Concluded.

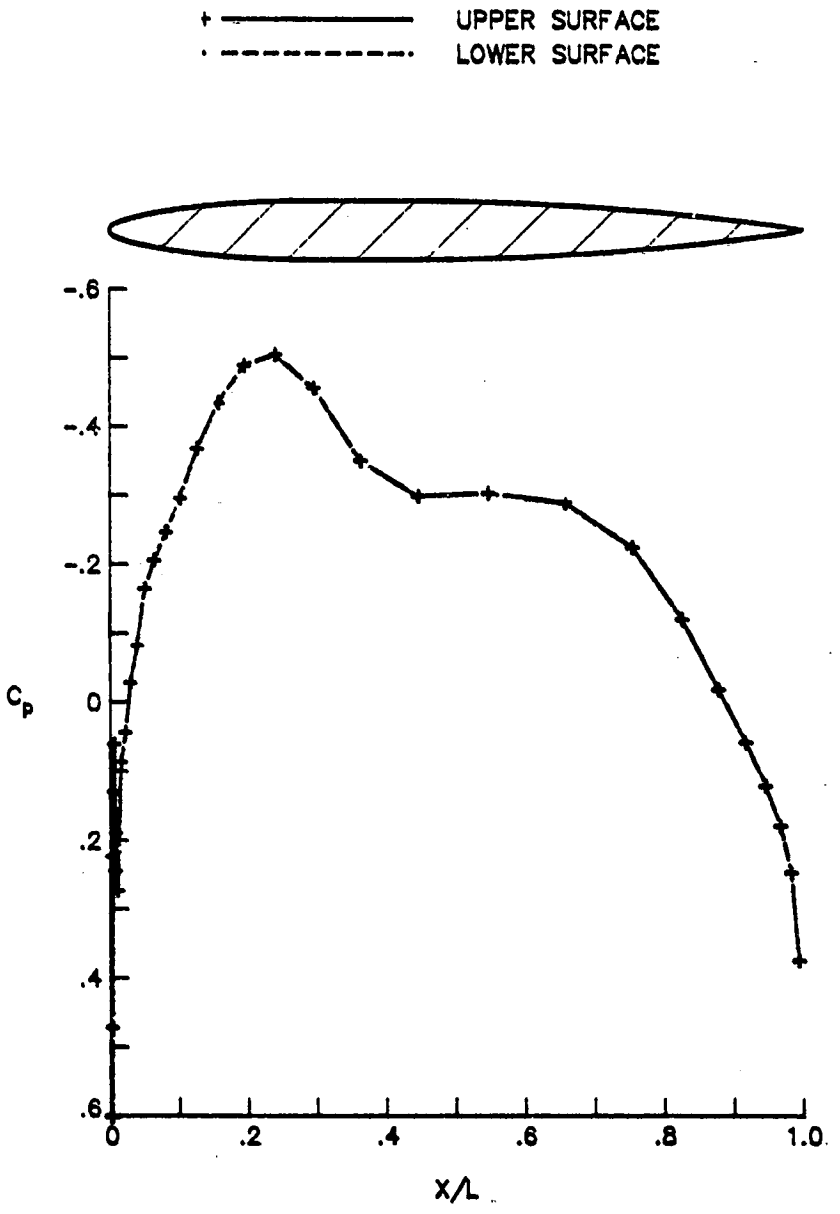

(a) Pressure coefficient distributions.

Figure A-5. Solution for the wing with a symmetrical airfoil and a C-grid at a free stream Mach number of 0.80. ($\alpha = 0.0^{o}$)

Δ CONTOUR = 0.10

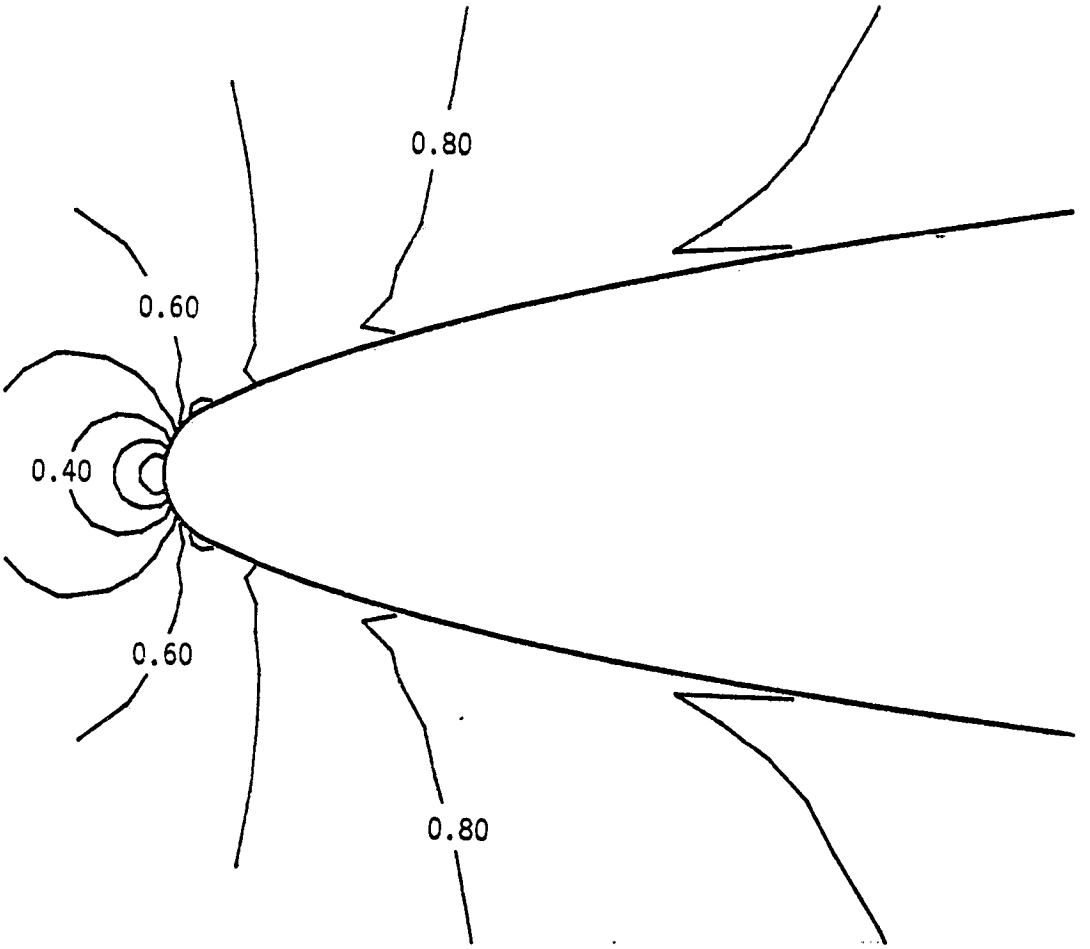

(b) Mach number contours in the vicinity of the leading edge.

Figure A-5. Continued.

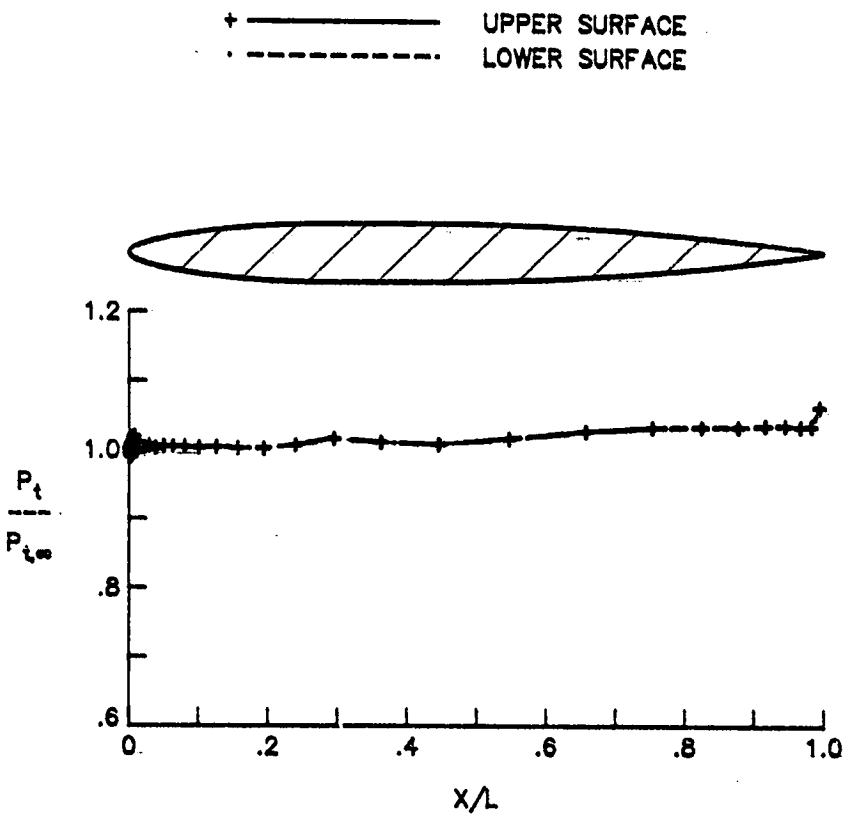

(c) Total pressure distributions.

Figure A-5. Concluded.

grid at a free stream Mach number of 0.80. The pressure coefficients, which are presented in part (a) of the figure, agree well with the corresponding pressure distributions calculated with the H-grid. Figure A-5(b), which shows the Mach number contours, illustrates that the stagnation point is at the forward most point of the airfoil, and that the strength of the expansion at the leading edge has been reduced. The resulting total pressure distributions are presented in part (c) of the figure, and show that the total pressure on the surface of the wing remains close to the free stream value.

By reducing the free-stream Mach number, it is also possible to reduce the strength of the expansion. The results for a free stream Mach number of 0.40 are presented in figure A-6. The pressure coefficients, presented in part (a), look reasonable although there are no experimental data with which to compare them. The Mach number contours in the vicinity of the leading edge, and the total pressure distributions, parts (b) and (c) respectively, illustrate the reduced strength of the expansion at the leading edge, and the resulting surface total pressures which are essentially at the free stream value.

An investigation to determine the cause of the total pressure loss in the computed flow on the internal surface of the nacelle has been summarized in this appendix. It was found that the loss was associated with the flow expanding around the sharp leading edge of the nacelle and thus creating severe local gradients in the flow field. It was determined that by reducing the severity of these gradients, the total pressure loss could be prevented. Although the specific approaches used for the wing (C-grid and reduced Mach number) were not attempted for the nacelle, an alternate approach in which the nacelle geometry was modified such that

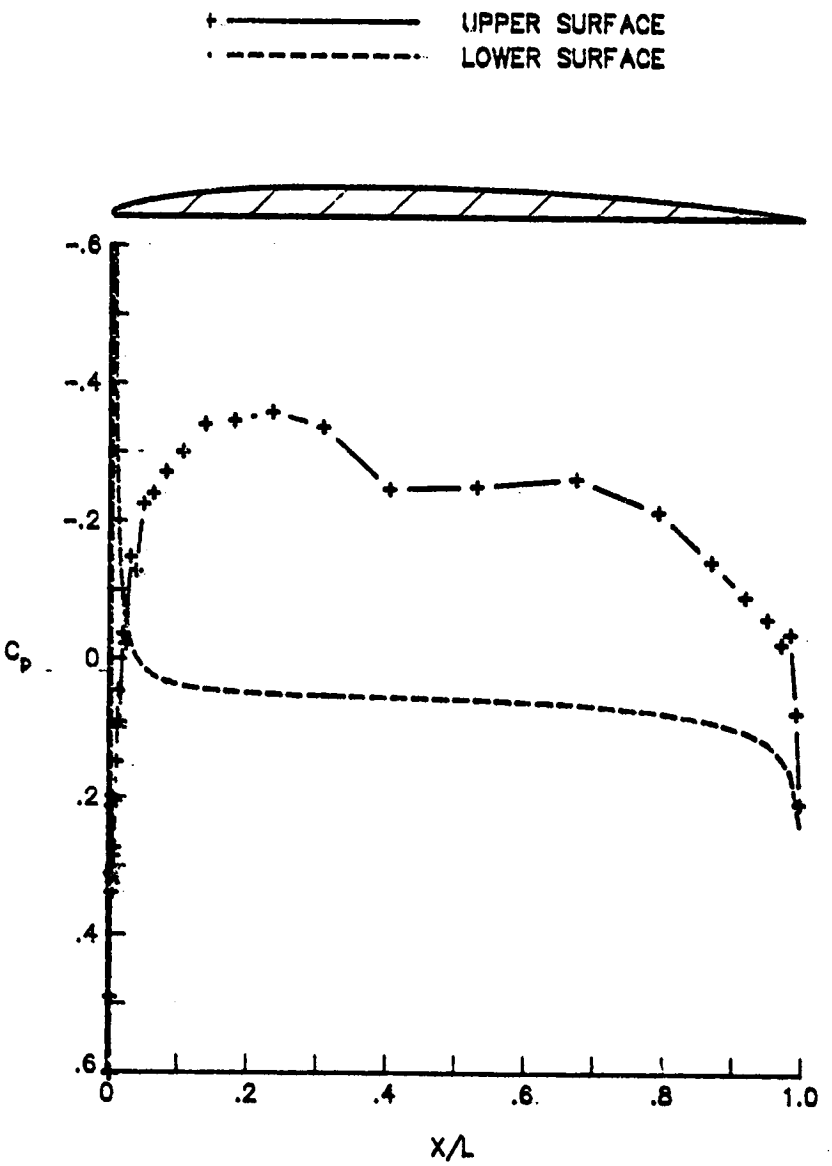

(a) Pressure coefficient distributions.

Figure A-6. Solution for the wing with a cambered airfoil and a C-grid at a free stream Mach number of 0.40. ($\alpha = 0.0^{o}$)

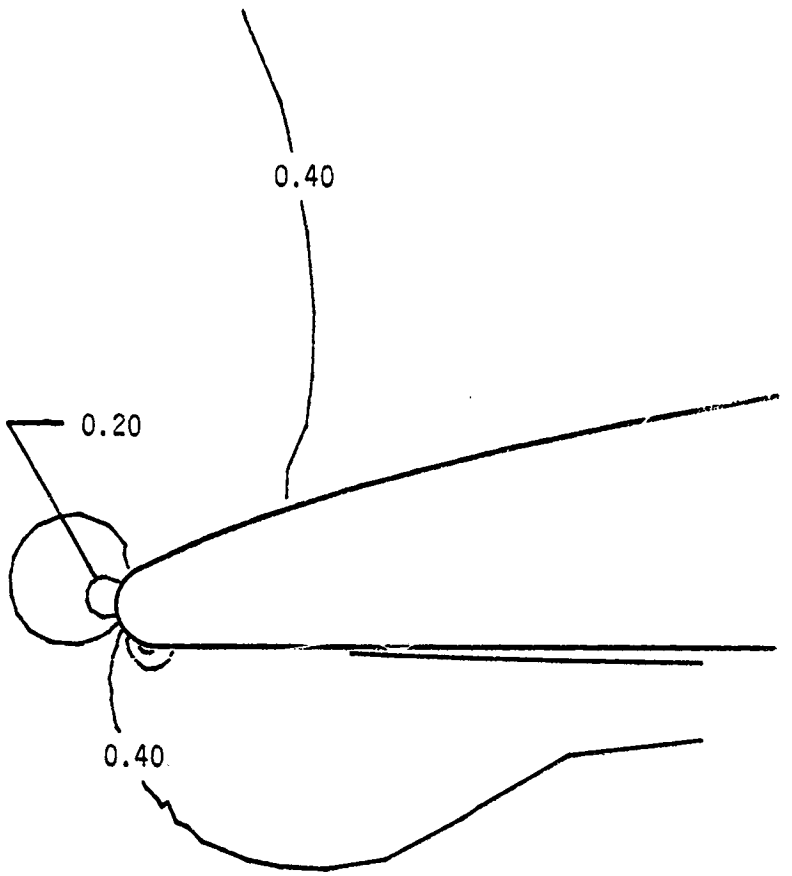

(b) Detail of Mach number contours at the leading edge.

Figure A-6. Continued.

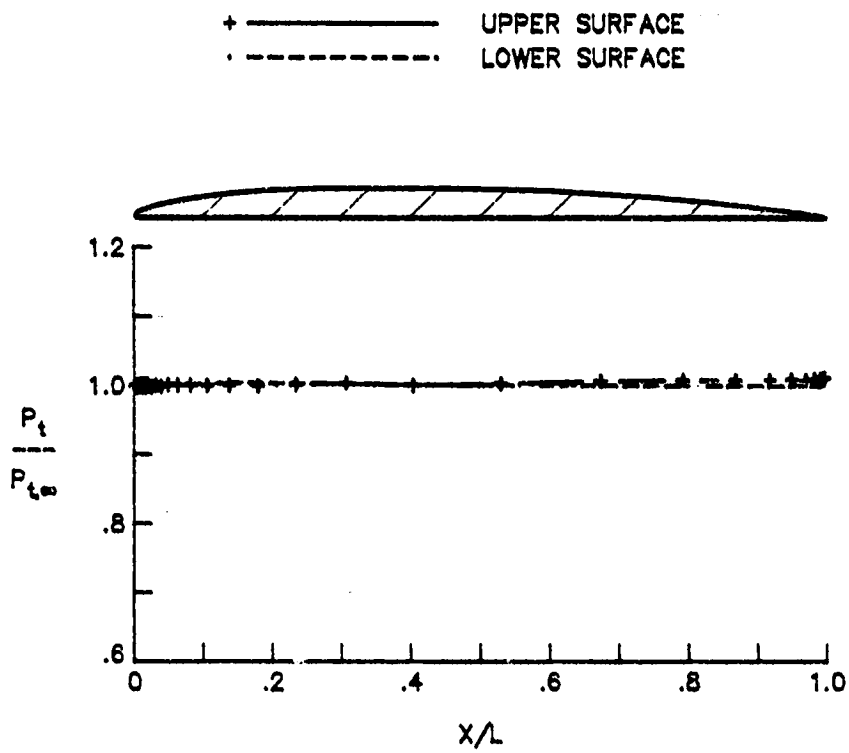

(c) Total pressure distributions.

Figure A-6. Concluded.

stagnation occured precisely at the leading edge was tried. This modified nacelle produced similar results in that the loss in total pressure was eliminated (see Cnapter VI). The implication is that almost any modification to the leading-edge treatment that either reduces or resolves the flow gradients should produce similar results.

REFERENCES

[1] Maglieri, Dominic J. and Dollyhigh, Samuel M., "Special Section on the Outlook for Advanced Transport Aircraft," Astronautics and Aeronautics, Feburary 1982.

[2] Graves, Randolf A., Jr., "Computational Fluid Dynamics - The Coming Revolution," Astronautics and Aeronautics, March 1982.

[3] Hess, J. L., "Calculation of Potential Flow About Arbitrary Three-Dimensional Lifting Bodies," MDC J5679-01, McDonnell Douglas, October 1972.

[4] Boppe, C. W. and Stern, M. A., "Simulated Transonic Flows for Aircraft With Nacelles, Pylons, and Winglets," AIAA Paper 80-0130, January 1980.

[5] Reyhner, Theodore A., "Computation of Transonic Potential Flow About Three-Dimensional Inlets, Ducts, and Bodies," NASA Contractor Report 351A, March 1982.

[6] Rizzi, A. and Erickson, L. E., "Transfinite Mesh Generation and Damped Euler Equation Algorithm for Transonic Flow Around Wing-Body Configurations," AIAA Paper 81-0999, Computational Fluid-Dynamics Conference, June 1981.

[7] Salas, M. D., Jameson, A., and Melnik R. E., "A Comparative Study of the Nonuniqueness Problem of the Potential Equation," AIAA Conference Procedings 83-1888, January 1983.

[8] Steinhoff, J. and Jameson, A., "Multiple Solutions of the Transonic Potential Flow Equation," AIAA Journal, Vol. 20, No. 11, November 1981.

[9] Srinivasan, G. R., Chyu, W. J., and Steger, J. L., "Computations of Simple Three-Dimensional Wing-Vortex Interaction in Transonic Flow," AIAA Paper 81-1206, June 1981.

[10] Cline, Michael C., "NAP: A Computer Program for the Computation of Two-Dimensional, Time-Dependent, Inviscid Nozzle Flow," Los Alamos Scientific Laboratory Report LA-5984, January 1977.

[11] Schmidt, W., Jameson, A., and Whitfield, D., "Finite Volume Solution for the Euler Equation for Transonic Flow Over Airfoils," Journal of Aircraft, Vol. 20, Feb. 1983, pp. 127-133.

[12]Jameson, A., Schmidt, W., and Turkel, E., "Numerical Solutions or the Euler Equations by Finite Volume Methods Using Runge-Kutta Time-Stepping Schemes," AIAA Paper 81-1259, June 1981.

[13]Jameson, Antony and Baker, Timothy J., "Solution of the Euler Equations for Complex Configurations," AIAA Paper 83-1929, June 1983.

[14]Compton, W. B. III and Whitesides, J. L., "Three-Dimensional Euler Solutions for Long-Duct Nacelles," AIAA Paper 83-0089, January 1983.

[15]Cline, Michael C., "Stability Aspects of Diverging Subsonic Flow," AIAA Journal Article NO. 80-4036, Vol. 13, No. 5, May 1980.

[16]Oliger, Joseph and Sundstrom, Arne, "Theoretical and Practical Aspects of Some Initial Boundary Value Problems in Fluid Dynamics," SIAM Journal of Applied Mathematics, Vol. 35, No. 3, November 1978.

[17]Beam, Richard M. and Warming, R. F., "An Implicit Factored Scheme for the Compressible Navier-Stokes Equations," AIAA Journal, Vol. 1, No. 4, April 1978.

[18]Steger, J. L., "Implicit Finite Difference Simulation of Flow About Arbitrary Geometrics with Application to Airfoils," AIAA Paper 77-665, June 1977.

[19]Thomas, P. D., "Numerical Method for Predicting Flow Characteristics and Performance of Nonaxisymmetric Nozzles-Theory," NASA Contractor Report 3147, September 1979.

[20]Warming, R. F. and Beam, Richard M., "On the Construction and Application of Implicit Factored Schemes for Conservation Laws," SIAM-AMS Proceedings, Volume II, pp. 85-129, 1978.

[21]Roach, Patrick J.: Computational Fluid Dynamics. Hermosa Publishers, Albuquerque, New Mexico, 1972, pp. 33-36.

[22]Pulliam, Thomas H. and Steger, Joseph L., "On Implicit Finite-Difference Simulations of Three-Dimensional Flow," AIAA Paper 78-0010, Janurary 1978.

[23]Abarbanel, Saul S., Dwoyer Douglas L., and Gottlieb, David, "Stable Implicit Finite-Difference Methods for Three- Dimensional Hyperbolic Systems," Institute for Computer Applications in Science and Engineering Report 82-39, NASA Langley Research Center, November 1982.

[24]Bayliss, Alvin and Turkel, Eli, "Far Field Boundary Conditions for Compressible Flows," Numerical Boundary Condition Procedures, NASA Conference Publication 2201, October 1981.

[25]Rudy, David H. and Strikwerda, John C., "Boundary Conditions for Subsonic Compressible Navier-Stokes Calculations," Computers and Fluids, Vol. 9, 1981, pp. 327-338.

[26]Lerat, A., "Implicit Methods of Second-Order Accuracy for the Euler Equations," AIAA Paper 83-1925, July 1983.

[27]Rizzi, A., "Numerical Implementation of Solid-Body Boundary Conditions for the Euler Equations," ZAMM 58, T301-T304, 1978.

[28]Anderson, Dale A., Tannehill, John C., and Pletcher, Richard H., "Computational Fluid Mechanics and Heat Transfer," Hemisphere Publishing Corporation, McGraw Hill, 1984, pp. 329-363.

[29]Green, J. E., Weeks, D. J., and Brooman, J. W. F., "Prediction of Turbulent Boundary Layers and Wakes in Compressible Flow by a Lag-Entrainment Method," RAE Technical Report 72231, January 1973.

[30]Cyber 200 Mathematical Library, Central Scientific Computing Document S-3, NASA, Langley Research Center, Section VD2.1, October 1984.

[31]Thomas, James Lee, "Transonic Viscous-Inviscid Interaction Using Euler And Inverse Boundary-Layer Equations," PhD Dissertation, Mississippi State University, December 1983.

[32]Johnston, W. and Sochol, P.,"A Viscous-Inviscid Interactive Compressor Calculation," AIAA Paper 89-1140, July 1978.

[33]Lock, R. C., "A Review of Methods for Predicting Viscous Effects on Aerofoils and Wings at Transonic Speeds," AGARD Conference Proceedings NO. 291, September - October 1980.

[34]Melnik, R. E., "Turbulent Interactions on Airfoils at Transonic Speeds - Recent Developments," AGARD Conference Proceedings No. 291, September - October 1980.

[35]Re, Richard J. and Peddrew, Kathryn H., "Tabulations of Static Pressure Coefficients on the Surface of Three Pylon-Mounted Axisymmetric Flow-Through Nacelles at Mach Numbers from 0.40 to 0.98," NASA Technical Memorandum 84540, September 1982.

[36]Miranda, Louis, "Private Communication," Lockheed California Company, Burbank, California, September 1984.

[37]Dwoyer, Douglas L., "Private communication," NASA, Langley Research Center, September 1984.

[38]Warming, R. F. and Beam, Richard M., "An Extension of A-Stability to Alternating Direction Implicit Methods," BIT, No. 19, 1979, pp 395-417.

[39]Jameson, A. and Turkel E., "Implicit Schemes and L-U Decompositions," Mathematics of Computation, Vol. 37, No. 156, October 1981, pp 385-397.

[40]Vatsa, Veer N., "Private Communication," NASA, Langley Research Center, August 1984.

[41]Ballhaus, W. F., Jr., "Computational Aerodynamics and Supercomputers," NASA Technical Memorandum 85887, January 1984.

[42]Capone, F. J. and Bare, E. A., "Subsonic/Supersonic Aerodynamic Characteristics for a Tactical Supercruiser," AIAA Paper 84-2192, August 1984.

[43]Salas, M. D., "Private Communication," NASA, Langley Research Center, March 1984.

BIOGRAPHICAL SKETCH

William Bernard Compton, III, was born in [redacted] on [redacted]. He graduated from Coffee High School at Florence, Alabama in 1957. In June 1961, he graduated from the University of Alabama with a Bachelor of Science degree in Aeronautical Engineering. Shortly thereafter, he became an employee of the National Aeronautics and Space Administration (NASA) at the Langley Research Center.

In December 1961, Mr. Compton was called to active military duty status in the United States Naval Reserve. He attended the Naval Officer Candidate School at Newport, Rhode Island, and upon graduation in June 1962, received a commission as an ensign in the United States Naval Reserve. He served onboard the USS Taconic (AGC-17) and the USS Vulcan (AR-5), before returning to inactive military duty status in June 1965.

In 1965, Mr. Compton returned to work for NASA at the Langley Research Center where he is a research engineer. In 1968, he enrolled in the Center's part-time graduate study program with the George Washington University's Joint Institute for Advancement of Flight Sciences. He received a Master of Science degree from the George Washington University in September 1973.

Mr. Compton continued part-time graduate study at the George Washington University's Joint Institute for Advancement of Flight Sciences in January 1974 by enrolling in their Doctor of Science degree program. He completed the course requirements for a Doctor of Science degree in

Fluid Mechanics and Thermal Sciences in May 1977, and is currently continuing pursuit of that degree.